NASA Contractor Report 4770

A Three-Dimensional Linearized Unsteady Euler Analysis for Turbomachinery Blade Rows

Matthew D. Montgomery and Joseph M. Verdon
United Technologies Research Center
East Hartford, Connecticut

Prepared for
Lewis Research Center
under Contract NAS3–26618

National Aeronautics and
Space Administration

Office of Management
Scientific and Technical
Information Program

1997

A Three-Dimensional Linearized Unsteady Euler Analysis for Turbomachinery Blade Rows

Contents

List of Figures

Figure 14. Contours of the in-phase component of the unsteady pressure at midspan due to the interaction of an acoustic excitation from upstream [$p^-_{A,\mathrm{Ref}} = (1,0)$, $\omega = 3.332$, $\sigma = 90\,\mathrm{deg}$] with the helical fan.

Figure 15. Unsteady surface pressure distributions due to the interaction of an acoustic excitation from downstream [$p^+_{A,\mathrm{Ref}} = (1,0)$, $\omega = 3.332$ and $\sigma = 90\,\mathrm{deg}$] with the helical fan.

Figure 16. Unsteady surface pressure distributions at midspan ($r/r_D = 0.9$) due to the interaction of an acoustic excitation from downstream [$p^+_{A,\mathrm{Ref}} = (1,0)$, $\omega = 3.332$, $\sigma = 90\,\mathrm{deg}$] with the helical fan.

Figure 17. Contours of the in-phase component of the unsteady pressure at midspan due to the interaction of an acoustic excitation from downstream [$p^+_{A,\mathrm{Ref}} = (1,0)$, $\omega = 3.332$, $\sigma = 90\,\mathrm{deg}$] with the helical fan.

Figure 18. Axial eigenvalues, $\chi = \beta + i\kappa_\xi$, for three circumferential ($m = -1, 0, 1$) and three radial ($\mu = 0, 1, 2$) modes of acoustic disturbance in the far field of the helical fan, for an unsteady flow at $\omega = 3.887$ and $N_D = 3$.

Figure 19. Unsteady surface pressure distributions at $r/r_D = 0.8$ (– – –), $r/r_D = 0.9$ (——) and $r/r_D = 1.0$ (- - - -), due to the interaction of an acoustic excitation from upstream [$p^-_{A,\mathrm{Ref}} = (1,0)$, $\omega = 3.887$ and $\sigma = 45\,\mathrm{deg}$], with the helical fan.

Figure 20. Unsteady surface pressure distributions at midspan ($r/r_D = 0.9$) due to the interaction of an acoustic excitation from upstream [$p^-_{A,\mathrm{Ref}} = (1,0)$, $\omega = 3.887$ and $\sigma = 45\,\mathrm{deg}$], with the helical fan.

Figure 21. Unsteady surface pressure distributions at $r/r_D = 0.8$ (– – –), $r/r_D = 0.9$ (——) and $r/r_D = 1.0$ (- - - -), due to the interaction of an acoustic excitation from downstream [$p^+_{A,\mathrm{Ref}} = (1,0)$, $\omega = 3.887$ and $\sigma = 45\,\mathrm{deg}$], with the helical fan.

Figure 22. Unsteady surface pressure distributions at midspan ($r/r_D = 0.9$) due to the interaction of an acoustic excitation from downstream [$p^\mp_{A,\mathrm{Ref}} = (1,0)$, $\omega = 3.887$ and $\sigma = 45\,\mathrm{deg}$], with the helical fan.

Figure 23. Relative surface Mach number distributions for the 3D 10th Standard Cascade ($M^{\mathrm{abs}}_{-\infty} = 0.4015$, $|\Omega| = 0.2145$): (a) TURBO predictions; (b) TURBO and CASPOF predictions at midspan, $r/r_D = 0.9$.

Figure 24. Relative frame steady flow properties far upstream and far downstream of the 3D 10th Standard Cascade ($M^{\mathrm{abs}}_{-\infty} = 0.4015$, $|\Omega| = 0.2145$).

Figure 25. Axial eigenvalues, $\chi = \beta + i\kappa_\xi$, for three circumferential ($m = -1, 0, 1$) and three radial ($\mu = 0, 1, 2$) modes of acoustic disturbance far upstream and far downstream of the 3D 10th Standard Cascade, for an unsteady flow at $\omega = 1.0$ and $N_D = 6$.

Figure 26. Radial pressure modes, $p^R_{m\mu}(r)$, $m = -1, 0, 1$, $\mu = 0, 1, 2$, for an acoustic excitation or response at $N_D = 6$ far upstream and for an acoustic response at $N_D = 6$ far

downstream of the 3D 10th Standard Cascade: (——) in-phase (real) component of $p^R_{m\mu}$; (– – –) out-of-phase (imaginary) component of $p^R_{m\mu}$.

Figure 27. Local work per cycle distributions at $r/r_D = 0.8$ (– – –), $r/r_D = 0.9$ (——) and $r/r_D = 1.0$ (- - - -), and global works per cycle for the 3D 10th Standard Cascade undergoing pure torsional vibrations about midchord and pure bending vibrations, at $\omega = 1$ and $\sigma = \mp 90$ deg ($N_D = \mp 6$).

Figure 28. Local work per cycle distributions at midspan, as predicted using the 3D LINFLUX (——) and the 2D LINFLO (– – –) analyses, for the 3D 10th Standard Cascade undergoing torsional blade vibrations about midchord at $\omega = 1$.

Figure 29. Local work per cycle distributions at midspan, as predicted using the 3D LINFLUX (——) and the 2D LINFLO (– – –) analyses, for the 3D 10th Standard Cascade undergoing bending vibrations at $\omega = 1$.

Figure 30. Work per cycle versus interblade phase angle for the 3D 10th Standard Cascade undergoing pure torsional vibrations about midchord (top) and pure bending vibrations (bottom) at $\omega = 1$.

Figure 31. Axial eigenvalues, $\chi = \beta + i\kappa_\xi$, for five circumferential ($m = -2, \ldots, 2$) and three radial ($\mu = 0, 1, 2$) modes of acoustic disturbance far upstream and far downstream of the 3D 10th Standard Cascade, for unsteady flow at $\omega = 3.218$ and $N_D = 9$.

Figure 32. Unsteady surface pressure distributions due to the interaction of an acoustic excitation from upstream [$p^-_{A,\mathrm{Ref}} = (1, 0)$, $\omega = 3.218$ and $\sigma = 135$ deg] with the 3D 10th Standard Cascade.

Figure 33. Unsteady surface pressure distributions at midspan ($r/r_D = 0.9$) due to the interaction of an acoustic excitation from upstream [$p^-_{A,\mathrm{Ref}} = (1, 0)$, $\omega = 3.218$, $\sigma = 135$ deg] with the 3D 10th Standard Cascade.

Figure 34. Contours of the in-phase component of the unsteady pressure at midspan due to the interaction of an acoustic excitation from upstream [$p^-_{A,\mathrm{Ref}} = (1, 0)$, $\omega = 3.218$, $\sigma = 135$ deg] with the 3D 10th Standard Cascade.

Figure 35. Unsteady surface pressure distributions due to the interaction of an acoustic excitation from downstream [$p^+_{A,\mathrm{Ref}} = (1, 0)$, $\omega = 3.218$ and $\sigma = 135$ deg] with the 3D 10th Standard Cascade.

Figure 36. Unsteady surface pressure distributions at midspan due to the interaction of an acoustic excitation from downstream [$p^+_{A,\mathrm{Ref}} = (1, 0)$, $\omega = 3.218$, $\sigma = 135$ deg] with the 3D 10th Standard Cascade.

Figure 37. Contours of the in-phase component of the unsteady pressure at midspan due to the interaction of an acoustic excitation from downstream [$p^+_{A,\mathrm{Ref}} = (1, 0)$, $\omega = 3.218$, $\sigma = 135$ deg] with the 3D 10th Standard Cascade.

Figure 38. Axial eigenvalues, $\chi = \beta + i\kappa_\xi$, for five circumferential ($m = -2, \ldots, 2$) and three radial ($\mu = 0, 1, 2$) modes of acoustic disturbance far upstream and far downstream of the 3D 10th Standard Cascade, for an unsteady flow at $\omega = 3.861$ and $N_D = 6$.

Figure 39. Unsteady surface pressure distributions due to the interaction of an acoustic excitation from upstream [$p^-_{A,\mathrm{Ref}} = (1, 0)$, $\omega = 3.861$ and $\sigma = 90\,\mathrm{deg}$] with the 3D 10th Standard Cascade.

Figure 40. Unsteady surface pressure distributions at midspan ($r/r_D = 0.9$) due to the interaction of an acoustic excitation from upstream [$p^-_{A,\mathrm{Ref}} = (1, 0)$, $\omega = 3.861$ and $\sigma = 90\,\mathrm{deg}$] with the 3D 10th Standard Cascade.

Figure 41. Contours of the in-phase component of the unsteady pressure at midspan due to the interaction of an acoustic excitation from upstream [$p^-_{A,\mathrm{Ref}} = (1, 0)$, $\omega = 3.861$, $\sigma = 90\,\mathrm{deg}$] with the 3D 10th Standard Cascade.

Figure 42. Unsteady surface pressure distributions, as predicted by the 2D LINFLUX and LINFLO analyses, due to the interaction of an acoustic excitation from upstream [$p^-_A = (1, 0)$, $\omega = 3.861$, $\sigma = 90\,\mathrm{deg}$] with the 2D 10th Standard Cascade. The LINFLUX solutions were determined on 141 × 41 (a), 211 × 61 (b), and 281 × 81 (c) H-meshes.

A Three-Dimensional Linearized Unsteady Euler Analysis for Turbomachinery Blade Rows

Summary

A three-dimensional, linearized, Euler analysis is being developed to provide an efficient unsteady aerodynamic analysis that can be used to predict the aeroelastic and aeroacoustic responses of axial-flow turbomachinery blading. The field equations and boundary conditions needed to describe nonlinear and linearized inviscid unsteady flows through a blade row operating within a cylindrical annular duct are presented in this report. A numerical model for linearized inviscid unsteady flows, which couples a near-field, implicit, wave-split, finite volume analysis to a far-field eigenanalysis, is also described. The linearized aerodynamic and numerical models have been implemented into a three-dimensional linearized unsteady flow code, called LINFLUX. This code has been applied herein to selected, benchmark, unsteady, subsonic flows to establish its accuracy and to demonstrate its current capabilities. The unsteady flows considered, have been chosen to allow convenient comparisons between the LINFLUX results and those of well-known, two dimensional, unsteady flow codes. The detailed numerical results for a helical fan and a three-dimensional version of the 10th Standard Cascade indicate that important progress has been made towards the development of a reliable and useful, three-dimensional, prediction capability that can be used in aeroelastic and aeroacoustic design studies.

1. Introduction

The development of analyses to predict unsteady flows in axial-flow turbomachines is motivated primarily by the need to predict the aeroelastic (flutter and forced vibration) and aeroacoustic (sound generation and propagation) characteristics of the blading. Accurate and efficient aerodynamic analyses are needed to determine the unsteady loads that act on the blades and the unsteady pressure responses that persist upstream and downstream of the blade row, for various sources of excitation. These include structural (blade) motions and aerodynamic disturbances at inlet and exit that carry energy towards the blade row. The computational resources required to simulate nonlinear and viscous unsteady fluid dynamic behavior will continue to prohibit the use of such simulations in detailed, parametric, aeroelastic or aeroacoustic design studies. Therefore, approximate, e.g., linearized inviscid, analyses are needed to provide efficient predictions of unsteady aerodynamic response phenomena.

Until recently, the linearized analyses available for turbomachinery aeroelastic and aeroacoustic applications, have been based on two- and three-dimensional, classical methods, see [Whi87, Nam87] for reviews. Such methods are very efficient, but are restricted to shock-free flows through lightly-loaded blade rows. Because of these limitations, two-dimensional, unsteady aerodynamic linearizations relative to nonuniform potential mean flows, as reviewed in [Ver93], have been developed. Such analyses account for the effects of real blade geometry, mean blade loading, and operation at transonic Mach numbers on unsteady aerodynamic response. They have received considerable attention in recent years and are being applied in aeroelastic and aeroacoustic design studies (e.g., see [Smi90, SS90, MM94]). However, more comprehensive linearizations are still needed to predict three-dimensional unsteady flows in which the effects of radial flow variations and mean swirl are important, and two- and three-dimensional flows in which strong shocks occur. For such flows, the nonlinear Euler equations are required to model the nonisentropic and rotational mean or steady background flow and linearized versions of these equations are required to model the unsteady perturbations.

Thus, much attention is now being given to the development of two- [HC93a, HC93b, KK93, MV95] and three-dimensional [HL93, HCL94] linearized Euler analyses. As in the earlier linearizations with respect to potential mean flows, the linearized Euler equations are developed in the frequency domain to address unsteady flows caused by temporally and circumferentially periodic unsteady excitations. Thus, explicit, physical time-dependence is removed from the resulting linear problem and the computational domain is limited to a single extended blade passage region. Unlike the earlier linearizations, the linearized Euler equations are solved over a deforming solution domain [HC93a, Gil93] so that troublesome extrapolation terms that would appear in the blade surface conditions are replaced with more tractable source terms in the linearized unsteady field equations. Also, because of the large number of unknowns involved, the discretized linear unsteady equations are solved iteratively, rather than by direct matrix inversion.

Under the present effort, we have proceeded with the development of a three-dimensional linearized Euler analysis. This analysis is based on a linearized unsteady aerodynamic formulation in the frequency domain, an implicit, flux-split, finite-volume, analysis for the unsteady flow in the near field, and an eigenanalysis for the unsteady perturbations far upstream and far downstream of a blade row. These three-dimensional unsteady aerodynamic

and numerical models have been implemented into a computer code, called LINFLUX. The LINFLUX analysis is described in detail in the present report, and numerical predictions, based on this analysis, are given for three-dimensional unsteady flows driven by prescribed blade motions and upstream and downstream traveling acoustic excitations.

A two-dimensional version of the LINFLUX analysis has been reported in [MV95, VMK95], where numerical results for subsonic and transonic unsteady flows excited by prescribed blade motions and external aerodynamic disturbances are provided and compared with those of the linearized potential analysis, LINFLO [Ver93] and the nonlinear Euler/Navier-Stokes analysis, NPHASE [HSR91, SLH+94, AV96]. These comparisons indicate that the 2D LINFLUX analysis gives accurate unsteady aerodynamic response information for unsteady subsonic flows excited by blade vibrations and external aerodynamic excitations, but improvements in the numerical modeling at shocks and near blade surfaces, are still required for the accurate resolution of unsteady transonic flows and unsteady flows excited by vortical gusts.

The main thrusts of the present effort have been to develop, validate and demonstrate a three-dimensional version of the LINFLUX analysis. A 3D numerical analysis and code has been constructed, in which a near-field, implicit, finite-volume analysis for the unsteady perturbations of an arbitrary mean flow is coupled to a far-field eigenanalysis for the unsteady perturbations of a fully-developed, axisymmetric, mean flow, to predict unsteady flows through three-dimensional blade rows operating within annular ducts. The near-field analysis is based upon the high-resolution, wave-split, finite-volume scheme developed for nonlinear unsteady flows by Whitfield, Janus and Simpson [WJS88] and implemented into the turbomachinery unsteady flow analysis, TURBO, by Janus, Horstman and Whitfield [JHW92]. The flux or wave splitting allows a sharp resolution of nonlinear shock phenomena — a feature which should facilitate the accurate prediction of impulsive unsteady shock loads with the linearized analysis in the future. The far-field analysis, which is coupled to the near-field, finite-volume analysis at the computational inflow and outflow boundaries, allows incoming external aerodynamic excitations to be prescribed, and outgoing response disturbances to pass through these computational boundaries without reflection.

The 3D LINFLUX analysis has been applied herein to predict relatively simple unsteady subsonic flows through three-dimensional blade rows; namely, a helical fan and a real-blade configuration, based on the 10th Standard Cascade [FV93]. We have considered unsteady flows excited by blade vibrations and acoustic excitations at inlet and exit. For validation purposes, we have selected highly two-dimensional unsteady excitations, i.e., blade motions of constant amplitude and acoustic excitations with zero radial nodes, and have compared the LINFLUX results with results determined using the two-dimensional, classical, linearized analysis of Smith [Smi72], and the two-dimensional, full-potential based linearization, LINFLO [Ver93]. Our predictions indicate that the current version of the 3D LINFLUX analysis can provide accurate unsteady aerodynamic response information for these benchmark test cases, but additional work is still needed to better understand mesh requirements, to enhance the computational efficiency of the LINFLUX analysis, and to extend its range of application.

2. Unsteady Flow through a Blade Row

We consider time-dependent adiabatic flow, with negligible body forces, of an inviscid non-heat conducting perfect gas through a rotating and vibrating blade row operating within a stationary annular duct (see Figure 1). The duct is of infinite axial extent and has inner and outer radii , $r = r_H$ and $r = r_D$, respectively. The blade row consists of N_B blades which rotate about the duct axis at constant angular velocity $\mathbf{\Omega} = \Omega \mathbf{e}_\xi$. In the absence of vibratory motion, the blades are assumed to be identical in shape, identical in orientation relative to an axisymmetric inlet flow, and equally spaced around the rotor.

We will analyze this unsteady flow in a reference frame that rotates with the blade row, in terms of cylindrical $(r,\ \theta,\ \xi,\ t)$ and Cartesian $(x_1, x_2, x_3, t) = (\xi,\ r\sin\theta,\ -r\cos\theta, t)$ coordinates. Here ξ and r measure distance along and radially outward from the duct axis, respectively, and θ measures angular distance in the direction opposite to the direction of rotation, which is assumed to be counterclockwise when looking in the axial flow direction. We will also have occasion to examine the flow in a stationary reference frame. Thus, when necessary, we will use the superscript abs to indicate a physical quantity measured relative to the stationary or absolute frame of reference; e.g., $\theta^{\text{abs}} = \theta + \Omega t$.

To describe flows in which the fluid domain deforms with time, it is useful to consider two sets of independent variables, say $(\mathbf{x}, t)$ and $(\bar{\mathbf{x}}, t)$. The position vector $\mathbf{x}(\bar{\mathbf{x}}, t) = \bar{\mathbf{x}} + \boldsymbol{\mathcal{R}}(\bar{\mathbf{x}}, t)$ describes the instantaneous location, in the rotating frame, of a moving field point, $\bar{\mathbf{x}}$ refers to the reference or mean position of this point, and $\boldsymbol{\mathcal{R}}(\bar{\mathbf{x}}, t)$ is the displacement of the point from its reference position. The displacement field, $\boldsymbol{\mathcal{R}}$, is prescribed so that the solution domain deforms with the vibratory motions of solid (i.e., blade) surfaces and is rigid far from the blade row.

In the present discussion, all physical variables are dimensionless. Lengths are scaled with respect to the reference length L^*, time with respect to the ratio L^*/V^* where V^* is the reference flow speed, velocity with respect to V^*, density with respect to a reference density ρ^*, pressure with respect to $\rho^*(V^*)^2$ and specific internal energy with respect to $(V^*)^2$. Here, the superscript $*$ refers to a dimensional reference value of a flow variable. To allow convenient comparisons between present 3D solutions and those of previous 2D analyses, the reference length is taken here to be the blade chord at midspan; the reference fluid density and flow speed, to be the inlet freestream density and relative flow speed at blade midspan, respectively.

For aeroelastic and aeroacoustic applications, we are usually interested in a restricted class of unsteady flows; those in which the unsteady fluctuations can be regarded as perturbations of a background flow that is steady in the reference frame that rotates with the blade row. Moreover, the steady background flows far upstream (say $\xi \leq \xi_-$) and far downstream $(\xi \geq \xi_+)$ from the blade row can be assumed to consist of at most a small steady perturbation from a steady, fully-developed axisymmetric, swirling flow. The time-dependent or unsteady fluctuations in these flows arise from temporally and circumferentially periodic unsteady excitations of small-amplitude, i.e., prescribed vibratory blade motions and prescribed aerodynamic disturbances at inlet and exit that carry energy towards the blade row.

For example, if the blades vibrate at reduced frequency, ω, as seen by an observer in the rotating frame, and at constant interblade phase angle, σ, we can write

$$\boldsymbol{\mathcal{R}}_{\mathrm{B}_n}(\bar{r}, \bar{\theta} + 2\pi n/N_B, \bar{\xi}, t) = \mathbf{T}_n Re\{\mathbf{R}_{\mathrm{B}}(\bar{r}, \bar{\theta}, \bar{\xi}) \exp[i(\omega t + n\sigma)]\},\ \bar{\mathbf{x}} \text{ on } B\ . \qquad (2.1)$$

Here, $\mathcal{R}_{B_n}$ is the displacement of a point on the nth moving blade surface from its mean position in the rotating frame; $\mathbf{T}_n$ is a rotation matrix, which relates a vector in the reference ($n = 0$) passage to its counterpart in the nth passage; $n = 0, 1, 2, \ldots, N_B - 1$ is a blade index; $Re\{\ \}$ denotes the real part of $\{\ \}$; $\mathbf{R}_B$ is the complex amplitude of the reference ($n = 0$) blade displacement; and B refers to the mean position of the reference blade. The interblade phase angle, σ, is determined by the nodal diameter pattern of the vibratory blade motion, i.e., $\sigma = 2\pi N_D/N_B$, where $|N_D|$, the number of nodal diameters, is the integer count of the number of times a disturbance pattern repeats around the wheel. The sign of N_D is determined by the direction of rotation of the disturbance pattern. If the vibratory disturbance pattern moves in the direction of blade rotation, i.e., the negative θ-direction, then $N_D > 0$.

The unsteady disturbances in the far upstream and far downstream regions of the flow are, in part, prescribed as a fluid dynamic excitation and, in part, depend upon the interaction between the fluid and the blading. Typically, an unsteady aerodynamic excitation is represented by a linear combination of fundamental disturbances that are harmonic in time, at temporal frequency ω, and in the circumferential direction, at circumferential wave number N_D.

For example, if the underlying mean flow is uniform, the pressure associated with a fundamental acoustic excitation is of the form

$$\tilde{p}_A(r, \theta, \xi, t) = Re\{a^{\mp} p^{R,\mp}(r) \exp[\chi^{\mp}\xi + i(\bar{m}\theta + \omega t)]\}, \quad \xi \lesseqgtr \xi_{\mp} \ . \tag{2.2}$$

Here, $\tilde{p}_A(\mathbf{x}, t)$ describes an incident pressure disturbance, i.e., a pressure disturbance that travels towards the blade row from far upstream ($\xi \leq \xi_-$) or far downstream ($\xi \geq \xi_+$). The quantities ω, $\bar{m} = N_D + mN_B = (\sigma + 2\pi m)N_B/2\pi$, where m is an integer, and the disturbance amplitude, $a^{\mp}$, are prescribed; the radial mode shape, $p^{R,\mp}(r)$, and the coefficient $\chi^{\mp} = \beta^{\mp} + i\kappa_\xi^{\mp}$, where β is the axial attenuation coefficient and κ_ξ is the axial wave number of the pressure disturbance, are determined by the equations that govern the unsteady fluid motion in the far field.

If equation (2.2) describes a pressure excitation as seen by an observer fixed in the rotating frame, then the frequency of this excitation in the stationary frame is $\omega^{abs} = \omega - N_D\Omega$, where the rotation term, $-N_D\Omega$, accounts for the Doppler shift.

3. Unsteady Aerodynamic Formulations

The equations that govern the unsteady flows, described in §2, are given below. These equations, which describe the flow seen by an observer fixed in the rotating frame, are based on the conservation laws for mass, momentum and energy and the thermodynamic relations for a perfect gas. The nonlinear equations in §3.1 describe the unsteady flow at the moving field points $\mathbf{x} = \bar{\mathbf{x}} + \boldsymbol{\mathcal{R}}(\bar{\mathbf{x}}, t) \in \mathcal{V}$, where $\boldsymbol{\mathcal{R}}(\bar{\mathbf{x}}, t)$ is a prescribed unsteady displacement field, which depends upon the vibratory blade motion, i.e., $\boldsymbol{\mathcal{R}} = \boldsymbol{\mathcal{R}}_{\mathrm{B}_n}$ for $\bar{\mathbf{x}} \in \mathrm{B}_n$, and $\mathcal{V}$ is a moving control volume. The linear equations in §3.2 describe an unsteady perturbation, driven by small-amplitude, circumferentially periodic, and temporally harmonic excitations, of a nonlinear background flow that is steady in the rotating frame. In this case $\boldsymbol{\mathcal{R}} = \mathrm{Re}\{\mathbf{R}(\bar{\mathbf{x}}) \exp(i\omega t)\}$, where $|\mathbf{R}| \sim \mathcal{O}(\epsilon)$ and ω is the temporal frequency of the unsteady motion, as seen by an observer in the rotating frame.

3.1 Nonlinear Unsteady Aerodynamic Equations

Consider an arbitrary moving control volume, $\mathcal{V}(t)$, which is bounded by the control surface $\mathcal{A}(\mathbf{x}, t) = 0$. The conservation laws for the fluid within $\mathcal{V}$ at time t, referenced to a coordinate frame that rotates with the blade row at constant angular velocity $\boldsymbol{\Omega}$, can be written in column vector form as

$$\frac{d}{dt}\int_{\mathcal{V}} \tilde{\mathbf{U}} d\mathcal{V} + \int_{\mathcal{A}} [\tilde{\mathbf{F}}_{x_j} - \tilde{\mathbf{U}}\dot{\mathcal{R}}_{x_j}] n_{x_j} d\mathcal{A} = \int_{\mathcal{V}} \tilde{\mathbf{S}} d\mathcal{V} \ . \tag{3.1}$$

Here, the symbol $\tilde{}$ indicates an unsteady flow quantity, $\dot{\boldsymbol{\mathcal{R}}} = (\dot{\mathcal{R}}_{x_1}, \dot{\mathcal{R}}_{x_2}, \dot{\mathcal{R}}_{x_3})$ is the velocity of a field point embedded in the control surface $\mathcal{A}$, $\mathbf{n}$ is a unit normal vector pointing outward from this surface, and a summation over repeated indices is implied. The source term on the right-hand-side of (3.1) accounts for the rotation of the reference coordinate frame.

The state, $\tilde{\mathbf{U}}$, flux, $\tilde{\mathbf{F}}_{x_j}, j = 1, 2, 3$, and source term, $\tilde{\mathbf{S}}$, vectors in equation (3.1) are defined by

$$\tilde{\mathbf{U}} = \begin{bmatrix} \tilde{\bar{\rho}} \\ \tilde{\bar{\rho}}\tilde{V}_{x_1} \\ \tilde{\bar{\rho}}\tilde{V}_{x_2} \\ \tilde{\bar{\rho}}\tilde{V}_{x_3} \\ \tilde{\bar{\rho}}\tilde{E}_T \end{bmatrix} , \ \mathbf{F}_{x_j}(\tilde{\mathbf{U}}) = \begin{bmatrix} \tilde{U}_{j+1} \\ \tilde{U}_{j+1}\tilde{U}_2/\tilde{U}_1 + \tilde{P}\delta_{1j} \\ \tilde{U}_{j+1}\tilde{U}_3/\tilde{U}_1 + \tilde{P}\delta_{2j} \\ \tilde{U}_{j+1}\tilde{U}_4/\tilde{U}_1 + \tilde{P}\delta_{3j} \\ \tilde{U}_{j+1}(\tilde{U}_5 + \tilde{P})/\tilde{U}_1 \end{bmatrix} , \ \tilde{\mathbf{S}}(\tilde{\mathbf{U}}, \mathbf{x}) = \begin{bmatrix} 0 \\ 0 \\ \Omega^2\tilde{U}_1 x_2 + 2\Omega\tilde{U}_4 \\ \Omega^2\tilde{U}_1 x_3 - 2\Omega\tilde{U}_3 \\ \Omega^2(\tilde{U}_3 x_2 + U_4 x_3) \end{bmatrix} \tag{3.2}$$

where $\tilde{\bar{\rho}}$, $\tilde{\mathbf{V}}$, $\tilde{E}_T = \tilde{E} + \tilde{V}^2/2$ and $\tilde{P} = (\gamma - 1)\tilde{\bar{\rho}}\tilde{E} = (\gamma - 1)[\tilde{U}_5 - \tilde{U}_1^{-1}(\tilde{U}_2^2 + \tilde{U}_3^2 + \tilde{U}_4^2)/2]$ are the time-dependent fluid density, relative velocity, relative specific total internal energy, and pressure, respectively, and δ_{ij} is the Kronecker delta. As a convenience, we have expressed the flux vectors $\tilde{\mathbf{F}}_{x_j}$ as explicit functions of the state variables $\tilde{U}_i$, $i = 1, 2 \ldots, 5$, and the source term vector $\tilde{\mathbf{S}}$ as an explicit function of the $\tilde{U}_i$ and the spatial coordinates x_i, $i = 1, 2, 3$, but these vectors could also be defined directly in terms of the primitive fluid dynamic variables $\tilde{\bar{\rho}}$, $\tilde{V}_{x_j}$, $j = 1, 2, 3$, $\tilde{E}_T$ and $\tilde{P}$.

Equation (3.1) applies in a reference frame that rotates at constant angular velocity $\boldsymbol{\Omega}$. Thus, the time derivative, d/dt, the Cartesian spatial coordinates, (x_1, x_2, x_3) and the

velocities $\dot{\mathcal{R}}$ and $\tilde{\mathbf{V}}$ are measured relative to an observer fixed in this frame. However, if we set $\mathbf{\Omega} \equiv \mathbf{0}$, and replace the foregoing relative flow quantities by their absolute counterparts, we recover an integral conservation equation that applies in the stationary or inertial frame of reference.

Local Field Equations

After interchanging the order of time differentiation and volume integration in equation (3.1), converting the surface integral to a volume integral, and taking the limit of the resulting volume integrals as $\mathcal{V}(t) \to 0$, we arrive at a differential equation, i.e.,

$$\partial\tilde{\mathbf{U}}/\partial t\Big|_{\mathbf{x}} + \partial\tilde{\mathbf{F}}_{x_j}/\partial x_j = \tilde{\mathbf{S}} \ . \tag{3.3}$$

that governs the inviscid fluid motion at the field points, $\mathbf{x}$, within the fluid domain, at which this motion is continuous and differentiable. In addition, if we choose a volume that contains a surface at which the fluid variables are discontinuous, and take the limits of the terms in (3.1) as this volume collapses into the surface of discontinuity, we determine jump conditions, i.e.,

$$[\![\mathbf{F}_{x_j} - \tilde{\mathbf{U}}\dot{\mathcal{R}}_{x_j}]\!]n_{x_j} = 0 \quad \text{for} \quad \mathbf{x} \in \mathcal{W}_n \quad \text{or} \quad \mathbf{x} \in \mathcal{S}h_n \ , \tag{3.4}$$

that apply at vortex-sheet wakes, $\mathcal{W}_n$, and at shocks, $\mathcal{S}h_n$. Here $[\![\ \ ]\!]$ denotes the jump in a flow quantity across a surface of discontinuity and $\dot{\mathcal{R}}$ is the surface velocity. In principle, jump conditions should be imposed explicitly in fluid dynamic calculations, but the usual procedure is to solve conservative forms of the governing equations, e.g., (3.1) or (3.3), over the entire fluid domain and apply special discretization techniques in an attempt to "capture" wake and shock phenomena.

Equations (3.1) and (3.3) apply over a fluid domain that rotates with the blade row and vibrates with the blading. We will also require a field equation, expressed in terms of cylindrical coordinates, i.e.,

$$\frac{\partial\tilde{\mathbf{U}}^{\mathrm{cyl}}}{\partial t}\bigg|_{\mathbf{x}} + r^{-1}\frac{\partial r\tilde{\mathbf{F}}_r}{\partial r} + r^{-1}\frac{\partial\tilde{\mathbf{F}}_\theta}{\partial\theta} + \frac{\partial\tilde{\mathbf{F}}_\xi}{\partial\xi} = \tilde{\mathbf{S}} \ , \tag{3.5}$$

that applies at fixed locations in the rotating frame, to determine approximate solutions for the unsteady flows far upstream ($\xi < \xi_-$) and far downstream ($\xi > \xi_+$) from a blade row. The state and source-term vectors in (3.5) are given by

$$\tilde{\mathbf{U}}^{\mathrm{cyl}} = \begin{Bmatrix} \tilde{\bar{\rho}} \\ \tilde{\bar{\rho}}\tilde{V}_r \\ \tilde{\bar{\rho}}\tilde{V}_\theta \\ \tilde{\bar{\rho}}\tilde{V}_\xi \\ \tilde{\bar{\rho}}\tilde{E}_T \end{Bmatrix}, \qquad \tilde{\mathbf{S}} = r^{-1}\begin{Bmatrix} 0 \\ (\tilde{U}_3^{\mathrm{cyl}})^2/\tilde{U}_1^{\mathrm{cyl}} + \tilde{P} \\ -\tilde{U}_2^{\mathrm{cyl}}\tilde{U}_3^{\mathrm{cyl}}/\tilde{U}_1^{\mathrm{cyl}} \\ 0 \\ 0 \end{Bmatrix} + \Omega\begin{Bmatrix} 0 \\ 2\tilde{U}_3^{\mathrm{cyl}} + \tilde{U}_1^{\mathrm{cyl}}\Omega r \\ -2\tilde{U}_2^{\mathrm{cyl}} \\ 0 \\ \tilde{U}_2^{\mathrm{cyl}}\Omega r \end{Bmatrix}, \tag{3.6}$$

and the flux vectors $\tilde{\mathbf{F}}_r(\tilde{\mathbf{U}}^{\mathrm{cyl}})$, $\tilde{\mathbf{F}}_\theta(\tilde{\mathbf{U}}^{\mathrm{cyl}})$ and $\tilde{\mathbf{F}}_\xi(\tilde{\mathbf{U}}^{\mathrm{cyl}})$ and the pressure $P(\tilde{\mathbf{U}}^{\mathrm{cyl}})$ have the same functional forms as those indicated, previously [cf. (3.2)] for $\tilde{\mathbf{F}}_{x_1}(\tilde{\mathbf{U}})$, $\tilde{\mathbf{F}}_{x_2}(\tilde{\mathbf{U}})$, $\tilde{\mathbf{F}}_{x_3}(\tilde{\mathbf{U}})$ and $\tilde{P}(\tilde{\mathbf{U}})$.

Boundary Conditions

The foregoing fluid-dynamic field equations must be supplemented by conditions on the flow at the blade surfaces, the duct walls, and at the inflow ($\xi = \xi_-$) and outflow ($\xi = \xi_+$) boundaries of the computational domain. Flow tangency conditions, i.e.,

$$(\tilde{\mathbf{V}} - \dot{\boldsymbol{\mathcal{R}}}) \cdot \mathbf{n} = 0 \quad \text{for} \quad \mathbf{x} \in \mathcal{B}_n \quad \text{and} \quad \tilde{\mathbf{V}} \cdot \mathbf{n} = 0 \quad \text{for} \quad r = r_H, r_D \ , \tag{3.7}$$

apply at the moving blade surfaces and at the stationary duct walls, respectively. In addition, temporally- and circumferentially-averaged values of the total pressure, the total temperature and the inlet flow angle are specified as functions of radius at the inflow boundary, and the circumferentially- and temporally-averaged pressure is specified at the outflow boundary, consistent with radial equilibrium. The unsteady fluctuations at inlet and exit that carry energy towards the blade row must also be specified; those that carry energy away from the blade row must be determined as part of the unsteady solution.

3.2 Linearized Unsteady Aerodynamic Model

We proceed to develop the linearized aerodynamic equations for unsteady flows, that occur at a single temporal frequency, ω, relative to an observer fixed in the rotating frame. The unsteady excitations are assumed to be of small amplitude (e.g., $|\boldsymbol{\mathcal{R}}_{B_n}| \sim \mathcal{O}(\epsilon) << 1$); hence, the unsteady part of the inviscid flow can be approximated as a first-order (in ϵ) perturbation of an underlying nonlinear background flow that is steady in the rotating frame of reference.

The linearized model offers several computational advantages. First, since the unsteady excitations are harmonic in time, the first-order unsteady flow properties will have harmonic time-dependence. Thus, physical time dependence can be removed from the linearized unsteady boundary value problem. Second, as a consequence of our assumptions regarding rotor geometry, inlet and exit mean-flow conditions, and the temporal and circumferential behaviors of the unsteady excitations, the steady background flow will be periodic from blade-to-blade, and the first-order unsteady flow will exhibit a phase-lagged, blade-to-blade periodicity. Such conditions allow numerical resolutions of the steady and linearized unsteady flows to be limited to a single, extended, blade-passage region, i.e., a region of angular pitch $\Delta\theta = 2\pi/N_B$. Finally, since the steady background flow far from the blade row is at most a small perturbation from an axisymmetric swirling flow, unsteady far-field solutions can be constructed and matched to a numerical near-field solution to further reduce the computational domain to one of finite extent in the axial-flow direction.

Series Expansions

To determine the linearized unsteady aerodynamic equations, we first expand the unsteady state vector, $\tilde{\mathbf{U}}$, into an asymptotic series of the form [HC93a, Gil93]

$$\tilde{\mathbf{U}}[\mathbf{x}(\bar{\mathbf{x}}, t), t] = \mathbf{U}(\bar{\mathbf{x}}) + \tilde{\mathbf{u}}[\mathbf{x}(\bar{\mathbf{x}}, t), t] + \ldots = \mathbf{U}(\bar{\mathbf{x}}) + Re\{\mathbf{u}(\bar{\mathbf{x}}) \exp(i\omega t)\} + \ldots \ , \tag{3.8}$$

where the column vectors $\mathbf{U}(\bar{\mathbf{x}}) \sim \mathcal{O}(1)$ and $\tilde{\mathbf{u}}[\mathbf{x}(\bar{\mathbf{x}}, t), t] \sim \mathcal{O}(\epsilon)$ contain the conservation variables for the steady background flow at $\bar{\mathbf{x}}$ and the first-order unsteady flow at $\mathbf{x} =$

$\bar{\mathbf{x}} + \boldsymbol{\mathcal{R}}(\bar{\mathbf{x}}, t)$, respectively, and the dots refer to higher order terms. The components of the vector $\mathbf{u}$ are the complex amplitudes of the first-order unsteady conservation variables, i.e.,

$$\mathbf{u}^T = [\rho \ , \ \bar{\rho}v_{x_1} + \rho V_{x_1} \ , \ \bar{\rho}v_{x_2} + \rho V_{x_2} \ , \ \bar{\rho}v_{x_3} + \rho V_{x_3} \ , \ \bar{\rho}e_T + \rho E_T] \tag{3.9}$$

where $\bar{\rho}$, $\mathbf{V}$ and E_T and ρ, $\mathbf{v}$, and e_T are the steady and the complex amplitudes of the first-order unsteady, primitive flow variables, respectively.

The unsteady flux $\tilde{\mathbf{F}}_{x_j}$ and source term, $\tilde{\mathbf{S}}$, vectors can be approximated using Taylor series expansions about the mean flow state, $\mathbf{U}$, and the reference spatial location, $\bar{\mathbf{x}}$, i.e.,

$$\tilde{\mathbf{F}}_{x_j}(\tilde{\mathbf{U}}) = \mathbf{F}_{x_j}(\mathbf{U}) + \frac{\partial \mathbf{F}_{x_j}}{\partial \mathbf{U}}\tilde{\mathbf{u}} + \dots \quad \text{and} \quad \tilde{\mathbf{S}}(\tilde{\mathbf{U}}, \mathbf{x}) = \mathbf{S}(\mathbf{U}, \bar{\mathbf{x}}) + \frac{\partial \mathbf{S}}{\partial \mathbf{U}}\tilde{\mathbf{u}} + (\boldsymbol{\mathcal{R}} \cdot \boldsymbol{\nabla}_{\bar{\mathbf{x}}})\mathbf{S} + \dots \ . \tag{3.10}$$

Here, $\partial \mathbf{F}_{x_j}/\partial \mathbf{U} = \{\partial F_{i,x_j}/\partial U_k\}$ and $\partial \mathbf{S}/\partial \mathbf{U} = \{\partial S_i/\partial U_k\}$ are Jacobian matrices and the subscripts i and k refer to the ith row and kth column, respectively, of these matrices.

We have expressed the nonlinear fluid dynamic equations (3.1) and (3.3) in terms of the moving control volume, $\mathcal{V}$, which is bounded by the surface $\mathcal{A}$, and the moving spatial coordinate $\mathbf{x}$, respectively. However, because of dependent variable expansions of the form (3.8), the corresponding steady and linearized unsteady equations are more conveniently expressed in terms of the corresponding fixed quantities $\bar{V}$, $\bar{A}$ and $\bar{\mathbf{x}}$, which describe the mean or steady-state positions of $\mathcal{V}$, $\mathcal{A}$ and $\bar{\mathbf{x}}$, respectively. To within first-order in ϵ, the required spatial transformation relations are

$$d\mathcal{V} = [1 + \partial R_m/\partial \bar{x}_m \exp(i\omega t)]d\bar{V} + \dots \ , \quad \mathbf{n}d\mathcal{A} = \bar{\mathbf{n}}d\bar{A} + \Delta(\bar{\mathbf{n}}d\bar{A})\exp(i\omega t) + \dots \ ,$$

and

$$\partial \ /\partial x_j = \ \partial \ /\partial \bar{x}_j - (\partial R_{x_m}/\partial \bar{x}_j)\exp(i\omega t)\partial \ /\partial \bar{x}_m + \dots \tag{3.11}$$

where $\bar{\mathbf{n}}$ is the unit outward normal vector to the control surface $\bar{A}$, and $\Delta(\bar{\mathbf{n}}d\bar{A})$ is the complex amplitude of the first-harmonic component of $\mathbf{n}d\mathcal{A} - \bar{\mathbf{n}}d\bar{A}$. Also, to within first order in ϵ, the local time derivative $\partial/\partial t|_{\mathbf{x}}$ transforms according to

$$\partial \ /\partial t|_{\mathbf{x}} = \partial \ /\partial t|_{\bar{\mathbf{x}}} - i\omega R_{x_m}\exp(i\omega t)\partial \ /\partial \bar{x}_m + \dots \ . \tag{3.12}$$

The Steady and Linearized Unsteady Equations

The equations that govern the zeroth-order steady and the first-order unsteady flows are obtained by substituting the series expansions (3.8), (3.10), (3.11) and (3.12) into the nonlinear governing equations; equating terms of like power in ϵ; and neglecting terms of second and higher order in ϵ. This procedure leads to nonlinear and linear variable-coefficient equations, respectively, for the zeroth- and first-order flows. The variable coefficients that appear in the linearized equations depend upon the underlying steady background flow.

The conservation equation for the steady background flow is

$$\int_{\bar{A}} \mathbf{F}_j n_{x_j} d\bar{A} = \int_{\bar{V}} \mathbf{S} d\bar{V} \quad \text{or} \quad \partial \mathbf{F}_{x_j}/\partial \bar{x}_j = \mathbf{S} \ . \tag{3.13}$$

In addition, the flow tangency condition,

$$\mathbf{V} \cdot \mathbf{n} = 0 \ , \quad \text{for} \quad \bar{x} \in B_n \ , \ r = r_H \text{ and } r = r_D \tag{3.14}$$

applies at the reference blade surfaces and at the duct walls, and periodic conditions on the steady flow variables; e.g.,

$$\bar{\rho}(\bar{r},\bar{\theta}+2\pi n/N_B,\bar{\xi})=\bar{\rho}(\bar{r},\bar{\theta},\bar{\xi}) \quad \text{and} \quad \mathbf{V}(\bar{r},\bar{\theta}+2\pi n/N_B,\bar{\xi})=\mathbf{T}_n\mathbf{V}(\bar{r},\bar{\theta},\bar{\xi}) \tag{3.15}$$

apply upstream and downstream of the blade row. Finally, circumferentially averaged values of the appropriate steady flow variables are specified as functions of radius at the inflow and outflow boundaries and circumferential harmonics of these variables are allowed to evolve to values that are consistent with a blade row operating within an infinite annular duct.

The conservation equation that governs the first-harmonic unsteady perturbation can be written as

$$\begin{aligned} i\omega\int_{\bar{V}}\mathbf{u}d\bar{V}+\int_{\bar{A}}\left(\frac{\partial\mathbf{F}_j}{\partial\mathbf{U}}\mathbf{u}\right)\bar{n}_{x_j}d\bar{A}-\int_{\bar{V}}\frac{\partial\mathbf{S}}{\partial\mathbf{U}}\mathbf{u}d\bar{V}&=-\int_{\bar{V}}i\omega\left(\frac{\partial R_{x_m}}{\partial\bar{x}_m}\right)\mathbf{U}d\bar{V}\\ &+\int_{\bar{A}}\left[i\omega R_{x_j}\mathbf{U}\bar{n}_{x_j}d\bar{A}-\mathbf{F}_j\Delta(\bar{\mathbf{n}}d\bar{A})\right]+\int_{\bar{V}}\frac{\partial}{\partial\bar{x}_j}(R_{x_j}\mathbf{S})d\bar{V}\ , \end{aligned} \tag{3.16a}$$

or

$$\begin{aligned} i\omega\mathbf{u}\ +\ \frac{\partial}{\partial\bar{x}_j}\left(\frac{\partial\mathbf{F}_{x_j}}{\partial\mathbf{U}}\mathbf{u}\right)-\frac{\partial\mathbf{S}}{\partial\mathbf{U}}\mathbf{u}&=-i\omega\frac{\partial R_{x_m}}{\partial\bar{x}_m}\mathbf{U}\\ +\ \frac{\partial}{\partial\bar{x}_j}\left[i\omega R_{x_j}\mathbf{U}+\frac{\partial R_{x_j}}{\partial\bar{x}_m}\mathbf{F}_{x_m}-\frac{\partial R_{x_m}}{\partial\bar{x}_m}\mathbf{F}_{x_j}\right]&+\frac{\partial}{\partial\bar{x}_j}(R_{x_j}\mathbf{S})\ , \end{aligned} \tag{3.16b}$$

respectively, where the terms on the right-hand side, which depend explicitly on the displacement field $\mathbf{R}$, are regarded as known source terms.

The linearized flow tangency condition,

$$\mathbf{v}\cdot\bar{\mathbf{n}}=i\omega\mathbf{R}\cdot\bar{\mathbf{n}}+\mathbf{V}\cdot\boldsymbol{\nabla}(\mathbf{R}\cdot\bar{\mathbf{n}}),\ \text{for}\ \bar{\mathbf{x}}\in B_n\ ,\ r=r_H\ \text{and}\ r=r_D\ , \tag{3.17}$$

applies at the blade surfaces and at the duct walls, and phase-lagged periodicity conditions, e.g.,

$$\rho(\bar{r},\bar{\theta}+2\pi n/N_B\ ,\bar{\xi})=\rho(\bar{r},\bar{\theta},\bar{\xi}) \quad \text{and} \quad \mathbf{v}(\bar{r},\bar{\theta}+2\pi n/N,\bar{\xi})=\mathbf{T}_n\mathbf{v}(\bar{r},\bar{\theta},\bar{\xi})\exp(in\sigma)\ , \tag{3.18}$$

apply upstream and downstream of the blade row. The far-field conditions imposed in the unsteady problem must allow for the prescription of external unsteady aerodynamic excitations and permit unsteady disturbances coming from within the solution domain to pass through the computational inlet (at $\xi=\xi_-$) and exit (at $\xi=\xi_+$) boundaries without reflection.

In addition to the differential equations in (3.13) and (3.16), we also require field equations that will allow us to develop approximate analytical representations for the steady and unsteady flows far upstream ($\xi<\xi_-$) and far downstream ($\xi>\xi_+$) of a blade row. In particular, we will require equations, expressed in cylindrical coordinates, that describe the steady background flow and the first-order unsteady perturbation at fixed points, $\mathbf{x}=\bar{\mathbf{x}}$, in the rotating frame. After transforming the differential equations in (3.13) and (3.16) to

cylindrical coordinates, or, alternatively, after applying the series expansions (3.8) and (3.10) to the nonlinear, time-dependent equation (3.5), and setting $\mathbf{R} \equiv \mathbf{0}$, we find that

$$r^{-1}\frac{\partial r\mathbf{F}_r}{\partial r} + r^{-1}\frac{\partial \mathbf{F}_\theta}{\partial \theta} + \frac{\partial \mathbf{F}_\xi}{\partial \xi} = \mathbf{S} \tag{3.19}$$

and

$$i\omega\mathbf{u} + r^{-1}\frac{\partial(r\mathbf{A}\mathbf{u})}{\partial r} + r^{-1}\frac{\partial \mathbf{B}\mathbf{u}}{\partial \theta} + \frac{\partial \mathbf{C}\mathbf{u}}{\partial \xi} - \mathbf{D}\mathbf{u} = 0\ . \tag{3.20}$$

Here, $\mathbf{A} = \partial\mathbf{F}_r\ /\partial\mathbf{U}^{\text{cyl}}$, $\mathbf{B} = \partial\mathbf{F}_\theta\ /\partial\mathbf{U}^{\text{cyl}}$ and $\mathbf{C} = \partial\mathbf{F}_\xi\ /\partial\mathbf{U}^{\text{cyl}}$ are flux Jacobian matrices and $\mathbf{D} = \partial\mathbf{S}_r\ /\partial\mathbf{U}^{\text{cyl}}$ is the source-term Jacobian.

Solution Strategy

We require solutions to the nonlinear steady and the linearized unsteady boundary-value problems to predict the unsteady aerodynamic responses of a blade row operating within an annular duct, to various types of unsteady excitation. In the present study, we will employ the nonlinear analysis, TURBO [JHW92], to provide the steady background flow information, required for a linearized unsteady aerodynamic analysis; and seek solutions to the linearized unsteady problem by matching a wave-split, finite-volume analysis for the unsteady perturbation in the near field, i.e., in the region $\xi_- \le \xi \le \xi_+$, to approximate solutions for the unsteady perturbations of fully-developed, axisymmetric, mean flows in the regions far upstream ($\xi \le \xi_-$) and far downstream ($\xi \ge \xi_+$) of the blade row. Thus, we will solve the integral form (3.16b) of the linearized unsteady field equation in the near field, and a reduced form of the differential equation (3.20) in the far-field.

In the near-field, finite-volume analysis, it is advantageous to regard the state vector $\mathbf{u}$ as pseudo time dependent, i.e., to set $\mathbf{u} = \mathbf{u}(\bar{\mathbf{x}}, \tau)$, where τ is the pseudo time variable, and add the term $\partial(\int_{\bar{V}} \mathbf{u} d\bar{V})/\partial\tau$ to the left-hand side of equation (3.16b). This allows conventional time-marching algorithms to be used to converge the solution for the complex amplitude of the unsteady state vector to a steady-state value.

Also, the complex-amplitude of the displacement field, $\mathbf{R}(\bar{\mathbf{x}})$, must be prescribed over the entire solution domain. In the present study, this field is defined so that the solution domain deforms with the blade motion (i.e., $\mathbf{R}(\bar{\mathbf{x}}) = \mathbf{R}_{\mathrm{B}_n}(\bar{\mathbf{x}})$ for $\bar{\mathbf{x}} \in \mathrm{B}_n$), slides along the hub and duct walls ($\mathbf{R}(\bar{\mathbf{x}}) \cdot \mathbf{e}_r = 0$ for $\bar{r} = r_H, r_D$), and remains rigid far from the blade row ($\mathbf{R}(\bar{\mathbf{x}}) \equiv \mathbf{0}$ for $\bar{\xi} \lesseqgtr \bar{\xi}_\mp$). In addition, $\mathbf{R}(\bar{\mathbf{x}})$ is prescribed along one blade-to-blade periodic boundary, such that it is continuous at the blade leading and trailing edges and decays exponentially away from the blade row. At the other boundary, $\mathbf{R}$ is set so as to satisfy phase-lagged periodicity, cf. (3.15). The function $\mathbf{R}(\bar{\mathbf{x}})$ is determined, first, along the hub and duct walls, and then, in the interior of the computational domain as solutions of Laplace's equation, $\nabla^2_{\bar{\mathbf{x}}}\mathbf{R} = \mathbf{0}$, subject to the appropriate Dirichlet boundary conditions, given above. Note that for unsteady flows in which no blades vibrations occur, we simply set $\mathbf{R} \equiv \mathbf{0}$.

The linearized far-field analysis is described in §4 of this report; the near-field, finite-volume analysis, in §5. These have been coupled and implemented into the LINFLUX code, which is demonstrated via the numerical results in presented §6.

4. Unsteady Perturbations in the Far-Field

Analytical descriptions of the linearized unsteady flows in the regions far upstream ($\xi < \xi_-$) and far downstream ($\xi > \xi_+$) from a blade row can be applied to restrict the near-field computational domain to one of finite extent in the axial-flow direction. Such decriptions are based on reduced sets of governing equations. They allow unsteady disturbances that enter the computational domain (excitations) to be prescribed as approximate solutions to the linearized governing equations and render the computational inflow and outflow boundaries transparent to outgoing waves.

This approach has been applied successfully in two-dimensional unsteady flow calculations [Ver89b], wherein exact solutions for the linear unsteady perturbations of uniform mean flows are matched to numerical near-field solutions at the computational inflow ($\xi = \xi_-$) and outflow ($\xi = \xi_+$) boundaries. Unfortunately, exact solutions for three-dimensional unsteady disturbances are only available for the special case of a uniform, absolute, steady-background flow. Thus, at present, approximate far-field conditions must be applied in computational simulations of more general three-dimensional flows. For example, analytic two-dimensional solutions have been applied in radial strips [SG91]. This quasi three-dimensional approach can be useful for blade flutter applications, and it is easy to implement. However, since the true radial behaviors of the unsteady disturbances are not taken into account, realistic three-dimensional, unsteady aerodynamic excitations cannot be prescribed, and the mismatches that exist between the near- and far-field solutions can cause nonphysical or spurious reflections of outgoing disturbances.

The approach taken here is a similar, but expanded, version of that adopted in [HLC93]. In particular, we propose approximate representations for the three-dimensional unsteady perturbations of a fully-developed, axisymmetric, swirling, mean flow. These representations describe the behaviors of the convected and the modal or wave-type unsteady disturbances that exist far upstream and far downstream of a blade row operating within a cylindrical annular duct. The fundamental unsteady disturbances are assumed to vary harmonically in time and in the circumferential direction and exponentially in the axial direction. The axial exponential coefficients and the radial distributions of the modal disturbances are determined by solving a far-field eigenvalue problem numerically. The resulting far-field solutions are then used to prescribe incoming unsteady aerodynamic excitations and, by matching the analytic far-field solutions to a numerical near-field solution, to determine the amplitudes of the outgoing waves.

We assume that, far from the blade row, the mean or steady flow quantities are dependent only on radial position, i.e., $\bar{\rho} = \bar{\rho}(r)$, $P = P(r)$, etc., and that the radial component of the steady velocity is negligible, i.e.,

$$\mathbf{V} \approx V_\theta(r)\mathbf{e}_\theta + V_\xi(r)\mathbf{e}_\xi \ . \tag{4.1}$$

Under these conditions, the steady field equation (3.19) reduces to

$$\bar{\rho}^{-1}\frac{dP}{dr} = r^{-1}V_\theta^2 + 2\Omega V_\theta + \Omega^2 r \ . \tag{4.2}$$

Equation (4.2) must be satisfied to ensure that radial momentum is conserved in the steady background flow. We also assume that the velocity and the thermodynamic information

needed to completely determine the steady background flow in the far field are known. Equation (4.2) can then be combined with the appropriate thermodynamic relations to determine the remaining mean-flow thermodynamic properties. For example, if the mean flow is isentropic, and the steady pressure and density are specified at some reference radial station, say at $r = r_{\text{ref}}$, we can combine (4.2) with the thermodynamic relations $P\bar{\rho}^{-\gamma} = (P\bar{\rho}^{-\gamma})_{\text{ref}}$ and $E = (\gamma - 1)^{-1} P\bar{\rho}^{-1}$ to obtain

$$\frac{\gamma}{\gamma - 1}(P\bar{\rho}^{-\gamma})^{1/\gamma} \frac{dP^{(\gamma-1)/\gamma}}{dr} = \frac{\gamma}{\gamma - 1}(P\bar{\rho}^{-\gamma})\frac{d\bar{\rho}^{\gamma-1}}{dr} = \gamma \frac{dE}{dr} = r^{-1}V_\theta^2 + 2\Omega V_\theta + \Omega^2 r \ . \quad (4.3)$$

Similar, but slightly more complicated relationships, hold for non-isentropic mean flows.

For the mean flow conditions just described, the linearized unsteady equation (3.20) can be reduced to

$$i\omega \mathbf{u} + r^{-1}\frac{\partial(r\mathbf{A}_2\mathbf{u})}{\partial r} + r^{-1}\mathbf{B}_2\frac{\partial \mathbf{u}}{\partial \theta} + \mathbf{C}_2\frac{\partial \mathbf{u}}{\partial \xi} - \mathbf{D}\mathbf{u} = 0 \ , \quad (4.4)$$

where the subscript 2 on the Jacobian matrices in (4.4) indicates that they are evaluated at $U_2^{\text{cyl}} = 0$, e.g., $\mathbf{A}_2 \equiv \partial \mathbf{F}_r / \partial \mathbf{U}^{\text{cyl}}|_{U_2^{\text{cyl}}=0}$.

4.1 Uniform Mean Flow

For the special case of a uniform mean flow in the absolute frame, i.e., $\mathbf{V}^{\text{abs}} = V_\xi^{\text{abs}} \mathbf{e}_\xi$, where V_ξ^{abs} and the mean-flow thermodynamic properties are constant, an exact solution can be determined for the first-order unsteady perturbation. In particular, the linearized unsteady equations (4.4) can be recast as a system of uncoupled equations [VMK95] for the first-order unsteady entropy, $\tilde{s}$, vorticity, $\tilde{\boldsymbol{\zeta}} = \boldsymbol{\nabla} \times \tilde{\mathbf{v}}$, and pressure, $\tilde{p}$, of the form

$$\frac{\bar{D}\tilde{s}}{Dt} = 0 \ , \quad \frac{\bar{D}\tilde{\boldsymbol{\zeta}}}{Dt} + \boldsymbol{\Omega} \times \tilde{\boldsymbol{\zeta}} = 0 \ , \quad \text{and} \quad \frac{\bar{D}^2\tilde{p}}{Dt^2} - A^2 \boldsymbol{\nabla}^2 \tilde{p} = 0 \ , \quad (4.5)$$

where $\bar{D}/Dt = \partial/\partial t + V_\xi \partial/\partial \xi + V_\theta r^{-1} \partial/\partial \theta$ is a convective derivative operator based on the relative mean-flow velocity, i.e., $\mathbf{V} = \mathbf{V}^{\text{abs}} - \boldsymbol{\Omega} \times \mathbf{r}$, so that $V_\xi = V_\xi^{\text{abs}}$ and $V_\theta = -\Omega r$.

Equations (4.5) indicate that the first-order entropic, vortical and pressure perturbations of a uniform absolute mean flow are independent modes of unsteady fluid motion. Moreover, the entropic and vortical disturbances are convected at the mean flow velocity and therefore, have general solutions of the form

$$\tilde{s} = \tilde{s}(r, r\theta - V_\theta t, \xi - V_\xi t) \quad \text{and} \quad \tilde{\boldsymbol{\zeta}} = \tilde{\boldsymbol{\zeta}}(r, r\theta - V_\theta t, \xi - V_\xi t) \ . \quad (4.6)$$

Finally, the pressure disturbance is governed by a convected wave equation which can also be solved analytically.

For an unsteady flow occurring at temporal frequency ω in the rotating frame, the unsteady entropic and vortical perturbations can be represented as a superposition of harmonic disturbances of the form

$$s(r, \theta, \xi) = \sum_{m=-\infty}^{\infty} s_m(r) \exp[i(\kappa_{\xi,m}\xi + \bar{m}\theta)] \ , \quad (4.7)$$

and

$$\zeta(r,\theta,\xi) = \sum_{m=-\infty}^{\infty} \zeta_m(r) \exp[i(\kappa_{\xi,m}\xi + \bar{m}\theta)] \ . \tag{4.8}$$

Here s and ζ are the complex amplitudes of the unsteady entropic and vortical fluctuations, $s_m(r)$ and $\zeta_m(r)$ describe the radial behaviors of the fluctuations in the $\bar{m}$th circumferential mode, $\bar{m} = N_D + mN_B$ is a circumferential angular wave number which represents the number of complete cycles or "lobes" in the mth convected disturbance over the interval $0 \leq \theta \leq 2\pi$, and $\kappa_{\xi,m}$ is the axial wave number of the mth disturbance. The temporal frequency of an mth convected disturbance as seen by an observer fixed in the absolute frame is given by $\omega_m^{\text{abs}} = \omega - \bar{m}\Omega_x$, and it follows from the convection equations in (4.5) that $\kappa_{\xi,m} = -(\omega - \bar{m}\Omega_x)V_\xi^{-1} = -\omega_m^{\text{abs}} V_\xi^{-1}$.

A solution for the first-order unsteady pressure disturbance can be determined by solving the convected wave equation in (4.5), using the method of separation of variables [TS62, VTM82]. The resulting solution for the complex-amplitude of the unsteady pressure perturbation is

$$p(r,\theta,\xi) = \sum_{m=-\infty}^{\infty} \left(\sum_{\mu=0}^{\infty} a_{m\mu}^{\mp} [J_{\bar{m}}(k_{m\mu}r) + Q_{m\mu} Y_{\bar{m}}(k_{m\mu}r)] \exp(\chi_{m\mu}^{\mp}\xi) \right) \exp(i\bar{m}\theta) \ . \tag{4.9}$$

Here $a_{m\mu}^{\mp}$, $Q_{m\mu}$ and $k_{m\mu}$ are constants, $J_{\bar{m}}$ and $Y_{\bar{m}}$ are Bessel functions, of order $\bar{m}$, of the first and second kinds, respectively, and the acoustic modes are ordered so that the index $\mu = 0, 1, 2, \ldots$ indicates the number of zero crossings or radial nodes in the μth radial mode. The constants, $k_{m\mu}$ and $Q_{m\mu}$, in (4.9) are determined by the boundary conditions at the duct walls, e.g., see (3.17), and

$$\chi_{m\mu}^{\mp} = \beta_{m\mu}^{\mp} + i\kappa_{\xi,m\mu}^{\mp} = (1 - M_\xi^2)^{-1} \left[iM_\xi \omega_m^{\text{abs}}/A \mp [(1 - M_\xi^2)k_{m\mu}^2 - (\omega_m^{\text{abs}}/A)^2]^{1/2} \right] , \tag{4.10}$$

where $M_\xi = V_\xi/A < 1$ and A are the axial Mach number and speed of sound propagation in the steady background flow, respectively, and $\omega_m^{\text{abs}} = \omega - \bar{m}\Omega$ is the absolute frequency of the unsteady pressure disturbances in the mth circumferential mode.

The $-$ and $+$ superscripts in the foregoing equations indicate that there are two components of the $m\mu$th pressure pattern. If $\omega_m^{\text{abs}}/A > (1 - M_\xi^2)^{1/2} k_{m\mu}$, then the $\chi_{m\mu}^{\mp}$ are purely imaginary, and the two components describe propagating acoustic disturbances. If $\omega/A_m^{\text{abs}} < (1 - M_\xi^2)k_{m\mu}$, then $\chi_{m\mu}^{\mp}$ are complex, and one component decays, whereas the other grows exponentially with increasing distance along the duct. The appropriate sign, $-$ or $+$, to be used is determined by the conditions imposed on the $m\mu$th acoustic disturbance. The minus sign describes an acoustic wave that propagates downstream or attenuates with increasing distance downstream; the plus sign, a wave that propagates upstream or attenuates with increasing distance upstream. Thus, for example, for subsonic ($M_\xi < 1$) axial mean flow, the minus sign must be selected to describe an acoustic excitation coming from upstream of a blade row; the plus sign, to describe an acoustic excitation coming from downstream.

4.2 Mean Flows with Swirl and Axial Shear

For nonuniform mean flows in which the fluid absolute velocity and thermodynamic properties vary with radius, it is not possible to determine exact solutions for the first-order unsteady flow variables. However, guided by the solutions determined for uniform mean flows, we can presuppose approximate solutions to (4.4), for the unsteady perturbations associated with a blade row operating within a cylindrical annular duct. In particular, we set $\tilde{\mathbf{u}} = \tilde{\mathbf{u}}_C + \tilde{\mathbf{u}}_W$, where $\tilde{\mathbf{u}}_C$ describes a purely convected disturbance field, and has a general solution of the form

$$\tilde{\mathbf{u}}_C = \tilde{\mathbf{u}}_C(r, r\theta - V_\theta t, \xi - V_\xi t) \ , \tag{4.11}$$

and $\tilde{\mathbf{u}}_W$ describes convected-wave or modal type disturbances, and has a solution of the form

$$\tilde{\mathbf{u}}_W = \mathrm{Re}\{\mathbf{u}_W \exp(i\omega t)\} = \mathrm{Re}\left\{\left(\sum_{m=-\infty}^{\infty}\sum_{n=0}^{\infty} a_{mn}\mathbf{u}^R_{mn}(r)\exp(\chi_{mn}\xi + i\bar{m}\theta)\right)\exp(i\omega t)\right\} \ , \tag{4.12}$$

where $\mathbf{u}^R_{mn}(r)$ defines the radial shape of the mnth mode.

The convected disturbances are solutions of the unsteady equation (4.4) that satisfy the condition, $\bar{D}\tilde{\mathbf{u}}_C/Dt \equiv 0$. As a result, the complex amplitude $\mathbf{u}_C$ of the state vector, $\tilde{\mathbf{u}}_C$, has the form

$$\mathbf{u}_C = \sum_{m=-\infty}^{\infty} \mathbf{u}_{m,C}(r)\exp\{i[\kappa_{\xi,m,C}(r)\xi + \bar{m}\theta]\} \ . \tag{4.13}$$

In general, the axial wave number of the mth convected disturbance, $\kappa_{\xi,m,CV}$, depends on radius, and is given by

$$\kappa_{\xi,m,C}(r) = -[\omega + \bar{m}r^{-1}V_\theta(r)]/V_\xi(r) = -[\omega^{\mathrm{abs}}_m + \bar{m}r^{-1}V^{\mathrm{abs}}_\theta(r)]/V_\xi(r) \ , \tag{4.14}$$

where $\omega^{\mathrm{abs}}_m = \omega - \bar{m}\Omega$ and $V^{\mathrm{abs}}_\theta = V_\theta + \Omega r$. Because of this radial dependency, the solution for the convected disturbances cannot be represented via a modal analysis. It should also be noted that the axial wave numbers of the convected disturbances are independent of radius for the special cases of uniform axial velocity and either solid body swirl ($V_\theta \propto r$) or no swirl.

The wave-type or modal disturbances in (4.12) must be determined as solutions of equation (4.4), subject to the appropriate boundary conditions at the duct walls, e.g., see (3.17). After substituting the modal form of the solution, assumed in (4.12), into these equations, we find that

$$i\omega\mathbf{I}\,\mathbf{u}^R_{mn} + r^{-1}\frac{\partial}{\partial r}\left(r\mathbf{A}_2\,\mathbf{u}^R_{mn}\right) + i\bar{m}r^{-1}\mathbf{B}_2\,\mathbf{u}^R_{mn} + \chi_{mn}\mathbf{C}_2\,\mathbf{u}^R_{mn} - \mathbf{D}_2\,\mathbf{u}^R_{mn} = \mathbf{0} \ . \tag{4.15}$$

The system of equations (4.15) provides an eigenvalue problem for determining the eigenvalues χ_{mn}, and the corresponding right eigenvectors $\mathbf{u}^R_{mn}$ of the far-field, convected-wave type, unsteady disturbances. The exact solutions to (4.15) for uniform mean flows indicate that the wave-type solutions are associated with irrotational unsteady pressure perturbations. For mean flows with swirl and/or axial shear, numerical solutions to (4.15) indicate the existence of a more complicated array of modal or wave-type disturbances.

Numerical Eigensolutions

After discretizing (4.15), by replacing the radial derivative operator by a finite-difference operator and introducing an artificial dissipation term, we find that

$$(\mathbf{P} - \chi_{mn}\mathbf{C}_2)\ \mathbf{u}^R_{mn} = \mathbf{0} \tag{4.16}$$

where

$$\mathbf{P} = -i\omega\mathbf{I} - \mathbf{L}(r, \mathbf{A}_2) - i\bar{m}r^{-1}\ \mathbf{B}_2 + \mathbf{D}_2 + \epsilon_4\delta_4\mathbf{I}\ . \tag{4.17}$$

Here, the column vector $\mathbf{u}^R_{mn}$ contains an entry for each of the five conservation variables at each radial discretization point, $\mathbf{L}(r, \mathbf{A}_2)$ is a finite difference approximation to $r^{-1}\partial(r\mathbf{A}_2\mathbf{u}^R_{mn})/\partial r$, and $\epsilon_4\delta_4$ is a dissipation term, which has been included to suppress odd-even decoupling. The dissipation term is based on fourth-order radial differencing and the coefficient ϵ_4 is used to control the amount of added dissipation.

The complex, non-Hermetian, generalized eigenvalue problem (4.16) can be solved, using a standard linear algebra routine, to determine the axial eigenvalues, χ_{mn}, and the associated right eigenvectors, $\mathbf{u}^R_{mn}(r)$, that describe the modal unsteady perturbations in the far field. The left eigenvectors, $\mathbf{u}^L_{mn}$, are determined as a solution to the equation $(\mathbf{P} - \chi_{mn}\mathbf{C})^H\mathbf{u}^L_{mn} = \mathbf{0}$, where the superscript H indicates the conjugate transpose of a complex matrix. An orthonormal set of left eigenvectors can then be determined by setting $(\mathbf{v}^L_{mn})^H = (\mathbf{u}^L_{mn})^H\mathbf{C}/[(\mathbf{u}^L_{mn})^H\mathbf{C}\mathbf{u}^R_{mn}]$, so that $\langle\mathbf{v}^L_{mp}, \mathbf{u}^R_{mq}\rangle = (\mathbf{v}^L_{mp})^H\mathbf{u}^R_{mq} = \delta_{pq}$, where $\delta_{pq} = 1$ if $p = q$ and $\delta_{pq} = 0$ if $p \neq q$.

Once the eigenvalues and the eigenvectors of (4.15) have been computed, the constants, a_{mn}, in equation (4.12) can be determined from the complex amplitude, $\mathbf{u}_W$, of the superposed wave-type disturbances. After taking the inner product and making use of the orthogonality relations for the left and right eigenvectors, we find that

$$\langle\mathbf{v}^L_{mn}, \mathbf{u}_W\rangle = \sum_{m=-\infty}^{\infty} a_{mn}\exp(\chi_{mn}\xi + i\bar{m}\theta) \tag{4.18}$$

Then, after multiplying both sides of (4.18) by $\exp(-\chi_{mn}\xi - i\bar{m}\theta)$, and integrating the result with respect to θ over the angular pitch, $2\pi/N_B$, of the blading, we obtain the following expression for a_{mn}:

$$a_{mn} = \langle\mathbf{v}^L_{mn}, \frac{N_B}{2\pi}\int_{\theta}^{\theta+2\pi/N_B} \mathbf{u}_W\exp[-(\chi_{mn}\xi + i\bar{m}\theta)]d\theta\rangle\ . \tag{4.19}$$

The group velocity, $V_{g,mn}$, of an unattenuated mnth disturbance, i.e., the velocity at which such a disturbance carries energy, can be determined by differentiating (4.16) with respect to ω and taking inner products between $(\mathbf{v}^L_{mn})^H$ and the terms in the resulting equation. After carrying out the algebra, we find that

$$V_{g,mn} = \frac{\partial\omega}{\partial\chi_{mn}} = \frac{\langle\mathbf{v}^L_{mn}, \mathbf{C}\mathbf{u}^R_{mn}\rangle}{\langle\mathbf{v}^L_{mn}, (\partial\mathbf{P}/\partial\omega)\,\mathbf{u}^R_{mn}\rangle}\ . \tag{4.20}$$

The group velocity can be used to determine the propagation directions of the acoustic disturbance modes.

Classification of Unsteady Disturbances

Unsteady perturbations of uniform mean flows can be represented by a superposition of purely entropic and purely vortical disturbances that are convected by the mean flow, and upstream- and downstream traveling irrotational pressure disturbances. However, for nonuniform mean flows, the situation is more complicated [Kou95]. In particular, for the rotational, but isentropic, mean flows being considered herein, the unsteady entropy is an independent disturbance that is convected by the mean flow, but neither convected purely vortical nor propagating or attenuating purely irrotational acoustic disturbances exist, because of the coupling between vortical and acoustic disturbances caused by mean-flow vorticity. Instead, downstream traveling, nearly-convected, vorticity-dominated disturbances and upstream and downstream traveling, pressure-dominated disturbances occur [GA96]. The nearly-convected disturbances are primarily vortical, but also contain pressure fluctuations. They travel downstream, without attenuation, at speeds slightly less than and slightly greater than the mean flow speed. The propagating or decaying acoustic disturbances also carry unsteady vorticity. Both of these types of disturbances appear as solutions of the eigenvalue problem (4.15).

Thus, we can further decompose the solution for the unsteady state variables by setting

$$\mathbf{u}(r,\theta,\xi) = \mathbf{u}_C(r,\theta,\xi) + \mathbf{u}_A(r,\theta,\xi) + \mathbf{u}_N(r,\theta,\xi) \ , \tag{4.21}$$

where $\mathbf{u}_W = \mathbf{u}_A + \mathbf{u}_N$ and $\mathbf{u}_C$, $\mathbf{u}_A$ and $\mathbf{u}_N$ are the complex amplitudes of the convected, the acoustic and the nearly-convected unsteady disturbances, respectively. The complex amplitude of the state vector for the convected disturbances is described by (4.13).

If we order the acoustic disturbances in (4.21) according to the number of zero crossings or nodes of the radial eigenmode, denoted by the subscript $\mu = 0, 1, 2, \ldots$, the state vector, $\mathbf{u}_A$, can be expressed as

$$\mathbf{u}_A(r,\theta,\xi) = \sum_{m=-\infty}^{\infty} \sum_{\mu=0}^{\infty} a^{\mp}_{m\mu,A} \mathbf{u}^{R,\mp}_{m\mu,A}(r) \exp(\chi^{\mp}_{m\mu,A}\xi + i\bar{m}\theta) \ , \tag{4.22}$$

where the $-$ and $+$ superscripts correspond to the downstream and upstream traveling acoustic disturbances. For subsonic relative flows, $|\mathbf{V}| < A$, the behaviors of the acoustic waves change, with increasing μ and/or $|m|$, from propagating (if any propagating waves exist for the given frequency and number of nodal diameters) to decaying. This implies that the series in (4.22) can be truncated at a finite distance from the blade row, since the high μ or $|\bar{m}|$ acoustic response disturbances will have decayed to negligible levels. This is fortuitous, because only a finite number of disturbance modes can be accurately represented in numerical descriptions of the unsteady perturbations in the far upstream and downstream regions.

As in uniform mean flows, the eigenvalues, $\chi^{\mp}_{m\mu}$, of the $m\mu$th acoustic disturbances are composed of an attenuation coefficient and an axial wave number, i.e., $\chi^{\mp}_{m\mu} = \beta^{\mp}_{m\mu} \mp i\kappa^{\mp}_{\xi,m\mu}$. The $m\mu$th acoustic waves propagate, if the $\chi^{\mp}_{m\mu}$ are purely imaginary; otherwise, these waves grow and decay exponentially in the downstream axial direction. For uniform mean flows the decaying pressure waves occur in pairs at $\kappa^{\mp}_{\xi,m\mu} = \kappa_{\xi,m\mu,\text{cutoff}} = M_\xi \omega^{\text{abs}}_m / A$ [see (4.10)], where $\kappa_{\xi,m\mu,\text{cutoff}}$ is the axial wave number at which cutoff occurs; i.e., the wave number at

which the acoustic behavior changes from propagating to attenuating. For nonuniform mean flows, the decaying pressure waves also occur in pairs, but not at constant values of κ_ξ.

The nearly-convected, vorticity-dominated disturbances can also be ordered by the number of zero crossings in the eigenmode, but in this case starting with $\mu = 1$. Thus, the state vector, $\mathbf{u}_N$, can be expressed as

$$\mathbf{u}_N(r,\theta,\xi) = \sum_{m=-\infty}^{\infty} \sum_{\mu=1}^{\infty} a^{\mp}_{m\mu,N} \mathbf{u}^{R,\mp}_{m\mu,N}(r) \exp[i(\kappa^{\mp}_{\xi,m\mu,N}\xi + \bar{m}\theta)] \ . \tag{4.23}$$

The eigenvalues of the $m\mu$th nearly-convected disturbances are imaginary, i.e., $\chi^{\mp}_{m\mu} = i\kappa^{\mp}_{\xi,m\mu}$ and the $-$ and $+$ superscripts in (4.23) correspond to axial wave numbers that are less than and greater than, respectively, the axial wave numbers of the mth convected disturbance, i.e.,

$$\kappa^{-}_{\xi,m\mu,N} < \kappa_{\xi,m,C}(r) < \kappa^{+}_{\xi,m\mu,N} \ . \tag{4.24}$$

Note that, since the nearly convected waves do not attenuate, it may not be possible to truncate the series (4.23) without introducing error.

Filtering of Unwanted Radial Modes

The numerical solution of equation (4.15) will yield a radial mode for each of the five conservation variables and each radial grid point. For example, if the radial grid used to discretize equation (4.15) consists of 20 points, 100 radial modes will be obtained. Some of these numerically determined modes describe acoustic waves, some describe nearly-convected waves (if the mean flow is nonuniform), some are discrete representations of convected disturbances, and many are spurious solutions which satisfy the discretized equation but not the differential equation. The spurious modes must be filtered out to yield a valid solution set. Typically eight radial modes will be kept to represent acoustic disturbances. These are the upstream and downstream traveling acoustic modes with less than four radial zero crossings. Thus, if no nearly-convected modes exist, over 90% of the numerically determined radial modes are filtered out.

In the present effort, the filtering is based on the number of radial zero crossings, or nodes, and the point-to-point oscillations of each computed radial mode. To prevent aliasing errors, the number of zero crossings, N_Z, in a radial mode is limited; e.g., we set $N_Z \leq (r_D - r_H) \,/\, (4\Delta r_{\max})$, where r_D and r_H are the duct and hub radii, respectively, and $\Delta r_{\max}$ is the maximum spacing in the radial grid. To further eliminate the spurious oscillatory modes that arise from the discretization, the number of crossings about the mean value of the radial mode is also limited in a similar fashion. These filtering criteria have been found to usually yield only the genuine modes, but the filtering algorithm is still under development.

Since only a finite number of modes are retained after the filtering process, the far field modal description may be incomplete. This caveat applies to both the number of circumferential and radial modes. The number of circumferential modes required for acoustic disturbances is determined by the number of cut-on modes. For subsonic tip relative Mach numbers, typically only a few, if any, acoustic modes are cut-on, but for supersonic tip Mach numbers an infinite number of acoustic modes may be cut-on. For frequencies typical of blade flutter, usually only the radial modes having zero crossing are required. For frequencies

typical of blade row interactions, usually only radial modes with less than four nodes are required. The number of radial modes required for nearly-convected waves is unknown at this time.

Since the acoustic and nearly-convected modes are ordered by the number of radial nodes, the number of nodes in each kept numerical mode can be counted to determine if any genuine modes are missing or if spurious modes are being kept. If the number of kept modes with a given number of nodes is one, or two for the nearly convected modes, then it is likely that only the genuine modes have been retained. Based on our numerical results, the exclusion of genuine modes or the inclusion of spurious modes is detrimental to both the accuracy and convergence properties of the LINFLUX analysis.

4.3 Near-Field/Far-Field Matching Procedure

To couple the foregoing far field solutions to a near-field numerical solution for the linearized unsteady flow, the incoming unsteady aerodynamic disturbances (excitations) must be prescribed, and the outgoing disturbances must be determined by matching the far-field descriptions (4.12) and (4.13) to the near-field solution. In particular, the convected entropy and vorticity fields, the nearly-convected vortical waves, and the propagating and attenuating acoustic waves that travel downstream are incoming disturbances at the inflow boundary ($\xi = \xi_-$) of the near-field computational domain and outgoing disturbances at the outflow ($\xi = \xi_+$) boundary. Acoustic waves that travel upstream are incoming disturbances at $\xi = \xi_+$ and outgoing disturbances at $\xi = \xi_-$.

To determine the amplitudes, $a^{\mp}_{m\mu,A}$ and $a^{\mp}_{m\mu,N}$, of the outgoing wave-type disturbances, inner products of the left eigenvectors of the system (4.16) with the near-field solution for the state vector, $\mathbf{u}$ are taken, under the assumption that $\langle \mathbf{v}^L_{m\mu}, \mathbf{u} \rangle \approx \langle \mathbf{v}^L_{m\mu}, \mathbf{u}_W \rangle$. For each outgoing disturbance mode, the amplitude in the mth circumferential and μth radial mode is determined by applying (4.19) at the computational inflow and outflow boundaries, with $\mathbf{u}_W$ replaced by the near-field solution for $\mathbf{u}$ at the computational boundary. Thus, the amplitude, $a^{\mp}_{m\mu}$, is determined by

$$a^{\mp}_{m\mu} = \langle \mathbf{v}^L_{m\mu}, \frac{N_B}{2\pi} \int_{\theta}^{\theta+2\pi/N_B} \mathbf{u}(r, \theta, \xi_{\mp}) \exp[-(\chi^{\mp}_{m\mu}\xi_{\mp} + i\bar{m}\theta)] d\theta \rangle \ . \tag{4.25}$$

The wave-type modes are then sorted into acoustic and nearly-convected modes and superposed to provide solutions for $\mathbf{u}_W$ in the far-upstream and far-downstream regions of the flow, i.e.,

$$\begin{aligned} \mathbf{u}^{\mp}_W(r, \theta, \xi) \ &= \ \sum_{m=-M}^{M} \sum_{\mu=0}^{N} a^{\mp}_{m\mu,A} \mathbf{u}^{R,\mp}_{m\mu,A}(r) \exp(\chi^{\mp}_{m\mu,A}\xi + i\bar{m}\theta) \\ &+ \ \sum_{m=-M}^{M} \sum_{\mu=1}^{N} a^{\mp}_{m\mu,N} \mathbf{u}^{R,\mp}_{m\mu,N}(r) \exp[i(k^{\mp}_{\xi,m\mu,N}\xi + \bar{m}\theta)] \ , \ \xi \lesseqgtr \xi_{\mp} \end{aligned} \tag{4.26}$$

where M and N are the finite numbers of circumferential and radial modes, respectively, that can be represented accurately on the computational grid used to determine the near-field solution.

Once the wave-type far-field disturbances are determined, they are combined with any convected disturbance to obtain the complete far-field disturbance. At the upstream far-field boundary, the complex amplitude of the convected disturbance is set to describe any incident convected gust. At the downstream far-field boundary, the complex amplitude of the convected disturbance is set to be the difference between the total unsteady disturbance and the sum of the wave-type disturbances.

Thus, at the downstream boundary, the acoustic and nearly-convected unsteady disturbances in (4.26) are subtracted from the total unsteady disturbance, $\mathbf{u}$, and the remainder, $\mathbf{u}_C(r,\theta,\xi_+) = \mathbf{u}(r,\theta,\xi_+) - \mathbf{u}_W(r,\theta,\xi_+)$, is regarded as a convected disturbance. This has the effect of lumping all of the convected disturbances together, and relies on having a complete, orthogonal basis set for the wave-type disturbances. Thus, any error in the represention of the wave-type disturbances will appear in the assumed convected modes. The convected disturbance in the far-downstream region is computed by the method of characteristics as a solution of the equation $\bar{D}\tilde{\mathbf{u}}_C/Dt \equiv 0$. Because the mean radial velocity is assumed to be negligible, mean streamlines will lie along constant radius surfaces. Along one of these constant radius streamlines, $r\theta V_\xi - V_\theta \xi =$ constant, and the functional form of the far-downstream convected field is $\mathbf{u}_C(r,\theta,\xi) = \mathbf{u}_C(r,\theta,\xi_+)\exp\left[-i\omega\left(\xi-\xi_+\right)/V_\xi\right]$.

In the near field, the linearized unsteady governing equations are solved using the iterative technique described in the next section of this report. After each iterative update of the near-field solution, the amplitudes of the wave-type modes, i.e., $a^{\mp}_{m\mu,A}$ and $a^{\mp}_{m\mu,N}$, and the far-downstream convected disturbance, $\mathbf{u}_C(r,\theta,\xi_+)$, are updated. The far-field solutions, which are the sums of wave-type and convected disturbances, are then updated, and these values are used to supply the far-field boundary information needed for the next near-field update.

5. Numerical Model for the Linearized Unsteady Equations

The field equations that govern the nonlinear steady and the first-harmonic, linearized, unsteady flows through a vibrating blade row rotating at constant angular velocity $\mathbf{\Omega}$ have been given, as equations (3.13) and (3.16), respectively. The unsteady equation has been written in a conservation form in which the terms that depend explicitly on the blade motion, i.e., on $\mathbf{R}$, are regarded as known source terms. As described previously, the steady and linearized unsteady field equations must be solved, in sequence, each subject to appropriate boundary conditions at the blade surfaces, the duct walls, the blade-to-blade periodic boundaries, and at the inflow and outflow boundaries of the computational domain.

We proceed to describe the numerical procedures developed to resolve the linearized, first-harmonic, unsteady flow. These procedures are based on those used in the nonlinear unsteady analysis, TURBO, and have been implemented into the LINFLUX unsteady flow code. TURBO is an implicit, flux-split, cell-centered, finite-volume analysis that can be used to predict three-dimensional, nonlinear, inviscid and viscous, steady and unsteady flows. A detailed description of this analysis can be found in [JHW92]. Also, an excellent description of the basic numerical methods underlying TURBO and a two-dimensional counterpart, called NPHASE, can be found in [SLH+94].

In addition to serving as a basis for the development of the LINFLUX code, the TURBO analysis is used in the present study to provide the steady background flow information needed for a linearized, inviscid, unsteady aerodynamic analysis. In principle, LINFLUX can be run with any steady Euler solution. In practice, however, all codes have different error behaviors on finite grids. The TURBO and LINFLUX error behaviors should be similar, since these codes use similar numerical representations for the field equations and boundary conditions. So, in this sense a grid that works well for TURBO will work well for LINFLUX, and vice versa. This may not be true for other mean flow analyses.

The computational mesh used in the TURBO and LINFLUX analyses is a sheared H-mesh, typically generated using either the IGB [BH92] or the TIGER [SS91] grid-generation packages. This structured mesh defines a curvilinear coordinate system, the boundaries of which lie along the boundaries of the physical domain, such that there is a one-to-one correspondence between the points, $\bar{\mathbf{x}}$, in the physical domain and the points, $\boldsymbol{\alpha}$, in a rectangular computational domain, where the grid is uniform and orthogonal. The mesh points in physical space define the eight vertices of the non-overlapping hexahedral cells that fill the solution domain. For the sheared H-mesh, the α_1, α_2 and α_3 computational coordinates, or the I, J, K computational mesh indices, refer to the axial, radial and the blade-to-blade or circumferential directions, respectively. Cell faces are surfaces of constant computational coordinate, so that each cell is bounded by the six surfaces, defined by $\alpha_1 = I - 1/2$ and $I + 1/2$, and $\alpha_2 = J - 1/2$ and $J + 1/2$, and $\alpha_3 = K - 1/2$ and $K + 1/2$. The connectivity of the cells is thus known from the computational coordinates, with neighboring cells given by changing a computational coordinate by one.

5.1 Finite Volume Equations

Let the symbol $\hat{}$ refer to a quantity expressed in terms of cell parameters. Then, a finite-volume spatial discretization of the pseudo time dependent form of the linearized unsteady

equation (3.16a) can be written in the form

$$\frac{\partial \hat{\mathbf{u}}}{\partial \tau} = -i\omega\hat{\mathbf{u}} - \delta_j \hat{\mathbf{f}}_j + \frac{\partial \mathbf{S}}{\partial \mathbf{U}}\hat{\mathbf{u}} - i\omega(\Delta\vartheta)\mathbf{U} - \delta_j \hat{\mathbf{f}}_j^d + (\Delta\vartheta)\mathbf{S} + \bar{\vartheta}(\mathbf{R}\cdot\nabla_{\bar{\mathbf{x}}})\mathbf{S} = -\hat{\mathbf{r}} \tag{5.1}$$

where

$$\hat{\mathbf{u}} = \bar{\vartheta}\mathbf{u}\ , \quad \hat{\mathbf{f}}_j = \frac{\partial \hat{\mathbf{F}}_j}{\partial \mathbf{U}}\mathbf{u} = \bar{A}_{jk}\frac{\partial \mathbf{F}_k}{\partial \mathbf{U}}\mathbf{u} = \bar{A}_{jk}\mathbf{f}_k\ , \quad \text{and} \quad \hat{\mathbf{f}}_j^d = -\dot{\vartheta}_j\mathbf{U} + a_{jk}\mathbf{F}_k\ . \tag{5.2}$$

In equations (5.1) and (5.2), $\mathbf{u}$, $\mathbf{U}$, and $\mathbf{S}$ represent average values of the physical state and source term vectors over a mean cell volume; $\partial/\partial\tau$ is the pseudo time derivative; $\bar{\vartheta}$ is the mean cell volume; $\bar{A}_{jk}$ is the mean area of the constant α_j cell face projected in the $\bar{x}_k$ direction; the vectors $\hat{\mathbf{f}}_j$ and $\hat{\mathbf{F}}_j$ are the unsteady and steady fluxes, respectively, across a constant α_j cell face; $\hat{\mathbf{f}}_j^d$ is the unsteady flux, across the constant α_j face, that is associated with the deformation field, $\mathbf{R}$; and $\hat{\mathbf{r}}$ is the residual of the first-harmonic unsteady equation. The steady quantities $\bar{\vartheta}$, $\bar{A}_{jk}$, $\mathbf{U}$, $\mathbf{F}_j(\mathbf{U})$ and $\mathbf{S}(\mathbf{U},\bar{\mathbf{x}})$ are regarded as known for the linearized unsteady analysis.

The operator δ_j in (5.1) denotes the difference in the j-direction across adjacent cell interfaces, e.g., $\delta_j(\ \ )|_{I,J,K} = (\ \ )_{I,J+1/2,K} - (\ \ )_{I,J-1/2,K}$, where I, J and K are cell indices, and the $J\pm 1/2$ are the indices of the cell faces that are perpendicular to the α_j-direction. The repeated j index in (5.1) implies summation over all computational coordinate directions, so that the term

$$\begin{aligned}\delta_j \hat{\mathbf{f}}_j\big|_{I,J,K} = \hat{\mathbf{f}}_1\big|_{I+1/2,J,K} - \hat{\mathbf{f}}_1\big|_{I-1/2,J,K} + \hat{\mathbf{f}}_2\big|_{I,J+1/2,K} - \hat{\mathbf{f}}_2\big|_{I,J-1/2,K} \\ + \hat{\mathbf{f}}_3\big|_{I,J,K+1/2} - \hat{\mathbf{f}}_3\big|_{I,J,K-1/2}\end{aligned} \tag{5.3}$$

is the net unsteady flux through a cell due to the unsteady fluid motion, and $\delta_j\hat{\mathbf{f}}_j^d$ is the net unsteady flux due to grid motion.

The linearized perturbation equation contains source terms that arise because this equation has been expressed in terms of the reference spatial coordinates, $\bar{\mathbf{x}}$. The source terms depend on known steady flow properties and on the prescribed displacement field, $\mathbf{R}(\bar{\mathbf{x}})$. They are associated with changes in cell volume, cell face area, and cell radial location. The volume source term is given by $-i\omega(\Delta\vartheta)\mathbf{U} + (\Delta\vartheta)\mathbf{S}$, where $\Delta\vartheta = \delta_j(\bar{A}_{jk}R_{x_k})$ is the complex amplitude of the first-harmonic perturbation in the cell volume. The cell face source term, $-\delta_j\hat{\mathbf{f}}_j^d$, accounts for the net mean flux through the moving cell faces. The complex amplitudes of the first-harmonic perturbations in the projected face areas, a_{jk}, are computed using first order expansions in $\mathbf{R}$ for the area of a cell face, and the swept volume is given by $\dot{\vartheta}_j = i\omega\bar{A}_{jk}R_{x_k}$. In evaluating $\Delta\vartheta$ and $\dot{\vartheta}_j$, the R_{x_k} are taken to be the average displacements over a cell face. The remaining grid deformation source term, $\bar{\vartheta}(\mathbf{R}\cdot\boldsymbol{\nabla}_{\bar{\mathbf{x}}})\mathbf{S}$, where $\mathbf{R}$ is based on the average displacement of the cell vertices, accounts for changes in cell radial location.

The field equation (5.1) must be solved subject to the conditions imposed at the boundaries of the computational domain. Flow tangency conditions, cf. (3.17), are applied at the blade surfaces and the duct walls, a phase-lagged, periodicity condition, cf. (3.15), is applied at the blade-to-blade periodic boundaries, and analytic/numeric far-field eigensolutions are

matched to the numerical near-field solution at the inflow and outflow boundaries of the computational domain.

The flow tangency conditions are implemented by using phantom cells inside a solid surface. The density and pressure in a phantom cell are defined using a reflection condition, i.e., the phantom cell values, ρ_{ph} and p_{ph}, are set equal to the interior values, ρ_{int} and p_{int} at the adjacent cells within the fluid. This reflection condition is first-order accurate because the effects of surface curvature on the pressure are neglected. To obtain higher order accuracy, a pressure extrapolation or a solution to the normal momentum equation would be required. The phantom cell velocity is calculated such that the velocity at the solid surface, which is the average of the velocities in the phantom and the interior cells, satisfies the flow tangency condition, in a manner consistent with the finite volume discretization. Thus, the phantom-cell velocity is given by

$$\mathbf{v}_{ph} = \mathbf{v}_{\text{int}} + 2\left(-\mathbf{v}_{\text{int}} \cdot \bar{\mathbf{n}} + i\omega \mathbf{R} \cdot \bar{\mathbf{n}} + \mathbf{V} \cdot [\Delta(\bar{\mathbf{n}} d\bar{A})]/\bar{A}\right) \bar{\mathbf{n}} + 2\mathbf{V} \cdot \bar{\mathbf{n}}[\Delta(\bar{\mathbf{n}} d\bar{A})]/\bar{A} \qquad (5.4)$$

where $\Delta(\bar{\mathbf{n}} d\bar{A})$, cf. (3.11), accounts for the changes in the normal direction and area of the cell-face that coincides with the solid surface.

In imposing the periodicity condition, we take advantage of the grid periodicity in the blade-to-blade direction to define the state vector in the cells that lie along a periodic boundary. Thus, if NK denotes the number of blade-to-blade grid points, then the number of blade-to-blade grid cells is $NK - 1$, and the periodicity condition can be written as

$$\mathbf{u}|_{I,J,K} = \mathbf{T}_{\pm 1} \mathbf{u}_{I,J,K \pm (NK-1)} \exp(\pm i\sigma) \ . \qquad (5.5)$$

where I, J and K are cell indices, and the $\mathbf{T}_n$ matrix rotates the x_2 and x_3 components of the momentum vector through n blade passages.

The far-field conditions allow for the prescription of external aerodynamic disturbances and permit unsteady disturbance waves coming from within the solution domain to pass through the inflow and outflow boundaries without reflection. The far-field solutions currently used in LINFLUX have been described in §4 of this report. It should be noted that the far-field conditions used in TURBO are based on one-dimensional characteristic theory. This should lead to no loss in the accuracy of nonlinear steady solutions, provided that the computational inflow and outflow boundaries are placed far enough from the blade row so that outgoing steady disturbances have decayed to negligible levels.

Pseudo-Time Marching Procedure

A pseudo-time marching technique is used to converge successive estimates for the complex amplitudes of the unsteady conservation variables to constant or "steady-state" values. For this purpose, the pseudo time derivative in (5.1) is approximated using a first-order accurate, two-point, backward, difference approximation. In particular, we set

$$\hat{\Theta} \Delta \mathbf{u}^n = -\hat{\mathbf{r}}^{n+1} \ , \qquad (5.6)$$

where the superscript n refers to the current or nth pseudo time level, $\hat{\Theta} = \bar{\vartheta}/\Delta\tau$, and $\Delta \mathbf{u}^n = \mathbf{u}^{n+1} - \mathbf{u}^n$ is a pseudo-time update to the state vector. Equation (5.6) is used to

predict the state vector $\mathbf{u}^{n+1}$ at the $(n+1)$th pseudo time step in terms of the state vector at the previous time step and the unsteady residual, $\hat{\mathbf{r}}$, at the $(n+1)$th time step. The norm $||\Delta\mathbf{u}^n||$ is expected to approach zero with increasing n.

After expanding the residual, $\hat{\mathbf{r}}^{n+1}$, about the nth time level, we can write the discretized unsteady field equation as

$$\left(\hat{\Theta}\mathbf{I} + \frac{\partial\hat{\mathbf{r}}}{\partial\mathbf{u}}\right)\Delta\mathbf{u}^n = -\hat{\mathbf{r}}^n \ , \tag{5.7}$$

where $\hat{\mathbf{r}}$ is defined in (5.1) and $\partial\hat{\mathbf{r}}/\partial\mathbf{u}$ is a constant, since the unsteady residual is a linear function of the state vector $\mathbf{u}$. The change in the residual at the nth time step due to the pseudo-time update is given by

$$\frac{\partial\hat{\mathbf{r}}}{\partial\mathbf{u}}\Delta\mathbf{u}^n = i\omega\bar{\vartheta}\Delta\mathbf{u}^n + \delta_j\left(\frac{\partial\hat{\mathbf{F}}_j}{\partial\mathbf{U}}\Delta\mathbf{u}^n\right) - \bar{\vartheta}\frac{\partial\mathbf{S}}{\partial\mathbf{U}}\Delta\mathbf{u}^n \ , \tag{5.8}$$

and it follows from (5.1), (5.7) and (5.8), that the pseudo-time update formula can be expressed in the form

$$\left(\hat{\Theta} + i\omega\bar{\vartheta} - \bar{\vartheta}\frac{\partial\mathbf{S}}{\partial\mathbf{U}}\right)\Delta\mathbf{u}^n + \delta_j\left(\frac{\partial\hat{\mathbf{F}}_j}{\partial\mathbf{U}}\Delta\mathbf{u}^n\right) = -\bar{\vartheta}\left(i\omega - \frac{\partial\mathbf{S}}{\partial\mathbf{U}}\right)\mathbf{u}^n - (\delta_j\hat{\mathbf{f}}_j)^n + \mathbf{s}^n = -\hat{\mathbf{r}}^n \ , \tag{5.9}$$

where $\mathbf{s}$ is the grid deformation source term.

5.2 Evaluation of Flux Terms

In this and the following subsections we will describe the spatial discretizations that are used to approximate the flux terms on the left- and right-hand sides of equation (5.9) and the pseudo-time integration used to solve this equation. To simplify these descriptions, we will consider a "one-dimensional flow" in which $\hat{\mathbf{F}}_j = \hat{\mathbf{F}}$ and $\hat{\mathbf{f}}_j = \hat{\mathbf{f}}$ are the steady and unsteady flux vectors in the $\alpha_j = \alpha$ computational coordinate direction. The subscript J will refer to the cell volume bounded by the cell surfaces at $\alpha = J+1/2$ and $\alpha = J-1/2$. The extensions of the equations that follow to three-dimensional flows is straightforward conceptually, but involves the use of tedious additional nomenclature.

Interfacial Fluxes

A cell-centered finite-volume discretization requires that the fluxes at cell surfaces be computed in terms of the values of the state vector in the neighboring cell volumes. In the TURBO and LINFLUX analyses, a flux splitting technique is applied in which the flux at a cell interface is computed in terms of a flux Jacobian matrix representing the local interface conditions and the values of the state vector in the cell volumes adjacent to the interface. The eigenvalues of the flux Jacobian matrix are used to determine which characteristic modes are taken into account, thus controlling the direction of spatial differencing.

The flux splitting is based on a similarity transformation and an eigenvalue decomposition of the flux Jacobian matrix, $\partial\hat{\mathbf{F}}/\partial\mathbf{U}$, into matrices that account for right (+) and left (−) traveling disturbances. Thus, the flux vector, $\hat{\mathbf{f}}$, is split according to

$$\hat{\mathbf{f}} = \frac{\partial\hat{\mathbf{F}}}{\partial\mathbf{U}}\mathbf{u} = \left(\frac{\partial\hat{\mathbf{F}}}{\partial\mathbf{U}}^{+} + \frac{\partial\hat{\mathbf{F}}}{\partial\mathbf{U}}^{-}\right)\mathbf{u} = \hat{\mathbf{T}}(\hat{\mathbf{\Lambda}}^{+} + \hat{\mathbf{\Lambda}}^{-})\hat{\mathbf{T}}^{-1}\mathbf{u} \ , \tag{5.10}$$

where the (+) terms are determined using information from the negative coordinate direction; the (−) terms, using information from the positive coordinate direction. The matrices $\hat{\mathbf{T}}$ and $\hat{\mathbf{T}}^{-1}$ contain the right and left eigenvectors, respectively, of $\partial\hat{\mathbf{F}}/\partial\hat{\mathbf{U}}$, and $\hat{\mathbf{\Lambda}}^{+}$ and $\hat{\mathbf{\Lambda}}^{-}$ are diagonal matrices containing the positive (+) and negative (−) eigenvalues, respectively. Thus, the sign of the wave speed (i.e., + or −) determines the direction in which spatial differencing is applied.

In the TURBO analysis, two methods are applied to evaluate surface fluxes. One is the flux vector splitting scheme proposed by Steger and Warming [SW81]; the other, the flux difference splitting scheme proposed by Roe [Roe81]. The former is applied to evaluate the left-hand-side flux terms, i.e., the flux terms appearing in the implicit operator; the latter, to evaluate those on the right-hand side. Flux vector splitting is used in the nonlinear analysis, because the resulting flux Jacobians are easier to compute than those resulting from flux difference splitting, and these Jacobians must be computed at each time step. In LINFLUX, however, flux difference splitting is used to evaluate the flux terms on both sides of the linear unsteady equation. This is feasable because the steady flux Jacobian matrices must only be computed once, and it has been found to improve the convergence rates of the linear unsteady solutions. The use of an inconsistent flux splitting in TURBO should only affect convergence rates, but not the final converged solutions.

In the flux difference splitting approach, the flux, $\hat{\mathbf{f}}_{J+1/2}$, at the $J+1/2$ cell interface is constructed from the flux in the cell to the left (J) or right ($J+1$) of the interface plus the flux due to waves approaching the interface due to the change in the state vector across the interface. In the present implementation, we have chosen to evaluate the flux vector, $\hat{\mathbf{f}}_{J+1/2}$, based on $\hat{\mathbf{f}}(\mathbf{u}_J)$, and disturbances traveling to the left, i.e., at negative wave velocity. This results an approximate expression for the unsteady flux at the $J+1/2$ interface of the form

$$\hat{\mathbf{f}}_{J+1/2} = \left(\frac{\partial\hat{\mathbf{F}}}{\partial\mathbf{U}}\mathbf{u}\right)_{J+1/2} \approx \hat{\mathbf{f}}(\mathbf{u}_J, \bar{A}_{J+1/2}) + \left.\frac{\partial\hat{\mathbf{F}}}{\partial\mathbf{U}}\right|^{-}_{\mathbf{U}^{\mathrm{Roe}}_{J+1/2},\bar{A}_{J+1/2}} (\mathbf{u}_{J+1} - \mathbf{u}_J) \ . \tag{5.11}$$

In equation (5.11), $\hat{\mathbf{f}}(\mathbf{u}_J, \bar{A}_{J+1/2})$ is a flux based on the state vector in the Jth cell and the area of the $J+1/2$ cell interface, and the flux Jacobian matrix $\partial\hat{\mathbf{F}}/\partial\mathbf{U}|_{\mathbf{U}^{\mathrm{Roe}}_{J+1/2},\bar{A}_{J+1/2}}$ is evaluated in terms of the intermediate state vector, $\mathbf{U}^{\mathrm{Roe}}_{J+1/2}$, and the area $\bar{A}_{J+1/2}$. The intermediate state vector, $\mathbf{U}^{\mathrm{Roe}}_{J+1/2}$, is based on $\mathbf{U}_J$ and $\mathbf{U}_{J+1}$ and is defined according to the relations:

$$\bar{\rho}^{\mathrm{Roe}}_{J+1/2} = \sqrt{\bar{\rho}_J\bar{\rho}_{J+1}} \ , \quad \mathbf{V}^{\mathrm{Roe}}_{J+1/2} = \frac{\sqrt{\bar{\rho}_J}\mathbf{V}_J + \sqrt{\bar{\rho}_{J+1}}\mathbf{V}_{J+1}}{\sqrt{\bar{\rho}_J} + \sqrt{\bar{\rho}_{J+1}}} \ ,$$

and

$$E^{\mathrm{Roe}}_{T,J+1/2} = \frac{\sqrt{\bar{\rho}_J}E_{T,J} + \sqrt{\bar{\rho}_{J+1}}E_{T,J+1}}{\sqrt{\bar{\rho}_J} + \sqrt{\bar{\rho}_{J+1}}} \ . \tag{5.12}$$

The flux, $\hat{\mathbf{f}}_{J+1/2}$, in (5.11) could also have been constructed from $\hat{\mathbf{f}}(\mathbf{u}_{J+1}, \bar{A}_{J+1/2})$ and the disturbances traveling at positive wave velocity, or from an average value of the flux vectors in the neighboring cells and an average of the disturbances traveling at positive and negative wave velocities.

The discrete approximation (5.11) is first-order accurate, since the interfacial fluxes are based only upon information from adjacent cells. Higher order spatial accuracy can be

achieved by adding corrective fluxes, which bring in information from additional neighboring cells. In TURBO, flux limiters are used in conjunction with the corrective fluxes to control the dispersive errors that occur near shocks and stagnation points, but such limiters have not yet been incorporated into the LINFLUX analysis.

In LINFLUX, the corrective perturbation flux at the $J+1/2$ interface is comprised of right traveling waves at the upstream interface $(J-1/2)$ of the adjacent upstream cell (J) and left traveling waves at the downstream interface $(J+3/2)$ of the adjacent downstream cell $(J+1)$. These waves are approximated using the Roe-averaged flux Jacobian matrix at the $J+1/2$ interface. Thus, the enhanced approximation to the perturbation flux is given by

$$\begin{aligned} \hat{\mathbf{f}}_{J+1/2} \;\approx\; & \hat{\mathbf{f}}(\mathbf{u}_J, \bar{A}_{J+1/2}) + \left.\frac{\partial \hat{\mathbf{F}}}{\partial \mathbf{U}}\right|^{-}_{\mathbf{U}^{\mathrm{Roe}}_{J+1/2}, \bar{A}_{J+1/2}} (\mathbf{u}_{J+1} - \mathbf{u}_J) \\ & + \frac{1}{2}\left[\left.\frac{\partial \hat{\mathbf{F}}}{\partial \mathbf{U}}\right|^{+}_{\mathbf{U}^{\mathrm{Roe}}_{J+1/2}, \bar{A}_{J+1/2}} (\mathbf{u}_J - \mathbf{u}_{J-1}) - \left.\frac{\partial \hat{\mathbf{F}}}{\partial \mathbf{U}}\right|^{-}_{\mathbf{U}^{\mathrm{Roe}}_{J+1/2}, \bar{A}_{J+1/2}} (\mathbf{u}_{J+2} - \mathbf{u}_{J+1}) \right] , \end{aligned} \tag{5.13}$$

and should result in second order spatial accuracy.

Right- and Left-Hand-Side Flux Terms

Once the interfacial fluxes have been computed, they are spatially differenced to compute the flux terms that appear on the right- and left-hand sides of the unsteady equation (5.9). The difference expression for the net unsteady flux through the Jth control volume is

$$\delta \hat{\mathbf{f}}\Big|_J \approx \hat{\mathbf{f}}_{J+1/2} - \hat{\mathbf{f}}_{J-1/2} \; , \tag{5.14}$$

and the second-order discrete approximation, cf. (5.13), is used in conjunction with (5.14) to evaluate the net unsteady flux term that appears on the right-hand side of (5.9).

The left-hand side flux term in (5.9) represents the change in the net unsteady flux due to the pseudo time update. It is evaluated using the first-order accurate flux difference splitting approximation in (5.11), i.e., we set

$$\begin{aligned} \delta\left(\frac{\partial \hat{\mathbf{F}}}{\partial \mathbf{U}}\Delta\mathbf{u}\right)\Big|_J \;\approx\; & \hat{\mathbf{f}}(\Delta\mathbf{u}_J, \bar{A}_{J+1/2}) + \left.\frac{\partial \hat{\mathbf{F}}}{\partial \mathbf{U}}\right|^{-}_{\mathbf{U}^{\mathrm{Roe}}_{J+1/2}, \bar{A}_{J+1/2}} (\Delta\mathbf{u}_{J+1} - \Delta\mathbf{u}_J) \\ & - \hat{\mathbf{f}}(\Delta\mathbf{u}_{J-1}, \bar{A}_{J-1/2}) - \left.\frac{\partial \hat{\mathbf{F}}}{\partial \mathbf{U}}\right|^{-}_{\mathbf{U}^{\mathrm{Roe}}_{J-1/2}, \bar{A}_{J-1/2}} (\Delta\mathbf{u}_J - \Delta\mathbf{u}_{J-1}) \; , \end{aligned} \tag{5.15}$$

where $\hat{\mathbf{f}}(\Delta\mathbf{u}_J, \bar{A}_{J+1/2}) = \partial\mathbf{F}/\partial\mathbf{U}|_{\mathbf{U}=\mathbf{U}_J} \bar{A}_{J+1/2}\Delta\mathbf{u}_J = (\partial\hat{\mathbf{F}}/\partial\mathbf{U})_{\mathbf{U}_J, \bar{A}_{J+1/2}}\Delta\mathbf{u}_J$.

5.3 Pseudo-Time Integration

The linearized unsteady equation (5.9) is discretized, as outlined above, leading to a system of linear algebraic equations. In the discretization, the flux terms appearing on the left- and right-hand-sides of equation (5.9) are computed using flux difference splitting and the approximations to the flux terms on the right-hand-side are corrected for higher order spatial accuracy. The resulting system of algebraic equations is solved at each pseudo-time step using an iteration procedure in which the left-hand side matrix is decomposed into diagonal and off-diagonal, positive and negative, submatrices. Symmetric Gauss-Seidel (SGS) iterations [WT91] are then applied to solve the decomposed, discretized, pseudo time-stepping equation.

In particular, the pseudo-time stepping equation can be expressed in the form

$$\left(\hat{\Theta}_J \mathbf{I} + \left.\frac{\partial \hat{\mathbf{r}}}{\partial \mathbf{u}}\right|_{\mathbf{u}_J^n}\right) \Delta \mathbf{u}_J^n = \mathbf{D}_J \Delta \mathbf{u}_J^n - \mathbf{M}_{J-1}^{+} \Delta \mathbf{u}_{J-1}^n + \mathbf{M}_{J+1}^{-} \Delta \mathbf{u}_{J+1}^n = -\hat{\mathbf{r}}_J^n \ , \tag{5.16}$$

where the $\mathbf{D}$ submatrix contains the diagonal elements of the original matrix, and the $\mathbf{M}^{+}$ and $\mathbf{M}^{-}$ submatrices contain the off-diagonal elements in the negative and positive computational coordinate directions, respectively. Based on the flux difference splitting scheme given in (5.15), these matrices are given by

$$\mathbf{D}_J = (\hat{\Theta}_J + i\omega\bar{\vartheta}_J)\mathbf{I} - \bar{\vartheta}_J \left.\frac{\partial \mathbf{S}}{\partial \mathbf{U}}\right|_{\mathbf{U}_J} + \left.\frac{\partial \hat{\mathbf{F}}}{\partial \mathbf{U}}\right|_{\mathbf{U}_J, \bar{A}_{J+1/2}} - \left.\frac{\partial \hat{\mathbf{F}}}{\partial \mathbf{U}}\right|^{-}_{\mathbf{U}^{\mathrm{Roe}}_{J+1/2}, \bar{A}_{J+1/2}} - \left.\frac{\partial \hat{\mathbf{F}}}{\partial \mathbf{U}}\right|^{-}_{\mathbf{U}^{\mathrm{Roe}}_{J-1/2}, \bar{A}_{J-1/2}}$$

$$\mathbf{M}_{J-1}^{+} = \left.\frac{\partial \hat{\mathbf{F}}}{\partial \mathbf{U}}\right|_{\mathbf{U}_{J-1}, \bar{A}_{J-1/2}} - \left.\frac{\partial \hat{\mathbf{F}}}{\partial \mathbf{U}}\right|^{-}_{\mathbf{U}^{\mathrm{Roe}}_{J-1/2}, \bar{A}_{J-1/2}} \quad \text{and} \quad \mathbf{M}_{J+1}^{-} = \left.\frac{\partial \hat{\mathbf{F}}}{\partial \mathbf{U}}\right|^{-}_{\mathbf{U}^{\mathrm{Roe}}_{J+1/2}, \bar{A}_{J+1/2}} , \tag{5.17}$$

where the J subscript refers to the Jth cell, the $J \pm 1/2$ subscripts refer to the right and left interfaces of this cell, and $J-1$ refers to the adjacent upstream cell.

Introducing l as the Gauss-Seidel iteration index, the iteration formula for the linearized unsteady equation can be written in the form

$$\begin{aligned} \mathbf{D}_J \Delta \mathbf{u}_J^* - \mathbf{M}_{J-1}^{+} \Delta \mathbf{u}_{J-1}^* &= -\mathbf{M}_{J+1}^{-} \Delta \mathbf{u}_{J+1}^{l-1} - \mathbf{r}_J^n \\ \mathbf{D}_J \Delta \mathbf{u}_J^l + \mathbf{M}_{J+1}^{-} \Delta \mathbf{u}_{J+1}^l &= \mathbf{M}_{J-1}^{+} \Delta \mathbf{u}_{J-1}^* - \mathbf{r}_J^n \ , \end{aligned} \tag{5.18}$$

where $l = 1, 2, \ldots, L$, $\mathbf{u}_J^0 = \mathbf{u}_J^n$, $\Delta \mathbf{u}_J^* = \mathbf{u}_J^* - \mathbf{u}_J^n$, $\Delta \mathbf{u}_J^l = \mathbf{u}_J^l - \mathbf{u}_J^n$, and $\mathbf{u}_J^L \approx \mathbf{u}_J^{n+1}$. The first SGS iteration is over negative grid indices and the second iteration is over positive grid indices. The iteration procedure thus involves an LU decomposition of the pseudo-time update matrix, with forward and backward substitution. Once the pseudo-time solutions converge to a steady state, i.e., $||\hat{\mathbf{r}}^n|| \to 0$, any error introduced by the iteration scheme (5.18) vanishes. Only the discretization errors associated with the calculation of the residual of equation (5.1) remain. The current LINFLUX implementation uses explicit boundary conditions, which are incorporated into the LU-SGS iteration procedure, so that the boundary conditions are imposed in a semi-implicit manner. This treatment has been found to yield better convergence properties than a purely explicit implementation.

6. Numerical Results

Unsteady aerodynamic response predictions will be presented to demonstrate the accuracy and current capabilities of the 3D LINFLUX code. We consider three-dimensional unsteady flows through a helical-plate rotor and a real-blade rotor based on the Tenth Standard Cascade Configuration [FV93]. We will refer to the former as a helical fan, and the latter as the 3D 10th Standard Cascade. In each case, the rotor consists of 24 blades and operates within a cylindrical annular duct of inner radius $r_H = 3.395$ and outer radius $r_D = 4.244$. Therefore, the circumferential blade spacing, $G(r) = 2\pi r/N_{\rm B}$, at midspan, $r = 0.9r_D$, is unity. We assume that there is no clearance between the rotor blades and the outer duct wall. Also, in each case, the steady background flow at inlet is axial and uniform relative to a space-fixed or inertial reference frame. Thus, the inlet Mach number, $M^{\rm abs}_{-\infty} = M^{\rm abs}_{\xi,-\infty} = M_{\xi,-\infty}$ is a constant.

We will consider unsteady flows that are excited by prescribed single-degree-of-freedom, harmonic, blade motions (e.g., see Figure 2), or by acoustic excitations at inlet or exit. The blade vibrations occur at unit frequency ($\omega = 1$) and with a constant phase angle, $\sigma = 2\pi N_{\rm D}/N_{\rm B}$, between the motions of adjacent blades. The blade motions to be considered are pure translations normal to the sectional blade chords (bending) and pure rotations about axes at the blade midchords (torsion). These motions [cf. (2.1)] are defined by $\mathbf{R}_{\rm B} = h\mathbf{n}$ and $\mathbf{R}_{\rm B}(\bar{\mathbf{x}}_{\rm B}) = \boldsymbol{\alpha} \times (\bar{\mathbf{x}}_{\rm B} - \bar{\mathbf{x}}_{\rm P})$, respectively, where h and α are the complex amplitudes of the bending and torsional vibrations; $\mathbf{n}(r) = n_\theta \mathbf{e}_\theta + n_\xi \mathbf{e}_\xi$ is the unit normal to the blade chord at radius r, which is tangent to the cylinder $r =$ constant; and $\bar{\mathbf{x}}_{\rm B} - \bar{\mathbf{x}}_{\rm P}$ is the distance, at constant radius, to the point, $\bar{\mathbf{x}}_{\rm B}(r)$, on the mean or reference blade surface from the point, $\bar{\mathbf{x}}_{\rm P}(r)$, at the mean position of the torsional axis. To allow convenient comparisons between the LINFLUX predictions and those of two-dimensional unsteady flow codes, we have assumed that the complex amplitudes of the vibratory blade motions are constant along the span.

The linearized analyses have been applied to predict unsteady surface pressure and local (w_C) and global (W_C) work per cycle responses to the prescribed blade vibrations. The local and global works per cycle are determined from the relations

$$w_C(\bar{\mathbf{x}}_{\rm B}) = -\pi Im\{(P_{\rm B}\Delta(\bar{\mathbf{n}}_{\rm B}d\bar{A}_{\rm B})/\, d\bar{A}_{\rm B} + p_{\mathcal{B}}\bar{\mathbf{n}}_{\rm B}) \cdot \mathbf{R}^*_{\rm B}\} \quad \text{and} \quad W_C = \int_{\bar{A}_{\rm B}} \omega_C(\bar{\mathbf{x}}) d\bar{A}_{\rm B} \ . \quad (6.1)$$

In equation (6.1), $Im\{\ \ \}$ denotes the imaginary part of $\{\ \ \}$; P is the steady pressure; p is the complex amplitude of the unsteady pressure; the subscripts $\mathcal{B}$ and B refer to the instantaneous and the mean blade surfaces, respectively; $\mathbf{n}$ is a unit normal vector pointing out from the blade surface; $d\bar{A}$ is a differential element of surface area; $\Delta(\bar{\mathbf{n}}_{\rm B}d\bar{A}_{\rm B})$ is the complex amplitude of the first harmonic component of $\mathbf{n}_{\mathcal{B}}d\mathcal{A}_{\mathcal{B}} - \bar{\mathbf{n}}_{\rm B}d\bar{A}_{\rm B}$, cf. (3.11); and the superscript $*$ denotes the complex conjugate.

In addition to the unsteady flows excited by prescribed blade motions, we will also consider unsteady flows through the rotor blade rows that are excited by acoustic disturbances at inlet or exit that travel toward the blade row. These excitations are assumed to arise from the aerodynamic coupling between the rotor and an adjacent upstream or downstream stator, consisting of N_V equally spaced blades or vanes. In particular, we will consider acoustic

excitations to the rotor at the vane passing frequency $\omega = -N_V\Omega$ and at interblade phase angle $\sigma = 2\pi N_D/N_B = 2\pi(N_B - N_V)/N_B$.

Numerical results for the unsteady pressure responses in the field and at the blade surfaces will be presented for acoustic excitations at $N_D = N_B - N_V$ nodal diameters ($m = 0$) and zero radial crossings ($\mu = 0$). The state vector for such acoustic excitations has the form, cf. (4.22),

$$\mathbf{u}_A^{\mp}(r,\theta,\xi) = a_A^{\mp}\mathbf{u}_A^{R,\mp}(r)\exp(\chi^{\mp}\xi + iN_D\theta) \ , \quad \xi \lesseqgtr \xi_{\mp} \ . \tag{6.2}$$

where $\chi^{\mp}$ and $\mathbf{u}_A^{R,\mp}(r)$ are solutions of the far-field eigenvalue problem. The constant $a_A^{\mp}$ in (6.2) is chosen so that the complex amplitude of the pressure associated with the acoustic excitation, i.e.,

$$p_A^{\mp}(r,\theta,\xi) = a_A^{\mp}p^{R,\mp}(r)\exp(\chi^{\mp}\xi + iN_D\theta) \ , \quad \xi \lesseqgtr \xi_{\mp} \tag{6.3}$$

has a maximum magnitude of one, at say $r = r_{max}$, on the radial line passing through the leading edge of the reference-blade chord at midspan, and so that $p_A^{\mp} = p_{A,Ref}^{\mp} = (1,0)$ is a real quantity at $r = r_{max}$, see, e.g., Figures 6 and 26.

In addition to the LINFLUX results, for purposes of comparison, we will also present response predictions based on the two-dimensional classical analysis of Smith [Smi72] and on the two-dimensional LINFLO analysis [Ver93]. The Smith analysis applies to flat-plate cascades, staggered so that the blade mean positions are aligned with a uniform relative steady background flow. The unsteady flow is regarded as a small perturbation of this uniform stream. In LINFLO, which applies to more realistic two-dimensional configurations, the unsteady flow is regarded as a small perturbation of a nonuniform, potential, steady background flow. The TURBO [JHW92] analysis has been used to provide the steady background flow information for the LINFLUX linearized unsteady calculations. A utility code was developed to convert the results of the TURBO analysis, which uses a multi-block grid in the absolute frame, into a form usable for the LINFLUX analysis, which uses a single-block grid in the relative frame. The full-potential analysis CASPOF [Cas83] has been used to provide the steady background flows for the LINFLO calculations.

The TURBO nonlinear steady and the LINFLUX linearized unsteady solutions are determined, over a single extended blade passage, on the same H-type grid. The grids used, cf. Figures 3 and 4, for the two geometries considered herein, namely, the helical fan and 3D Tenth Standard Cascade, consist of 141 axial, 41 tangential and 11 radial surfaces (56,000 cells), and extend one axial chord, at mid-span, upstream and downstream from the blade row. This axial extent was found to be sufficient for the mean flow field to reach axisymmetric steady states at the computational inflow and outflow boundaries. Both grids have 81 axial points on the upper and lower blade surfaces, and 30 axial points on the upstream and downstream periodic boundaries. They were found to be sufficient for most of the calculations reported herein, with approximately 20 points per wave being applied to resolve the dominant acoustic waves. For some of the 3D Tenth Standard Cascade calculations, the near-sonic conditions on blade suction surfaces resulted in short wavelength acoustic response phenomena that could not be resolved on the prescribed 141 × 41 × 11 mesh.

In each case, the axial grid distribution has been clustered near blade leading and trailing edges; the circumferential grid distribution, near blade surfaces; and the radial grid distribution is uniform. For the helical fan, the normal and chordwise grid spacings at the leading edge are 0.25% and 0.35% of chord, respectively, see Figure 3. For the 3D Tenth Standard

Cascade, the normal and chordwise grid spacings at the leading edge are 0.02% and 0.10% of chord, respectively, see Figure 4. At present, for real blade calculations, the circumferential grid surfaces must be tightly clustered near the blade surfaces to minimize the numerical losses near the blades that occur in a TURBO steady-flow solution. Such losses can lead to significant errors in a subsequent LINFLUX, linearized unsteady flow solution. For example, a spurious total pressure loss of greater than 1% has been found to distort the LINFLUX predicted surface responses to prescribed blade vibrations.

The LINFLUX near-field, finite-volume solutions have been coupled to far-field acoustic eigensolutions, which have been determined on a radial grid consisting of 24 points clustered near the hub and duct walls. For the present calculations, the artificial dissipation term in (4.17) is set equal to zero and any nearly convected disturbances that occur downstream of the blade row are simply convected numerically through the computational outflow boundary and into the far downstream region of the flow.

The full potential steady and the LINFLO linearized unsteady solutions were determined on composite meshes consisting of local C-meshes embedded in global H-meshes, which extended one axial chord upstream and downstream from the blade row. The H- and C-meshes used with LINFLO consisted of 155 axial and 41 tangential lines and 101 radial and 21 circumferential lines, respectively. Coarser H- and C- meshes were used for the CASPOF calculations.

The 3D numerical solutions reported herein were determined on an IBM-3CT Workstation. The TURBO analysis is currently implemented in the absolute frame of reference, so that "steady" calculations for rotating blade rows must be converged to a time-dependent, steady-state solution, as opposed to a time-independent, steady solution. For a steady-state solution, the time stepping algorithm must be converged at each time step. To achieve a low-loss steady-state solution small time steps ($\approx 200,000$ per wheel revolution) and a relatively large number of subiterations (≈ 10) per time step are required, leading to relatively long CPU times. In particular, the TURBO analysis has required approximately 6 CPU days on the IBM 3CT to reach a converged, low-loss, steady-state solution for the 3D Tenth Standard Cascade. If a rotating frame or steady version of TURBO is constructed the foregoing CPU time should be reduced by an order of magnitude.

The LINFLUX, linearized, unsteady calculations required from 1,000 to 3,500 pseudo-time steps to converge to an 0.1% tolerance for global unsteady aerodynamic response quantities. Using two SGS sub-iterations, approximately 600 time steps could be completed per CPU hour on the IBM 3CT, corresponding to 110 μsec./time-step/cell or 1.5 to 6 CPU hours for a converged unsteady solution. For purposes of comparison, TURBO nonlinear steady and unsteady calculations require approximately 600 μsec./time-step/cell with two sub-iterations and 2600 μsec./time-step/cell with ten sub-iterations. The memory requirements for the two analyses, using 32-bit arithmetic, are approximately 2.2 kilobytes/cell for LINFLUX, and 1.8 kilobytes/cell for TURBO. The TURBO requirement is based on the option of using two blocks per blade passage and in-core storage for all variables. LINFLUX is always applied using a single block and in core storage for all variables. Note that the LINFLUX analysis converges to a pseudo-steady solution in a single blade passage, whereas a TURBO nonlinear unsteady analysis converges to a periodic solution over multiple blade passages. The computer resources required for executing TURBO are thus much greater than those required for executing LINFLUX, especially for nonlinear unsteady calculations

with excitations at nodal diameters that require a large number of blade passages.

6.1 Helical Fan

We consider a helical fan with mean or steady-state blade positions, in the rotating frame, defined by

$$r\theta = \xi \tan\Theta(r) + nG(r) \ , \ 2|\xi| < \cos\Theta(r) \ , \quad n = 0, \ \ldots, \ N_{\mathrm{B}} - 1 \ , \tag{6.4}$$

where $G(r) = 2\pi r/N_{\mathrm{B}}$ is the circumferential blade spacing, and $\Theta(r) = \tan^{-1}(\Omega r/V_\xi)$ is the blade stagger angle. The blade chord, $c(r) = 1$, is taken to be constant along the span; therefore, because of blade twist, the axial chord, $c_{ax}(r) = \cos\Theta(r)$, varies with radius from 0.748 at the hub to 0.669 at the tip. Our local surface response predictions for the helical fan are plotted versus $(\xi - \xi_{\mathrm{lem}})/c_{\mathrm{axm}}$, i.e., the ratio of the axial distance from the blade chord leading edge at midspan, $\xi = \xi_{\mathrm{lem}}$, to the axial chord at midspan, c_{axm}.

The helical fan operates in a uniform, axial, absolute, inlet flow, which occurs at $M_{\xi,-\infty} = 0.495$, and rotates at angular speed $|\boldsymbol{\Omega}| = 0.185$. Since the blades are aligned with the inlet relative mean flow velocity, the steady relative velocity is $\mathbf{V} = \mathbf{V}^{\mathrm{abs}}_{-\infty} - \boldsymbol{\Omega} \times \mathbf{r}$ and the steady thermodynamic properties of the fluid are constant throughout the entire fluid domain. Hence, there are no steady loads acting on the blades, and the inlet $(-\infty)$ and exit $(+\infty)$ freestream conditions are identical.

The foregoing helical-fan geometry and operating condition were chosen to provide a relatively simple 3D test case and to allow meaningful comparisons between the three-dimensional LINFLUX predictions at blade midspan and those of earlier two-dimensional analyses. The two-dimensional results apply to a flat plate cascade, with $G = 1$ and $\Theta = 45\,\mathrm{deg}$, operating in a uniform relative inlet flow at $M_{-\infty} = 0.7$ and $\Omega_{-\infty} = 45\,\mathrm{deg}$, where $\Omega_{-\infty}$ is the inlet flow angle.

Blade Vibrations

The 3D LINFLUX and the 2D Smith analyses have been applied to predict the unsteady aerodynamic responses of the helical fan with blades undergoing either pure torsional vibrations about midchord or pure bending vibrations. These motions occur at unit reduced frequency, $\omega = 1$, and at nodal diameters of $N_D = -6, -5, \ldots, 18$, i.e., at interblade phase angles, $\sigma = 2\pi N_D/N_B$, extending from $-90\,\mathrm{deg}$ to 270 deg in increments of 15 deg.

The predicted axial eigenvalues, $\chi = \beta + i\kappa_\xi$, and radial pressure eigenmodes, $p^R(r)$, for three circumferential $(m = -1, 0, 1)$ and three radial $(\mu = 0, 1, 2)$ acoustic modes are shown in Figures 5 and 6, respectively, for the helical fan subjected to unsteady excitations at $\omega = 1$ and $N_D = \mp 6$ $(\sigma = \mp 90\,\mathrm{deg})$. Since the inlet and exit mean flows for the helical fan are identical, the acoustic properties χ and $p^R(r)$ are the same in the upstream and downstream regions of the flow. The far-upstream and far-downstream modal amplitudes will generally differ, however. Moreover, because the absolute mean flow is uniform, the radial shapes of the upstream and downstream traveling pressure disturbances in a given mode are identical, and the phase of each pressure disturbance is independent of radius.

If the excitation is a prescribed blade vibration, only acoustic response disturbances will be present in the far field, i.e., only upstream propagating and decaying acoustic disturbances occur far upstream of the blade row and only downstream propagating and decaying

disturbances occur far downstream. The results in Figure 5 indicate that for $\omega = 1$ and $N_D = -6$ all acoustic response modes are cut off, i.e., they all attenuate. In this case we refer to the blade motion as being subresonant [Ver89b]. The $(m, \mu) = (0, 0)$ disturbances are the least damped with $|\beta| = 1.806$. For $\omega = 1$ and $N_D = 6$, the disturbances in the $(0, 0)$ mode propagate, with $\kappa_\xi = 1.715$ and $\kappa_\xi = 0.222$ for the upstream and downstream traveling wave, respectively. All other waves attenuate, with the (0,1) disturbances having the least attenuation, i.e., $|\beta| = 4.212$. In this case the blade motion is termed superresonant. The results in Figure 6 indicate that the pressure disturbances in the two $(0, 0)$ modes have little radial variation, whereas the pressures in the higher-order, attenuating modes have significant variation. As noted previously, the higher order modes can be cut on at higher excitation frequencies.

Local (w_C) and global (W_C) work per cycle predictions for the helical fan undergoing pure torsional vibrations about midchord and pure bending vibrations at $\omega = 1$ and $\sigma = -90\,\text{deg}$ and at $\omega = 1$ and $\sigma = 90\,\text{deg}$ are shown in Figure 7. Here, the LINFLUX local response predictions are given at the hub $(r/r_D = 0.8)$, midspan $(r/r_D = 0.9)$, and at the tip $(r/r_D = 1.0)$. The results indicate that, for the excitations considered, the unsteady response at a blade surface does not vary significantly along the span, except perhaps over a segment of the blade surfaces extending from 0 to 20% of blade chord. For the most part, the radial variations in this region are due to the change, with radius, in the axial blade chord. The LINFLUX calculations for both the subresonant $\sigma = -90\,\text{deg}$ and the superresonant $\sigma = 90\,\text{deg}$ blade motions, indicate that the pressure disturbances in the dominant far-field acoustic response mode, i.e., the (0,0) mode, are of small amplitude at the computational inlet and exit boundaries.

Unsteady pressure difference, i.e., $[\![p]\!] = p_{\text{lower}} - p_{\text{upper}}$, predictions, based on the 3D LINFLUX and the 2D Smith analyses, at midspan $(r/r_D = 0.9)$ of the helical fan vibrating in pure torsion and pure bending are shown in Figures 8 and 9, respectively, for blade motions at unit frequency and interblade phase angles, σ, of $-90\,\text{deg}$, $0\,\text{deg}$, $+90\,\text{deg}$ and $+180\,\text{deg}$. The motions at $\sigma = 0\,\text{deg}$ and $\sigma = 90\,\text{deg}$ are superresonant, in each case a single acoustic response disturbance at $(m, \mu) = (0, 0)$ persists far upstream and far downstream of the blade row. The motions at $\sigma = -90\,\text{deg}$ and $\sigma = 180\,\text{deg}$ are subresonant. The LINFLUX and the semi-analytical predictions, given in Figure 8, for the real (in-phase with blade displacement) and imaginary (out-of-phase with blade displacement) components of the unsteady pressure jump, $[\![p]\!]$, across a blade surface are in very good agreement. Small discrepancies occur in the blade leading edge region, which are probably caused by the small radial variations present in the helical fan flows.

Global work per cycle predictions for the blades of the helical fan and those of the corresponding flat-plate cascade undergoing pure torsional vibrations about midchord and pure bending vibrations are shown in Figure 10. In particular, results for the global work per cycle are given versus interblade phase angle for blade vibrations at unit frequency. The 3D LINFLUX results, indicated by the symbols in Figure 10, have been determined for $N_D = -6, -5, \ldots, 18$; the Smith code results, for $-90\,\text{deg} \leq \sigma \leq 270\,\text{deg}$ in increments of one degree. Note that we have multiplied the 2D work per cycle predictions by the blade span $r_D - r_H = 0.2\ r_D = 0.849$ to allow a convenient comparison with the 3D LINFLUX predictions. Also, the vertical lines above the curves in Figure 10 indicate the cut-off or resonance conditions, i.e., $\sigma_{2D}^- = -29.4\,\text{deg}$ and $\sigma_{2D}^+ = 107.3\,\text{deg}$ for the 2D flat-plate cascade

vibrating at $\omega = 1$ and, therefore, approximate resonance conditions at $\omega = 1$ for the helical fan. The flat-plate blade motions at $\sigma_{2D}^- < \sigma < \sigma_{2D}^+$ are superresonant; those at $-90\,\text{deg} \leq \sigma < \sigma_{2D}^-$ or $\sigma_{2D}^+ < \sigma \leq 270\,\text{deg}$ are subresonant. As can be seen from the results in Figure 10, the agreement between the LINFLUX numerical and the Smith semi-analytical predictions is very good over the entire nodal diameter or interblade phase angle range of blade vibration.

Acoustic Excitations

We proceed to consider the unsteady pressure responses of the helical fan to acoustic excitations at $\omega = -N_V\Omega$ and $\sigma = 2\pi(N_B - N_V)/N_B$, resulting from the aerodynamic coupling between the fan and an adjacent upstream or downstream stator consisting of N_V vanes. First, we will consider stators consisting of 18 vanes, and therefore, acoustic excitations at $\omega = 3.332$ and $\sigma = 90\,\text{deg}$ ($N_D = 6$); then, stators consisting of 21 vanes, i.e., acoustic excitations at $\omega = 3.887$ and $\sigma = 45\,\text{deg}$ ($N_D = 3$). In the following discussion, an acoustic excitation from upstream will refer to a downstream propagating $(m, \mu) = (0, 0)$ modal acoustic disturbance, imposed at the computational inflow boundary. Similarly, an acoustic excitation from downstream will refer to an upstream propagating (0,0) modal acoustic disturbance, imposed at the computational outflow boundary.

The computed axial eigenvalues of a far-field acoustic disturbance for an unsteady flow through the helical fan at $\omega = 3.332$ and $\sigma = 90\,\text{deg}$ are shown in Figure 11, where the numbers m, μ above each symbol indicate the circumferential (m) and radial (μ) mode order. The radial pressure modes, $p_{m\mu}^R(r)$, for $m = -1, 0, 1$ and $\mu = 0, 1, 2$ are identical to those shown in Figure 6. Only the disturbances in the (0,0) mode, for which the pressure shows little variation with radius, are of propagating type. The downstream propagating (0,0) excitation or response has an axial wave number, κ_ξ, of -1.662; an upstream propagating (0,0) disturbance, an axial wave number of 5.740. The remaining response modes attenuate with increasing distance from the blade row, and the disturbances in the (0,1) mode, which have one radial node (see Figure 6), have the lowest attenuation coefficient, i.e., $|\beta| = 2.114$.

Unsteady surface pressure distributions, as predicted using the 3D LINFLUX and the 2D LINFLO analyses, for the helical fan subjected to an acoustic excitation from upstream at $\omega = 3.332$ and $\sigma = 90\,\text{deg}$ are shown in Figures 12 and 13. Here, the real and imaginary components of the surface pressure are in- and out-of-phase, respectively, with the excitation pressure at the midspan leading-edge point. The LINFLUX predictions for the unsteady surface pressures at $r/r_D = 0.8, 0.9$ and 1.0, shown in Figure 12, indicate that the radial surface-pressure variations are small. As a result, the LINFLUX and LINFLO surface-pressure predictions at $r/r_D = 0.9$, given in Figure 13, are in good agreement. Again we can attribute the small differences to the radial gradients that exist in the three-dimensional flow. According to the LINFLUX solution, the unit-amplitude pressure excitation from upstream gives rise to upstream and downstream propagating (0,0) acoustic response waves that have amplitudes of 0.617 and 0.519, respectively, in the far upstream ($\xi \leq \xi_-$) and far downstream ($\xi \geq \xi_+$) regions of the flow. The corresponding LINFLO amplitude predictions are 0.694 and 0.517. The amplitudes of the attenuating acoustic response waves are small at the computational inflow ($\xi = \xi_-$) and outflow ($\xi = \xi_+$) boundaries, which is indicative of a highly two-dimensional unsteady flow within the computational domain.

Contours of the in-phase component, $\mathrm{Re}\{p\}$, of the unsteady pressure at midspan, as predicted by the LINFLUX and LINFLO analysis, for the unsteady flow driven by the acoustic excitation from upstream at $\omega = 3.332$ and $\sigma = 90\,\mathrm{deg}$ are shown in Figure 14. Again, the results of the two analyses are in very good agreement. It is important to note that the LINFLUX results show no acoustic reflections at the computational inflow and outflow boundaries, thereby indicating a successful coupling of the near-field, finite-volume and the far-field eigenanalyses.

Results similar to those shown in Figures 12, 13 and 14, but for an acoustic excitation from downstream at $\omega = 3.332$ and $\sigma = 90\,\mathrm{deg}$, are given in Figures 15, 16 and 17. The LINFLUX calculations indicate that the unit-amplitude, (0,0), acoustic excitation from downstream occurs at $\kappa_\xi = 5.740$ and produces propagating, (0,0), acoustic responses at amplitudes of 0.560 and 0.266 in the far upstream and far downstream regions, respectively. This excitation also produces attenuating, (1,0), acoustic responses at amplitudes of 0.111, at both the computational inflow and outflow boundaries, indicating some three-dimensional content (cf. Figure 6) to the unsteady flow in the near field. The LINFLO results also indicate an excitation wave number of 5.740, and upstream and downstream propagating acoustic responses at amplitudes of 0.686 and 0.266. The amplitudes of the higher order response modes are small.

The three-dimensional content in the near-field unsteady flow is illustrated by the unsteady surface pressure distributions at the hub, midspan and tip of the helical fan, shown in Figure 15, and the differences between the LINFLUX and LINFLO surface pressure predictions at midspan given in Figure 16. Note that the 2D and 3D surface pressure responses at midspan are in good qualitative agreement, but the radial variations in the three-dimensional unsteady flow cause some differences. The unsteady pressure contours at midspan, as predicted by the LINFLUX and LINFLO analyses (see Figure 17), are also in good agreement. It should be noted that the LINFLUX calculation for the acoustic excitation from downstream was also performed on a $161 \times 51 \times 17$ mesh, with only slight changes in the response predictions.

The highly two-dimensional, $(m, \mu) = (0, 0)$, acoustic excitations at $\omega = 3.332$ and $\sigma = 90\,\mathrm{deg}$ produce unsteady flows through the helical fan in which one nearly two-dimensional (0,0) acoustic response disturbance exists in both the far upstream and the far downstream regions of the flow (cf. Figure 11). In contrast, if we consider (0,0) acoustic excitations arising from the aerodynamic interactions between the fan rotor and an adjacent upstream or downstream stator consisting of 21 vanes, i.e., acoustic excitations at $\omega = -N_V\Omega = 3.887$ and $\sigma = 2\pi(N_B - N_V)N_B = 45\,\mathrm{deg}(N_D = 3)$, two propagating acoustic response disturbances persist in each far-field region (Figure 18). This could be indicative of more significant radial variations in the near-field unsteady response.

The axial eigenvalues of the modal acoustic responses in the far field of the helical fan, subjected to an unsteady excitation at $\omega = 3.887$ and $\sigma = 45\,\mathrm{deg}$, are shown in Figure 18. These results indicate that there are two propagating acoustic disturbances, at, $(m, \mu) = (0, 0)$ and $(m, \mu) = (1, 0)$, in each of the far-field regions. The (0,0) and (1,0) downstream traveling disturbances occur at axial wave numbers of -1.980 and 1.925, respectively, the corresponding upstream propagating disturbances at 6.058 and 6.229, respectively. The remaining modes attenuate, with the (0,1) mode having the lowest attenuation coefficient. The radial modes of the lowest-order modal acoustic disturbances are similar, but not identical, to those shown

in Figure 6. The (0,0) modes are almost constant, but the (1,0) and (0,1) modes show significant radial variation.

Unsteady surface pressure responses, as predicted using the LINFLUX and LINFLO analyses, for the helical fan subjected to (0,0) acoustic excitations from upstream and downstream at unit amplitude, $\omega = 3.887$, and $\sigma = 45$ deg are given in Figures 19 through 22. For the upstream excitation, the surface pressure distributions at the hub, midspan and tip (Figure 19) show moderate variations along the span and fairly significant differences between the LINFLUX and LINFLO results at midspan (Figure 20). The LINFLUX calculations indicate that the unit-amplitude acoustic excitation from upstream produces propagating (0,0) and (1,0) acoustic response disturbances with amplitudes of 0.483 and 0.033 far upstream and with amplitudes of 0.674 and 0.284 far downstream. The corresponding LINFLO results are 0.603 and 0.378 upstream and 0.660 and 0.344 downstream. The remaining acoustic response disturbances have attenuated to low amplitudes at the computational inflow and outflow boundaries. The large differences between the LINFLUX and LINFLO predictions for the amplitude of the (1,0), upstream traveling acoustic response wave may be due to three-dimensional effects, or to the use, with LINFLUX, of a mesh with insufficient density to accurately capture the upstream traveling acoustic response.

The predicted surface pressure responses to the acoustic excitation in the (0,0) mode from downstream show a much stronger three-dimensional content, cf. Figure 21, and, therefore, more significant differences between the 3D and 2D predictions at midspan, cf. Figure 22. The downstream excitation produces (0,0) and (1,0) propagating three-dimensional pressure responses at amplitudes of 0.167 and 0.172 far upstream and at 0.178 and 1.350 far downstream. The corresponding 2D LINFLO results are 0.204 and 0.480 upstream and 0.205 and 1.586 downstream. It is interesting to note that, according to both calculations, the downstream excitation in the $m = 0$ circumferential mode produces a much stronger far-downstream response in the (1,0) mode than in the (0,0) mode. The relatively strong response in the (1,0) mode far-downstream is indicative of significant radial variations throughout the three-dimensional, unsteady flow field.

6.2 3D Tenth Standard Configuration

The 3D 10th Standard Cascade consists of 24 straight (untwisted) blades. The mean positions of the blade chord lines are defined by

$$r\theta = \xi \tan\Theta + nG(r),\ 0 \le \xi \le \cos\Theta,\ n = 0, \ldots, N_B - 1\ . \tag{6.5}$$

Therefore, the blade-chord, leading edges lie in the axial plane $\xi = \xi_{le} = 0$ along the entire span, and the axial chord length, c_{ax}, is $\cos\Theta$. The blade sections at all radial stations are those of a modified NACA 5506 airfoil, i.e., the thickness distribution of the standard NACA airfoil has been altered slightly [Ver89a], so that the blade sections close in wedge-shaped trailing edges. The blades are staggered at an angle, Θ, of 45 deg and have a circumferential spacing, $G = 2\pi r/N_B$, of unity at midspan. The blade row operates in a uniform axial inlet flow, which occurs at $M^{abs}_{-\infty} = 0.4015$, and rotates at angular speed of $|\Omega| = 0.2145$. This geometry and flow condition were chosen to match the subsonic Tenth Standard Configuration [FV93] at midspan, where the relative inlet Mach number, $M_{-\infty}$, and the relative inlet flow angle, $\Omega_{-\infty}$, are 0.7 and 55 deg, respectively.

The steady, surface, Mach number distributions, as predicted using TURBO and CASPOF analyses, for the 3D and 2D, 10th Standard Cascades, are shown in Figure 23. The inlet and exit, mean-flow quantities for the 3D calculation are given in Figure 24. For the CASPOF, full potential calculation, the relative inlet Mach number, $M_{-\infty} = 0.7$, and inlet flow angle, $\Omega_{-\infty} = 55\,\text{deg}$, are prescribed and a Kutta condition is imposed at the blade trailing edges. For the TURBO calculation the mean-flow, total pressure, total temperature, and inlet flow angle are specified at the inlet (i.e., at $\xi = \xi_- = -c_{\text{ax}}$), and the mean-flow static pressure at the hub is specified at the exit ($\xi = c_{\text{ax}}$), so that the relative inlet flow at midspan matches the 2D conditions.

The TURBO steady-flow predictions at the hub, $r/r_{\text{D}} = 0.8$, midspan, $r/r_{\text{D}} = 0.9$, and tip, $r/r_{\text{D}} = 1.0$, given in Figure 23, indicate that although the Mach numbers on the blade suction and pressure surfaces show moderate variations with radius, the variation in steady blade loading is small. Also, the 3D TURBO predictions at midspan are in close agreement with the 2D CASPOF predictions. The TURBO results indicate that the maximum Mach numbers on the suction surface of a blade are 0.849 at the hub, 0.906 at midspan, and 0.961 at the tip. These values occur at $\xi/c_{\text{ax}} = 0.053$, 0.073 and 0.085, respectively. Thus, the flow is very close to Mach one in the tip region, along a blade suction surface, just aft of the leading edge. The CASPOF predictions for the 2D cascade indicate a maximum Mach number of 0.916 at $\xi = 0.065$.

For the three-dimensional flow, the steady pressure ($P = 1.4577$), density ($\bar{\rho} = 1.0$), and axial velocity ($V_\xi = 0.5736$) have constant values at inlet and the relative circumferential velocity, $V_\theta = -\Omega r$ varies linearly from 0.7283 at the hub to 0.9103 at the tip. At the computational exit boundary, the steady pressure, density, and axial velocity vary with radius (mean shear), and the circumferential velocity varies nonlinearly with radius (mean swirl). As indicated in Figure 24, the steady blade loading causes increases in the pressure and density and decreases in the axial and circumferential velocities, especially the latter.

Blade Vibrations

The 3D LINFLUX and the 2D LINFLO analyses have been applied to predict the unsteady aerodynamic responses of the 3D and 2D 10th Standard Cascades to pure bending and pure torsional blade vibrations at unit frequency and at nodal diameters of $-6, -5, \ldots, 18$. The predicted axial eigenvalues and radial pressure modes, $p^R_{m\mu}(r)$, for the acoustic modes at $m = -1, 0, 1$, $\mu = 0, 1, 2$ are shown in Figures 25 and 26, respectively, for an unsteady excitation at $\omega = 1$ and $N_D = 6$ ($\sigma = 90\,\text{deg}$). Because of mean blade loading, the steady inlet and exit conditions for the 3D 10th Standard Cascade differ. As a result, the acoustic properties, $\chi_{m\mu}$ and $p^R_{m\mu}$, in the far-upstream region of the flow differ from those in the far-downstream region. In particular, for an unsteady excitation at $\omega = 1$ and $\sigma = 90\,\text{deg}$, the acoustic disturbances in the (0,0) mode are of propagating type far upstream, but, of attenuating type far downstream. Since propagating acoustic response disturbances exist in the upstream region, the unsteady excitation at $\omega = 1$ and $\sigma = 90\,\text{deg}$ is classified as superresonant. If this excitation is a prescribed blade vibration, only acoustic response disturbances will occur in the far-field.

In the far-upstream region of an unsteady flow at $\omega = 1$ and $\sigma = 90\,\text{deg}$ through the 3D 10th Standard Cascade, the propagating acoustic response disturbance has an axial wave

number, κ_ξ, of 1.583 and the least damped or (0,1) response disturbance has an attenuation constant, β, of 3.990. In the far-downstream region, $\beta = -1.084$ for the least-damped or (0,0) response disturbance. Since the far-downstream mean flow is nonuniform, the axial wave numbers of the attenuating disturbances in a given circumferential mode vary with radial mode number, μ, as indicated by the results in Figure 25, particularly those for $m = 1$.

The radial eigenmodes for the pressures associated with the far upstream acoustic excitations or responses and the far downstream acoustic responses for an unsteady excitation at $\omega = 1$ and $\sigma = 90$ deg are shown in Figure 26. Although the inlet and exit mean-flow conditions differ, the upstream and downstream radial pressure modes are very similar, with the downstream modes showing a somewhat greater radial variations than their upstream counterparts. Note that the phase of a modal pressure disturbance is independent of radius for the uniform absolute mean flow at inlet, but the phase varies with radius for the mean flow with swirl and axial shear that exists in the far downstream region. Thus, the far-upstream, pressure modes, $p^R(r)$, are purely real, but the far-downstream modes have some imaginary or out-of phase content.

Local (w_C) and global (W_C) work per cycle predictions for the 3D 10th Standard Cascade undergoing pure torsional and pure bending vibrations at $\omega = 1$ and $\sigma = -90$ deg ($N_D = -6$) and at $\omega = 1$ and $\sigma = 90$ deg ($N_D = 6$) are shown in Figure 27, where the LINFLUX local response predictions are given at the hub ($r/r_D = 0.8$), midspan ($r/r_D = 0.9$), and at the tip ($r/r_D = 1.0$). These results indicate that the local work per cycle responses to the blade torsional and bending blade vibrations do not vary significantly along the span, however, the results for the bending vibrations show greater radial variations than those for the torsional motions. The LINFLUX calculations for the subresonant $\sigma = -90$ deg and the superresonant $\sigma = 90$ deg blade motions reveal that, for the most part, the far-field acoustic responses are of small amplitude at the computational inflow and outflow boundaries. However, the superresonant torsional and bending vibrations at $\sigma = 90$ deg produce upstream propagating acoustic response disturbances which have amplitudes, a_A, of 1.352 and 1.540, respectively, and occur at an axial wave number, κ_ξ, of 1.583. The corresponding LINFLO predictions are $a_A = 1.529$ and 2.822 and $\kappa_\xi = 1.603$. Thus, there is a substantial difference between the LINFLUX and LINFLO predictions for the upstream propagating, (0,0), acoustic response wave caused by the bending vibration.

Local work per cycle predictions at midspan, as determined from the 3D LINFLUX and the 2D LINFLO analyses, for the 10th Standard Cascade vibrating in torsion and bending are shown in Figures 28 and 29, respectively, for blade motions at unit frequency and at interblade phase angles, σ, of -90 deg, 0 deg, $+90$ deg and $+180$ deg. The motions at $\sigma = 0$ deg and 90 deg are superresonant. For the in-phase motions at $\sigma = 0$ deg, propagating acoustic response disturbances, at $(m, \mu) = (0, 0)$, occur both upstream and downstream of the blade row. For the motions at $\sigma = 90$ deg, such a disturbance only occurs in the upstream region. For the (subresonant) motions at -90 deg and $\sigma = 180$ deg all acoustic response disturbances attenuate.

The 3D LINFLUX and the 2D LINFLO predictions, given in Figure 28, for the torsional blade vibrations are in very good agreement. Those, in Figure 29, for the bending vibrations at $\sigma = -90$, 0 and 180 deg show small differences over the entire blade. The reasons for these differences are not understood at present, but similar discrepancies have been reported in our earlier work in which the predictions of 2D nonlinear [AV94, AV96] and 2D linearized

[VMK95, MV95] Euler analyses were compared with LINFLO results. The local work per cycle predictions for the bending vibration at $\sigma = 90\,\text{deg}$ show similar small differences along the pressure surface, but large differences on the suction surface over the forward half of the blade. The reasons for the large discrepancies along the suction surface have not been established at this time. However, we suspect that local, high-wave-number, acoustic responses, occurring in regions of high-subsonic steady Mach number, are not adequately resolved on the $141 \times 41 \times 11$ H-mesh used for the LINFLUX calculations.

Global work per cycle predictions for the 2D and 3D 10th Standard Cascade cascades undergoing prescribed blade vibrations are shown in Figure 30, where results for the global work per cycle versus interblade phase angle are given for pure torsional vibrations about midchord and pure bending vibrations at unit frequency. The 3D LINFLUX results, indicated by the discrete symbols in Figure 30, have been determined for $N_D = -6, -5, \ldots, 18$; the 2D LINFLO results, for $-90\,\text{deg} \leq \sigma \leq 270\,\text{deg}$ in increments of one degree. As in the case of the helical fan, we have multiplied the 2D work per cycle predictions by the blade span, $r_D - r_H = 0.2\ r_D = 0.849$, to allow a convenient comparison between the 3D LINFLUX and the 2D LINFLO predictions. Also, the vertical lines above the curves in Figure 30 indicate the cut-off or resonance conditions, for the 2D cascade vibrating at $\omega = 1$ and, therefore, approximate resonance conditions, at $\omega = 1$, for the 3D configuration.

The resonance or cut-off conditions for the two-dimensional configuration are $\sigma^-_{-\infty} = -26.93\,\text{deg}$ and $\sigma^+_{-\infty} = 117.12\,\text{deg}$ in the far upstream region and $\sigma^-_{+\infty} = -31.80\,\text{deg}$ and $\sigma^+_{+\infty} = 59.79\,\text{deg}$ in the far downstream region. The superresonant blade motions at $\omega = 1$ and at interblade phase angles between these cut-off values send a propagating wave into the upstream and/or downstream regions of the flow. The blade motions at $-90\,\text{deg} \leq \sigma < -31.80\,\text{deg}$ and $117.12\,\text{deg} < \sigma \leq 270\,\text{deg}$ are subresonant. The results in Figure 30 indicate a very good agreement between the 3D LINFLUX and the 2D LINFLO global response predictions over the entire nodal diameter or interblade phase angle range of blade vibrations. We should note, however, that for superresonant bending vibrations at $\sigma = 75$, 90 and 105 deg, in which a propagating acoustic response disturbance occurs far upstream, but all other acoustic response disturbances attenuate, the LINFLUX and LINFLO local responses show large differences along a blade suction surface. These are similar in magnitude to those revealed by the local work per cycle predictions in Figure 29 for the bending vibration at $N_D = 6$.

Acoustic Excitations

We proceed to consider the unsteady pressure responses of the 10th Standard Cascade to acoustic excitations at $\omega = -N_V\Omega$ and $\sigma = 2\pi(N_B - N_V)/N_B$, that result from the aerodynamic coupling between the fan and an adjacent stator consisting of N_V vanes. First, we consider upstream and downstream stators consisting of 15 vanes, and therefore, acoustic excitations at $\omega = 3.218$ and $\sigma = 135\,\text{deg}$ ($N_D = 9$); then, an upstream stator consisting of 18 vanes, which produces an acoustic excitation at $\omega = 3.861$ and $\sigma = 90\,\text{deg}$ ($N_D = 6$). As in our discussion on the helical fan, an acoustic excitation from upstream refers to a downstream propagating $(m, \mu) = (0, 0)$ acoustic disturbance, imposed at the computational inflow boundary. Similarly, an acoustic excitation from downstream refers to an upstream propagating (0,0) acoustic disturbance, imposed at the computational outflow boundary.

The computed axial eigenvalues of the far-field acoustic disturbances associated with unsteady flows, at $\omega = 3.218$ and $\sigma = 135\,\text{deg}$, through the 3D 10th Standard Cascade are shown in Figure 31, where the numbers m, μ associated with each symbol indicate the circumferential (m) and radial (μ) mode number. For the flows considered, only the (0,0) modes, in which the pressure shows small variations with radius, are of propagating type. In the upstream or inlet region, the downstream propagating (0,0) disturbance (excitation) has an axial wave number, κ_ξ, of -1.712; the upstream propagating (0,0) disturbance (response), an axial wave number of 5.147. In the downstream or exit region, the upstream and downstream propagating (0,0) disturbances have axial wave numbers of 3.146 and -0.949, respectively. The remaining response modes attenuate with increasing distance from the blade row, and the disturbances in the (0,1) mode, which have one radial node, have the least attenuation, i.e., $\beta = 2.235$ far upstream and $\beta = -3.446$ far downstream.

Unsteady surface pressure distributions, as predicted using the 3D LINFLUX and the 2D LINFLO analyses, for the 3D 10th Standard Cascade, subjected to a unit-amplitude acoustic excitation from upstream at $\omega = 3.218$, $\sigma = 135\,\text{deg}$ and $(m, \mu) = (0, 0)$, are shown in Figures 32 and 33. Here, the real and imaginary components of the pressure are in- and out-of-phase, respectively, with the excitation pressure at the blade chord leading-edge, $\xi = 0$. The LINFLUX predictions for the unsteady surface pressures at $r/r_D = 0.8, 0.9$ and 1.0, in Figure 32, show moderate variations with radius along the blade suction surface, but very small variations along the pressure surface. The LINFLUX and LINFLO surface pressure predictions at midspan, in Figure 33, show good agreement on the blade pressure surface, but poor agreement on the suction surface. We suspect that the combination of high-subsonic steady Mach numbers along the suction surface and a relatively high unsteady excitation frequency, lead to local attenuating acoustic responses at high wave numbers, that are not resolved on the $141 \times 41 \times 11$ H-grid used for the LINFLUX calculations. Note that the 2D and 3D results agree on the pressure surface where the steady Mach numbers are lower.

The LINFLUX results for the downstream traveling acoustic excitation at $\omega = 3.218$ and $\sigma = 135\,\text{deg}$ indicate that the unit-amplitude pressure excitation from upstream gives rise to upstream and downstream propagating, (0,0), acoustic response waves at amplitudes of 0.691 and 0.683, respectively, in the far upstream ($\xi \leq \xi_-$) and far downstream ($\xi \geq \xi_+$) regions of the flow. The corresponding LINFLO predictions are 0.958 and 0.607, respectively. Both analyses indicate that the amplitudes of the attenuating acoustic response waves at the computational inflow ($\xi = \xi_-$) and outflow ($\xi = \xi_+$) boundaries are small, which should be indicative of a highly two-dimensional unsteady flow within the computational domain. However, the steady Mach number variations along the span and the relatively high Mach numbers along the suction surfaces of the blades (see Figure 23) seem to cause significant three-dimensional unsteady aerodynamic responses in the vicinities of the blade suction surfaces.

Contours of the in-phase component, $\text{Re}\{p\}$, of the unsteady pressure at midspan, as predicted by the LINFLUX and LINFLO analysis, for the unsteady flow driven by the acoustic excitation from upstream are shown in Figure 34. The results of the two analyses are in good qualitative agreement, but there are important quantitative differences, particularly in blade leading-edge regions, along the suction surfaces of the blades, and upstream of the blade row. Again, the LINFLUX results show no spurious acoustic reflections at the

computational inflow and outflow boundaries, indicating a successful coupling of the near-field, finite-volume and the far-field eigenanalyses.

Results similar to those shown in Figures 32–34, but for an acoustic excitation from downstream at unit amplitude, $\omega = 3.218$, $\sigma = 135\,\text{deg}$ and $(m, \mu) = (0, 0)$, are given in Figures 35–37. The LINFLUX analysis indicates that the acoustic excitation occurs at $\kappa_\xi = 3.146$ and produces propagating, (0,0), acoustic response disturbances, at amplitudes of 0.579 and 0.183, in the far upstream and far downstream regions, respectively. The LINFLO analysis indicates that $\kappa_\xi = 3.172$ and amplitudes of the propagating acoustic waves of 0.908 upstream and 0.228 downstream. Both analyses predict that the amplitudes of the attenuating acoustic responses are small at the computational inflow and outflow boundaries.

The unsteady surface pressure distributions at the blade hub, midspan and tip of the 3D blades, see Figure 35, indicate relatively strong radial variations along the suction surfaces. Also, as in the previous example, there are significant differences between the LINFLUX and LINFLO suction-surface pressure predictions at midspan, see Figure 36. Note, however, that the 2D and 3D pressure responses on the pressure surface, where the steady Mach numbers are lower, are in fairly good agreement. The unsteady pressure contours at midspan, as predicted by the LINFLUX and LINFLO analyses, Figure 37, show qualitative agreement, but there are significant differences along the blade suction surfaces and upstream of the blade row.

As our final example, we will consider a (0,0) acoustic excitation arising from an adjacent upstream stator consisting of 18 vanes, i.e., an acoustic excitation from upstream at $\omega = -N_V\Omega = 3.861$ and $\sigma = 2\pi(N_B - N_V)N_B = 90\,\text{deg}(N_D = 6)$. In this case, two propagating acoustic response disturbances persist far upstream of the blade row and one such disturbance persists far downstream.

The axial eigenvalues of the modal acoustic disturbances in the far field of the 3D 10th Standard Cascade, subjected to an unsteady excitation at $\omega = 3.861$ and $\sigma = 90\,\text{deg}$, are shown in Figure 38. These results indicate that there are propagating acoustic disturbances, at $(m, \mu) = (0, 0)$ and $(m, \mu) = (1, 0)$, in the far-upstream region, and at $(m, \mu) = (0, 0)$ in the far-downstream region. In the upstream region, the (0,0) and (1,0) downstream propagating disturbances (excitations) occur at axial wave numbers, κ_ξ, of -2.212 and 1.567, respectively, the corresponding upstream propagating (responses) disturbances at 5.647 and 5.308. The remaining modes attenuate, with the (0,1) mode having the lowest attenuation coefficient, $\beta = 1.718$. The radial mode shapes of the lowest-order modal acoustic disturbances are similar, but not identical, to those shown in Figure 26. The (0,0) modes are almost constant, but the (1,0) and (0,1) modes show significant radial variation. In the far downstream region, the (0,0) excitation and response disturbances occur at $\kappa_\xi = 4.244$ and $\kappa_\xi = -1.865$, respectively, and the (0,1) response mode has an attenuation coefficient, β, of -1.170.

Unsteady pressure responses, as predicted using the LINFLUX and LINFLO analyses, for the 3D 10th Standard Cascade subjected to a (0,0) acoustic excitation from upstream at unit amplitude, $\omega = 3.861$ and $\sigma = 90\,\text{deg}$ are given in Figures 39 through 41. The surface pressure responses at the hub, midspan and tip (Figure 39) show a moderate variation along the span, but, again, there are significant differences between the LINFLUX and LINFLO predictions at midspan (Figure 40). The LINFLUX results indicate that the unit-amplitude acoustic excitation from upstream produces propagating (0,0) and (1,0) acoustic response disturbances at amplitudes of 0.676 and 0.099 far upstream and a propagating (0,0) response

at amplitude 0.768 far downstream. The corresponding LINFLO predictions are 0.481, 0.240 and 0.779, respectively. Both analyses indicate that the remaining, attenuating, acoustic response disturbances attenuate to low amplitudes at the computational inflow and outflow boundaries. Again, the computed in-phase pressure contours in Figure 41 are qualitatively similar, but the LINFLUX H-mesh solution does not contain the fine details of the unsteady pressure fields, between the blades and upstream of the blade row, that are predicted by the LINFLO composite-mesh calculation.

6.3 Discussion

At this point, we have presented numerous results for unsteady flows through a helical fan and a three-dimensional version of the 10th Standard Cascade. These results pertain to acoustically dominated unsteady flows in which the unsteady fluctuations are caused by prescribed blade vibrations or by prescribed acoustic disturbances at inlet or exit. They were determined using the 3D LINFLUX analysis and the 2D Smith [Smi72] and LINFLO [Ver93] analyses. LINFLUX is based on an implicit, flux-split, finite-volume scheme for solving the linearized Euler equations in the near field, which typically extends from one axial chord upstream to one axial chord downstream of the blade row, and eigenanalyses for the unsteady perturbations of fully-developed, axisymmetric, swirling mean flows in the far upstream and far downstream regions. For the unsteady flows considered herein, the eigenanalyses have been used to determine the lowest-order modal acoustic disturbances, the higher-order disturbances are assumed to be of negligible amplitude at the computational inflow and outflow boundaries, and the remaining part of the unsteady perturbation, consisting of convected and nearly convected disturbances, is simply convected out of the near-field domain through the computational outflow boundary.

Numerical Results

The numerical results indicate that the far-field eigenanalysis is capable of providing reasonable solutions for the axial eigenvalues and the radial pressure modes (see, e.g., Figures 5, 6, 25, and 26) of the acoustic excitations and responses that can exist far upstream and far downstream of a blade row. In particular, we have tested the numerical eigensolutions against analytical predictions for uniform absolute mean flows, and found excellent agreement. At this point, we have not applied the eigenanalysis to predict the axial eigenvalues and radial eigenmodes associated with nearly convected disturbances. The behavior of such disturbances is not well understood at present, as far-field eigenanalyses for non-uniform mean flows have become available only recently. It will be necessary to provide accurate numerical representations of nearly-convected, predominantly vortical, disturbances to predict the unsteady aerodynamic responses associated with wake/blade-row interactions. Therefore, this issue will be addressed in detail in the next phase of our LINFLUX development effort.

The LINFLUX local surface response predictions, i.e., ω_C vs ξ and $[\![p]\!]$ vs ξ (cf. Figures 7–9), for the helical fan undergoing pure torsional vibrations and pure bending vibrations show reasonable radial trends, and the predictions at blade midspan are in very good agreement with those based on the classical analysis of Smith. Similarly, the LINFLUX global work per cycle predictions, i.e., W_C vs σ (Figure 10) are in very good agreement with predictions based on the Smith analysis.

The local surface responses, predicted using the LINFLUX analysis, for acoustic excitations from upstream and downstream (Figures 12, 13, 15, 16 and 19–22) also show reasonable radial trends and, for the acoustic excitations at $\omega = 3.332$ and $\sigma = 90\,\text{deg}$ ($N_D = 6$), good agreement at midspan with the predictions of the 2D LINFLO analysis. The LINFLUX solutions for highly two-dimensional acoustic excitations at $\omega = 3.887$ and $\sigma = 45\,\text{deg}$ ($N_D = 3$) show strong radial variations, particularly for the excitation from downstream, therefore, as might be expected, the LINFLUX results at midspan differ from those of the LINFLO analysis. The unsteady pressure contours at midspan (Figures 14 and 17), predicted by the LINFLUX and LINFLO analyses, for the acoustic excitations at $\omega = 3.332$ and $\sigma = 90\,\text{deg}$, are in very good agreement, but the two analyses give slightly different predictions for the amplitudes of the far-upstream propagating acoustic response disturbances at $m = 0$. The LINFLUX pressure contours show no spurious acoustic reflections at the computational inflow and outflow boundaries; thereby, indicating a successful coupling of the LINFLUX near- and far-field solution procedures.

The TURBO predictions for the zeroth-order or steady relative flow at $M^{\text{abs}}_{-\infty} = M_{\xi,-\infty} = 0.4015$ through the 3D 10th Standard Cascade shows moderate variations in the blade-surface Mach numbers with radius, but only small variations in blade loading (Figure 23). In addition, the 3D Euler predictions for the surface Mach numbers at blade midspan are in close agreement with 2D full-potential predictions. The 3D 10th Standard Cascade operates in a uniform, axial, absolute, mean inlet flow, but, because of steady blade loading, the mean flow far downstream of the blade row (Figure 24) has swirl and axial shear.

The LINFLUX local unsteady response, i.e., w_C vs ξ, predictions (Figures 27–29) for the 3D 10th Standard Cascade, undergoing pure torsional and pure bending vibrations at $\omega = 1$, show small variations with radius and, for the most part, the results at midspan, are in good agreement with the 2D LINFLO predictions. However, the LINFLUX and LINFLO, local work per cycle results for a superresonant bending vibration at $\sigma = 90\,\text{deg}$ show significant differences along the blade suction surface. We suspect that these differences are due to an inadequate resolution, by LINFLUX, of the local, high wave number, upstream traveling, acoustic response disturbances that occur at high-subsonic, steady, Mach numbers. The LINFLUX and LINFLO global work per cycle, W_C vs σ, predictions for torsional and bending vibrations (Figure 30) are in very good agreement. However, the global results for the bending vibrations must be interpreted with some caution, as the local responses differ along blade suction surfaces at the interblade phase angles at which a propagating acoustic response disturbance exists far upstream of the blade row and all other acoustic responses attenuate.

The LINFLUX unsteady surface pressure predictions for the 3D 10th Standard Cascade, subjected to acoustic excitations from upstream (Figures 32, 34 39 and 40) or downstream (Figures 35 and 36), also show reasonable spanwise trends, but the LINFLUX and LINFLO predictions along the suction surface at midspan show substantial differences over the forward half of the blade. However, the unsteady pressure distributions on the lower or pressure surfaces of the blades, where steady Mach numbers are lower, are in good agreement. The LINFLUX and LINFLO predictions for the amplitudes of the upstream propagating acoustic response waves also show significant differences. We believe that the differences on the suction surface and far upstream stem from performing the LINFLUX calculations on an H-mesh that is too sparse to capture the upstream traveling acoustic response waves, that

occur near the suction surfaces of blades, in regions in which steady Mach numbers are close to one.

The unsteady pressure contours at midspan, as predicted by the LINFLUX and LINFLO analyses, for the flows through the 3D 10th Standard Cascade driven by acoustic excitations from upstream (Figure 34) and downstream (Figure 37) are in qualitative agreement, but significant quantitative differences occur in the vicinities of the blade leading edges, along the blade suction surfaces and upstream of the blade row. These differences suggest the regions in which the computational mesh, used for the LINFLUX calculations, should be refined.

Mesh Resolution Study

We have performed a brief study on an unsteady flow through the 2D 10th Standard Cascade to test whether LINFLUX results will approach those of LINFLO, if a re-distributed and more refined mesh is used for the LINFLUX calculations. For this purpose, we consider the unsteady flow excited by a unit-amplitude acoustic excitation from upstream at $\omega = 3.861$ and $\sigma = 90$ deg, and apply the 2D LINFLUX [MV95, VMK95] and LINFLO codes to predict the unsteady surface pressure distributions. The LINFLO results are the same as those shown in Figure 40. The 2D LINFLUX results, determined on a 141 $\times$ 41 grid which is similar to that used at midspan for the 3D LINFLUX calculations, agree closely with the midspan, 3D LINFLUX predictions shown in Figure 40. The 2D LINFLUX calculations were then performed on a re-distributed 141 $\times$ 41 grid in which more axial lines were placed upstream and over the forward half of the blade row. Following this calculation, 2D LINFLUX calculations were performed on refined meshes that were 1.5 and 2.0 times as dense as the re-distributed 141 $\times$ 41 mesh.

The results are shown in Figure 42, where it can be seen that the re-distribution of the original 141 $\times$ 41 mesh leads to LINFLUX surface-pressure predictions that are in better agreement with the corresponding LINFLO results. Moreover, as the mesh density is increased, the LINFLUX predictions approach those of LINFLO. In our future studies, similar grid re-distribution and density studies will be performed with the 3D LINFLUX analysis in an effort to determine the grid requirements for accurately resolving three-dimensional unsteady phenomena. At present, it appears that relatively large memory resources and CPU times will be required to achieve accurate acoustic response predictions using the 3D LINFLUX analysis.

Based on the numerical results presented in this report, we believe that the near- and far-field numerical algorithms used in the LINFLUX code are working properly and these algorithms have been successfully coupled. Also, it appears that the LINFLUX analysis is capable of providing accurate aerodynamic response information for unsteady flows driven by prescribed blade motions and/or acoustic excitations, provided that the computational grids used are sufficiently dense and properly distributed. LINFLUX mesh requirements should not impose any serious difficulties for blade flutter applications, but for the high frequency unsteady flows, associated with forced blade vibrations and blade-row noise generation, these requirements will be rather stringent. Hence, strategies for reducing mesh size, e.g., higher-order numerical approximations, both in the field and at blade surfaces, and/or the construction of a parallel version of LINFLUX may have to be considered.

7. Concluding Remarks

The LINFLUX, linearized unsteady aerodynamic analysis is being developed for turbomachinery aeroelastic and aeroacoustic design applications. This analysis is based on the Euler equations of fluid motion, a near-field, implicit, flux-split, finite-volume, analysis, and a far-field eigenanalysis for unsteady perturbations of a fully-developed, axisymmetric swirling mean flow. The near-field numerical model is based on the scheme used in the nonlinear unsteady analysis, TURBO [JHW92], and the far-field eigenanalysis, which is coupled to the near-field finite-volume analysis at computational inflow and outflow boundaries, allows incoming external aerodynamic excitations to be prescribed, and acoustic response disturbances to pass through these computational boundaries without spurious reflections. To date, this theoretical effort has been focused on formulating the linearized inviscid unsteady aerodynamic equations and the near- and far-field solution procedures, and on implementing these models, first, into a two-dimensional code [VMK95, MV95], and then, under the present effort, into a three-dimensional, linearized, unsteady aerodynamic code.

Under the present effort, we have applied the 3D LINFLUX analysis to predict unsteady subsonic flows through a helical fan and through a "real" blade configuration, i.e., a three dimensional version of the 10th Standard Cascade Configuration. We have considered unsteady flows excited by prescribed blade vibrations or by prescribed acoustic disturbances at inlet or exit that travel toward the blade row. In each case a highly two-dimensional excitation has been imposed, so that the LINFLUX predictions could be usefully compared and validated against predictions based on previous two-dimensional analyses.

The numerical results indicate that the current version of the 3D LINFLUX code is capable of providing accurate aerodynamic response information for unsteady subsonic flows, provided that the grids employed have a sufficient overall density and local clusterings in regions of high flow gradients. In particular, the numerical results indicate that the axial eigenvalues and radial eigenmodes of far-field acoustic disturbances can be accurately represented, and that the 3D blade-surface, response predictions show reasonable radial trends. Moreover, for the helical fan, the LINFLUX results at midspan are in very good agreement with those based on the Smith [Smi72] and LINFLO [Ver93] analyses. The LINFLUX and LINFLO results at midspan of the 3D 10th Standard Cascade are in good qualitative agreement, but in some cases significant quantitative differences occur. The latter appear along the suction surfaces of the blades, where steady Mach numbers are close to one, and upstream of the blade row. The present evidence suggests that the quantitative differences between the LINFLUX and LINFLO results can be eliminated if the meshes used in the LINFLUX calculations are of sufficient density and the grid lines are properly distributed.

Based on the numerical results presented in this report, it appears that the near- and far-field numerical algorithms, developed for the LINFLUX code, are working properly and that these algorithms have been successfully coupled. Also, the 3D LINFLUX analysis can yield useful response information for acoustically-dominated unsteady flows, i.e., flows excited by blade vibrations or acoustic disturbances. However, the mesh requirements for accurately resolving such flows must be better understood. The requirements for flutter applications, for which reduced frequencies are typically of order one, can be readily met, but those for forced vibration and aeroacoustic response studies, in which reduced frequencies on the order

of 5 to 50 must be considered, may impose serious constraints on available computational resources.

A number of computational strategies could be investigated to improve the performance of a TURBO/LINFLUX unsteady aerodynamic calculation. In particular, a rotating-frame version of the TURBO analysis could be constructed to allow more efficient predictions of nonlinear, steady background flows. Also, second-order accurate, surface boundary conditions could be installed to reduce the time required to achieve converged low-loss, steady solutions. In addition, strategies for reducing the mesh densities required to achieve accurate LINFLUX unsteady flows predictions should be investigated. Such strategies might entail the development of second-order accurate blade-surface conditions, fourth-order accurate field approximations, and the use of composite H–C meshes. A composite mesh capability would also be useful in the TURBO analysis for reducing the numerical losses that occur at the blade surfaces. Finally, because of the high frequencies involved, a parallel version of LINFLUX should be considered for forced blade vibration and blade-row aeroacoustic response studies.

In the next phase of our LINFLUX development effort, we will focus on the unsteady flows associated with wake/blade-row interactions. For such applications, the wakes must be modeled as a superposition of convected and nearly-convected disturbances, which are imposed at the computational inflow boundary. Their passage through the blade row and into the far-downstream region is determined by the LINFLUX, near- and downstream far-field analyses. Thus, for swirling mean flows, the present far-field eigenanalysis must be extended to determine nearly-convected modal disturbances, eliminate spurious or non-physical disturbances, and provide accurate descriptions of the axial and radial behaviors of the retained disturbances. Following this, the LINFLUX predictions for the unsteady responses to wake-type excitations must be determined and evaluated. Based on our earlier investigations with the 2D LINFLUX analysis [MV95, VMK95], we anticipate that higher-order boundary conditions will be needed to accurately model unsteady vortical behaviors near blade surfaces.

To date, we have focused on demonstrating and validating the 3D LINFLUX code for unsteady subsonic flows. This code can also be applied to predict unsteady transonic flows. But again, based on our earlier investigations with the 2D LINFLUX code [MV95, VMK95], improvements in shock modeling will be required, so that LINFLUX and its nonlinear counterpart, TURBO, which has excellent shock resolution capabilities, will provide consistent response information in the vicinities of moving shocks.

References

[AV94] T. C. Ayer and J. M. Verdon. Numerical Unsteady Aerodynamic Simulator for Blade Forced Response Phenomena. Contractor Report WL-TR-95-2011, prepared for the GUIde Consortium under U. S. Air Force Contract F33615-92-C-2212, December 1994.

[AV96] T. C. Ayer and J. M. Verdon. Validation of a Nonlinear Unsteady Aerodynamic Simulator for Vibrating Blade Rows. ASME Paper 96-GT-340, International Gas Turbine and Aeroengine Congress & Exhibition, Birmingham, UK, June 10-13. 1996. To be published in the *Trans. of the ASME: Journal of Turbomachinery.*

[BH92] T. A. Beach and G. Hoffman. IGB Grid: User's Manual (A Turbomachinery Grid Generation Code). NASA CR 189104, January 1992.

[Cas83] J. R. Caspar. Unconditionally Stable Calculation of Transonic Potential Flow through Cascades using an Adaptive Mesh for Shock Capture. *Transactions of the ASME: Journal of Engineering for Power*, 105(3):504-513, July 1983.

[FV93] T. H. Fransson and J. M. Verdon. Standard Configurations for Unsteady Flow through Vibrating Axial-Flow Turbomachine Cascades. In *Unsteady Aerodynamics, Aeroacoustics and Aeroelasticity of Turbomachines and Propellers*, pages 859-889. Edited by H. M. Atassi, Springer-Verlag, New York, 1993.

[GA96] V. V. Golubev and H. M. Atassi. Acoustic-Vorticity Waves in Swirling Flows. Technical report, Department of Aerospace and Mechanical Engineering, University of Notre Dame, Notre Dame, Indiana, 1996.

[Gil93] M. B. Giles. A Framework for Multi-Stage Unsteady Flow Calculations. In *Unsteady Aerodynamics, Aeroacoustics, and Aeroelasticity of Turbomachines and Propellers*, pages 57-72. Edited by H. M. Atassi, Springer-Verlag, New York, 1993.

[HC93a] K. C. Hall and W. S. Clark. Linearized Euler Predictions of Unsteady Aerodynamic Loads in Cascades. *AIAA Journal*, 31(3):540-550, March 1993.

[HC93b] D. G. Holmes and H. A. Chuang. 2D Linearized Harmonic Euler Flow Analysis for Flutter and Forced Response. In *Unsteady Aerodynamics, Aeroacoustics, and Aeroelasticity of Turbomachines and Propellers*, pages 213-230. Edited by H. M. Atassi, Springer-Verlag, New York, 1993.

[HCL94] K. C. Hall, , W. S. Clark, and C. B. Lorence. A Linearized Euler Analysis of Unsteady Transonic Flows in Turbomachinery. *Transactions of the ASME: Journal of Turbomachinery*, 116(3):477-488, July 1994.

[HL93] K. C. Hall and C. B. Lorence. Calculation of Three-Dimensional Unsteady Flows in Turbomachinery Using the Linearized Harmonic Euler Equations. *Transactions of the ASME: Journal of Turbomachinery*, 115(4):800-809, October 1993.

[HLC93] K. C. Hall, C. B. Lorence, and W. S. Clark. Nonreflecting Boundary Conditions for Linearized Unsteady Aerodynamic Calculations. AIAA Paper 93–0882, 31st Aerospace Sciences Meeting & Exhibit, Reno, Nevada, Jan 11–14 1993.

[HSR91] D. L. Huff, T. W. Swafford, and T. S. R. Reddy. Euler Flow Predictions for an Oscillating Cascade Using a High Resolution Wave-Split Scheme. Paper 91–GT–198, ASME International Gas Turbine and Aeroengine Congress and Exposition, Orlando, Florida, June 3–6 1991.

[JHW92] J. M. Janus, H. Z. Horstman, and D. L. Whitfield. Unsteady Flowfield Simulation of Ducted Prop-fan Configurations. Paper 92–0521, AIAA 30th Aerospace Sciences Meeting and Exhibit, Reno, Nevada, January 6-9 1992.

[KK93] G. Kahl and A. Klose. Computation of Time Linearized Transonic Flow in Oscillating Cascades. ASME Paper 93–GT–269, 38th International Gas Turbine and Aeroengine Congress and Exposition, Cincinnati, Ohio, May 24–27 1993.

[Kou95] K. A. Kousen. Eigenmode Analysis of Ducted Flows with Radially Dependent Axial and Swirl Components. In *Proceedings of the First Joint CEAS/AIAA Aeroacoustics Conference,* Vol, II, pages 1085–1094, Munich, Germany, June 12–15 1995.

[MM94] M. M. Morel and D. V Murthy. Turbomachinery Forced Response Prediction System: Users manual. CR 194465, NASA, March 1994. Prepared for NASA Lewis Research Center under Contract NAS3–25266 and Grant NAG3–1669.

[MV95] M. D. Montgomery and J. M. Verdon. A Linearized Unsteady Euler Analysis for Turbomachinery Blade Rows Using an Implicit Wave-Split Scheme. In *Unsteady Aerodynamics and Aeroelasticity of Turbomachines*, pages 143–160. Edited by Y. Tanida and M. Namba, Elsevier, Amsterdam, 1995.

[Nam87] M. Namba. Three Dimensional Flows. In *AGARD Manual on Aeroelasticity in Axial-Flow Turbomachines,* Vol. 1, *Unsteady Turbomachinery Aerodynamics*, chapter IV. Edited by M. F. Platzer and F. O. Carta, AGARD AG–298, March 1987.

[Roe81] P. L. Roe. Approximate Riemann Solvers, Parameter Vectors and Difference Schemes. *Journal of Computational Physics*, 43:357–372, 1981.

[SG91] A. P. Saxer and M. B. Giles. Quasi-3D Nonreflecting Boundary Conditions for Euler Equation Calculations. AIAA Paper 91–1603, 10th Computational Fluid Dynamics Conference, Honolulu, Hawaii, June 24–27 1991. pp. 845–857.

[SLH+94] T. W. Swafford, D. H. Loe, D. L. Huff, D. H. Huddleston, and T. S. R. Reddy. The Evolution of NPHASE: Euler/Navier-Stokes Computations of Unsteady Two-Dimensional Cascade Flow Fields. Paper 94–1834, AIAA 12th Applied Aerodynamics Conference, Colorado Springs, Colorado, June 20–23 1994.

[Smi72] S. N. Smith. Discrete Frequency Sound Generation in Axial Flow Turbomachines. R&M 3709, British Aeronautical Research Council, London, England, UK, March 1972.

[Smi90] T. E. Smith. Aerodynamic Stability of a High-Energy Turbine Blade. Paper 90–2351, AIAA/SAE/ASME/ASEE 26th Joint Propulsion Conference, Orlando, Florida, July 16–18 1990.

[SS90] A. Suddhoo and P. Stow. Simulation of Inviscid Blade-Row Interaction Using a Linearized Potential Code. Paper 90–1916, AIAA/SAE/ASME/ASEE 26th Joint Propulsion Conference, Orlando, Florida, July 16–18 1990.

[SS91] B. K. Soni and M. H. Shih. TIGER: Turbomachinery Interactive Grid GenERation. In *Proceedings of the Third International Conference on Numerical Grid Generation in CFD*, Barcelona, Spain, June 1991.

[SW81] J. L. Steger and R. F. Warming. Flux Vector Splitting of the Inviscid Gasdynamic Equations with Application to Finite Difference Methods. *Journal of Computational Physics*, 40(2):263–293, April 1981.

[TS62] J. M. Tyler and T. G. Sofrin. Axial Flow Compressor Noise Studies. *SAE Transactions*, 70:309–332, 1962.

[Ver89a] J. M. Verdon. The Unsteady Aerodynamic Response to Arbitrary Modes of Blade Motion. *Journal of Fluids and Structures*, 3(3):255–274, May 1989.

[Ver89b] J. M. Verdon. The Unsteady Flow in the Far Field of an Isolated Blade Row. *Journal of Fluids and Structures*, 3(2):123–149, March 1989.

[Ver93] J. M. Verdon. Unsteady Aerodynamic Methods for Turbomachinery Aeroelastic and Aeroacoustic Applications. *AIAA Journal*, 31(2):235–250, February 1993.

[VMK95] J. M. Verdon, M. D. Montgomery, and K. A. Kousen. Development of a Linearized Unsteady Euler Analysis for Turbomachinery Blade Rows. NASA CR 4677, prepared under Contract NAS3–25425 for NASA Lewis Research Center, June 1995.

[VTM82] C. S. Ventres, M. A. Theobald, and W. D. Mark. Turbofan Noise Generation, Volume 1: Analysis. CR 167952, NASA, July 1982.

[Whi87] D. S. Whitehead. Classical Two-Dimensional Methods. In *AGARD Manual on Aeroelasticity in Axial-Flow Turbomachines,* Vol. 1, *Unsteady Turbomachinery Aerodynamics,* Chapter III. Edited by M. F. Platzer and F. O. Carta, AGARD AG–298, March 1987.

[WJS88] D.L. Whitfield, J.M. Janus, and L.B. Simpson. Implicit Finite Volume High Resolution Wave Split Scheme for Solving the Unsteady Three-Dimensional Euler and Navier-Stokes Equations on Stationary or Dynamic Grids. Report MSSU–EIRS–ASE–88–2, Mississippi State Engineering and Industrial Research Station, 1988.

[WT91] D. L. Whitfield and L. Taylor. Discretized Newton-Relaxation Solution of High Resolution Flux-Difference Split Schemes. Paper 91–1539, AIAA 10th Computational Fluid Dynamics Conference, Honolulu, Hawaii, June 24–26 1991.

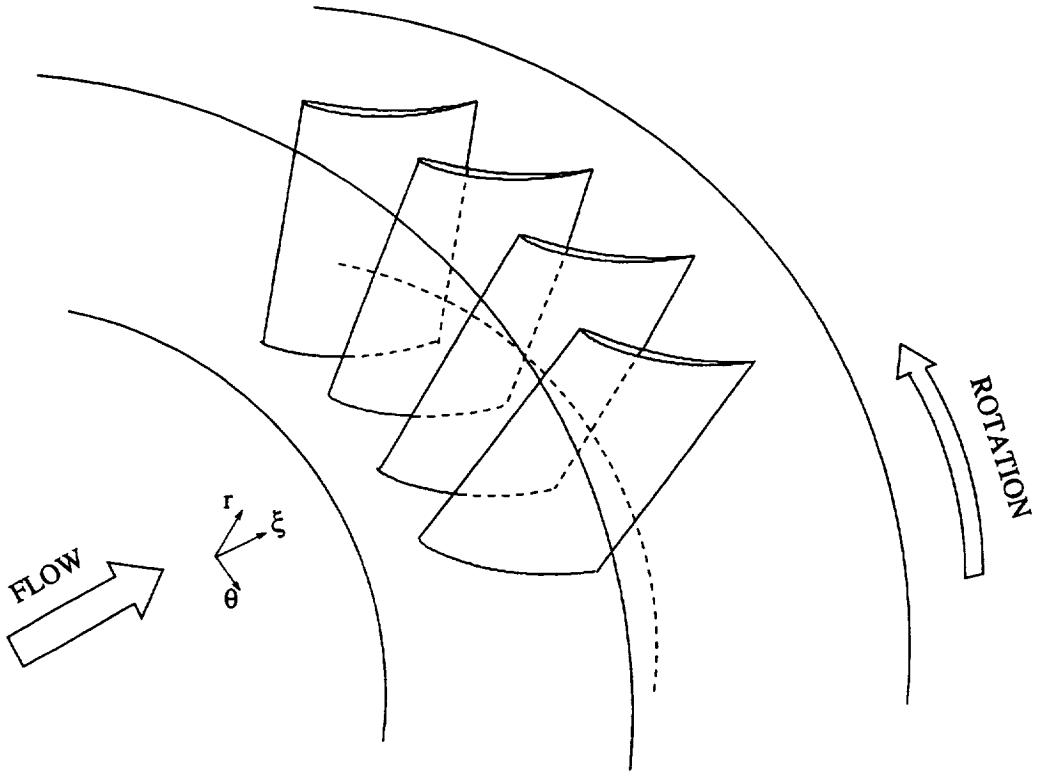

Figure 1: Rotating axial compressor blade row operating within an annular duct.

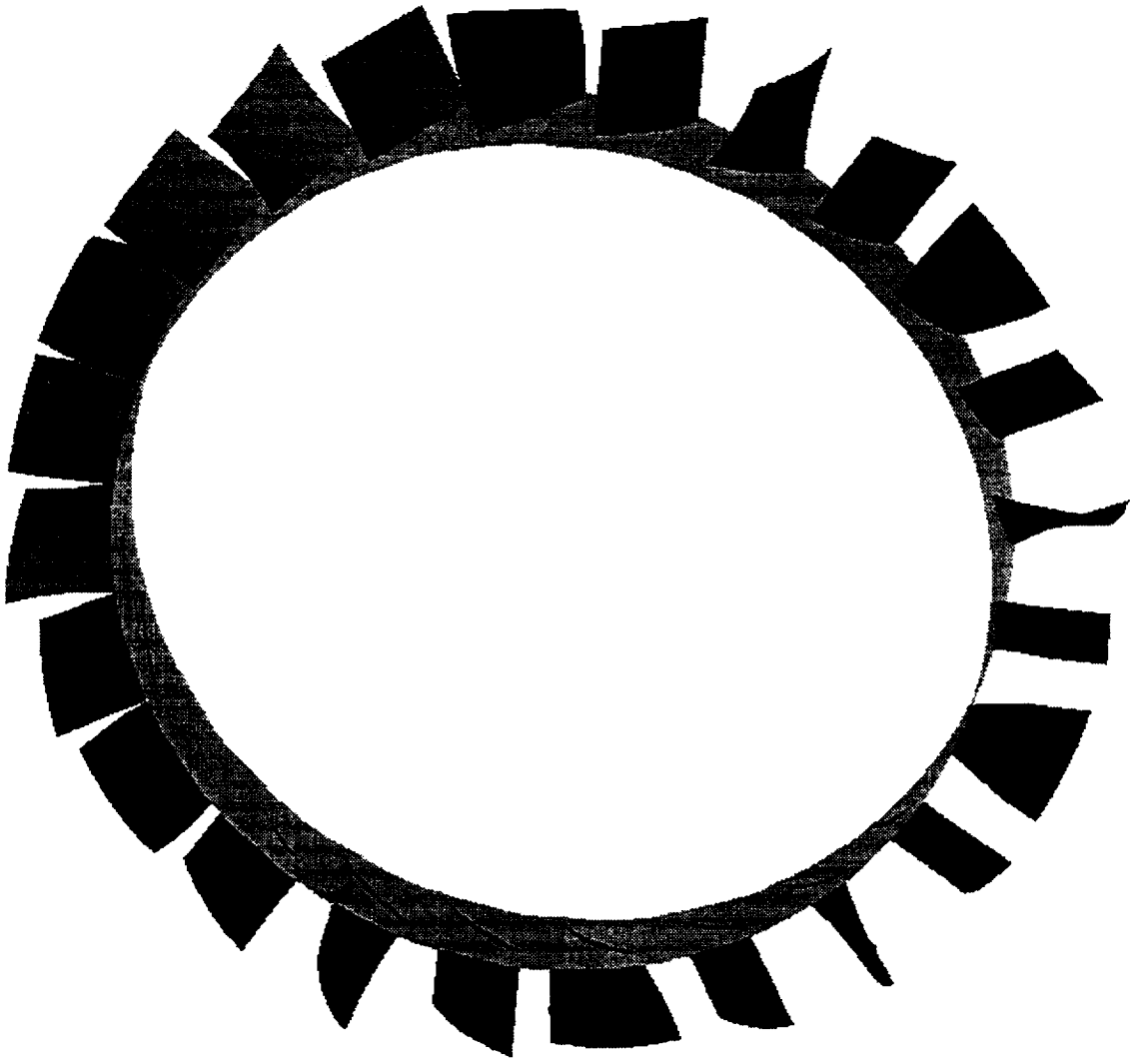

Figure 2: 3D Tenth Standard Configuration undergoing an exaggerated torsional motion ($\alpha_{hub} = 0$ deg, $\alpha_{tip} = 45$ deg). The rotor consists of 24 NACA 5506 airfoils staggered at 45 deg. The nodal diameter of the blade motion is 6, which results in an interblade phase angle of 90 deg. The outer casing has been eliminated from the figure for clarity.

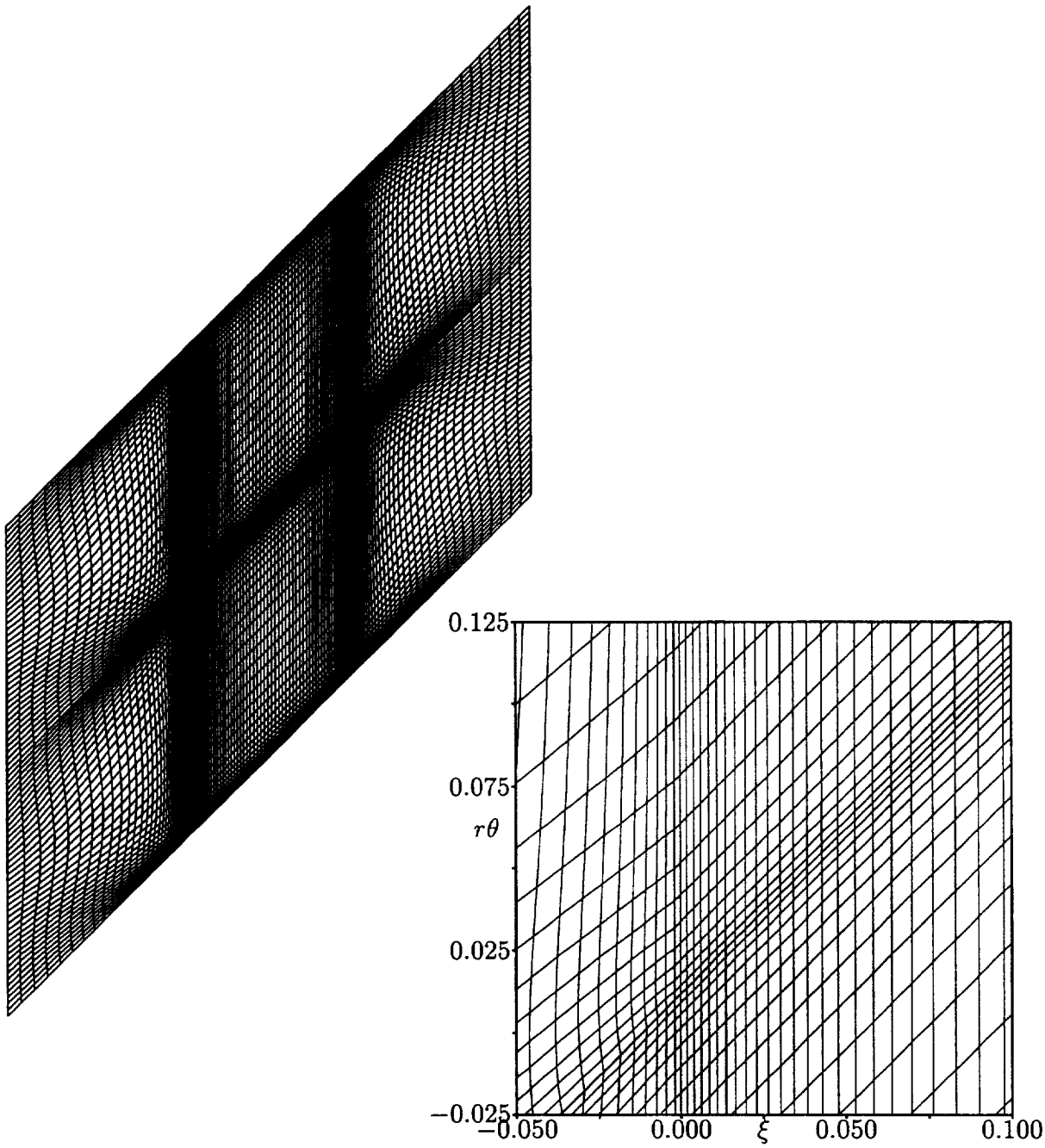

Figure 3: LINFLUX computational grid at midspan for the helical fan.

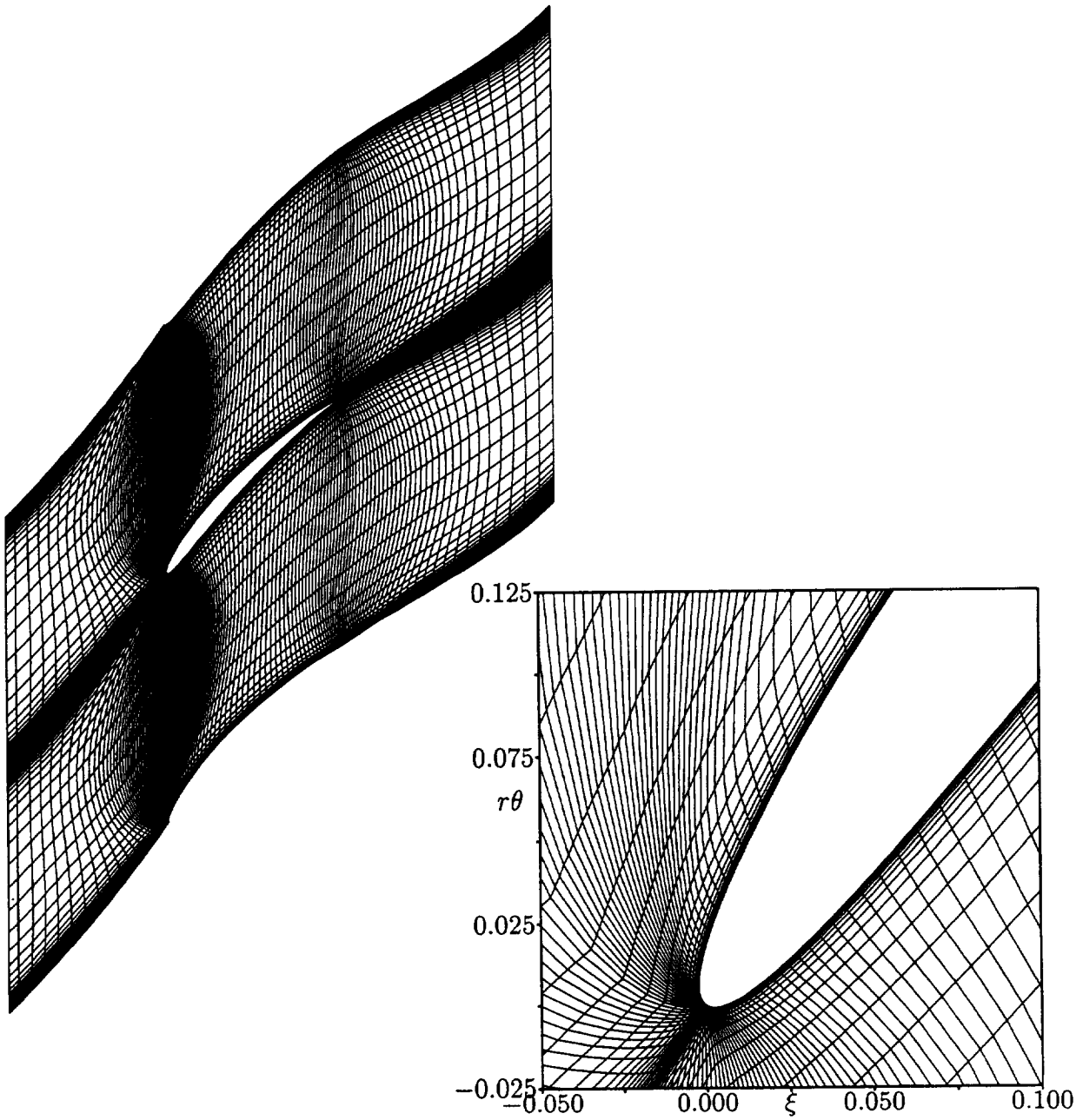

Figure 4: LINFLUX computational grid at midspan for the 3D 10th Standard Cascade.

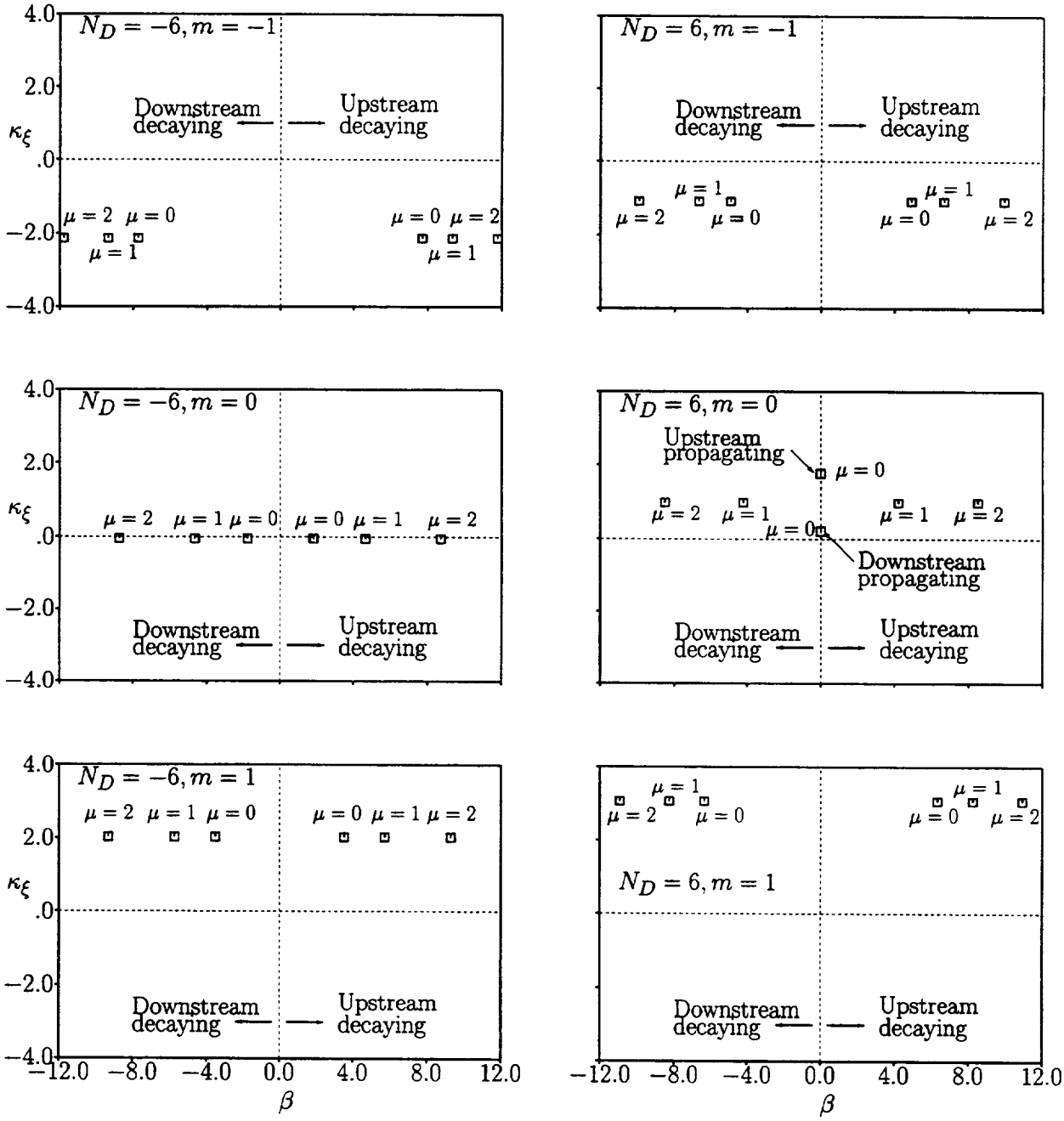

Figure 5: Axial eigenvalues, $\chi = \beta + i\kappa_\xi$, for three circumferential ($m = -1, 0, 1$) and three radial ($\mu = 0, 1, 2$) modes of acoustic disturbance in the far field of the helical fan, for unsteady flows at $\omega = 1.0$ and $N_D = \mp 6$.

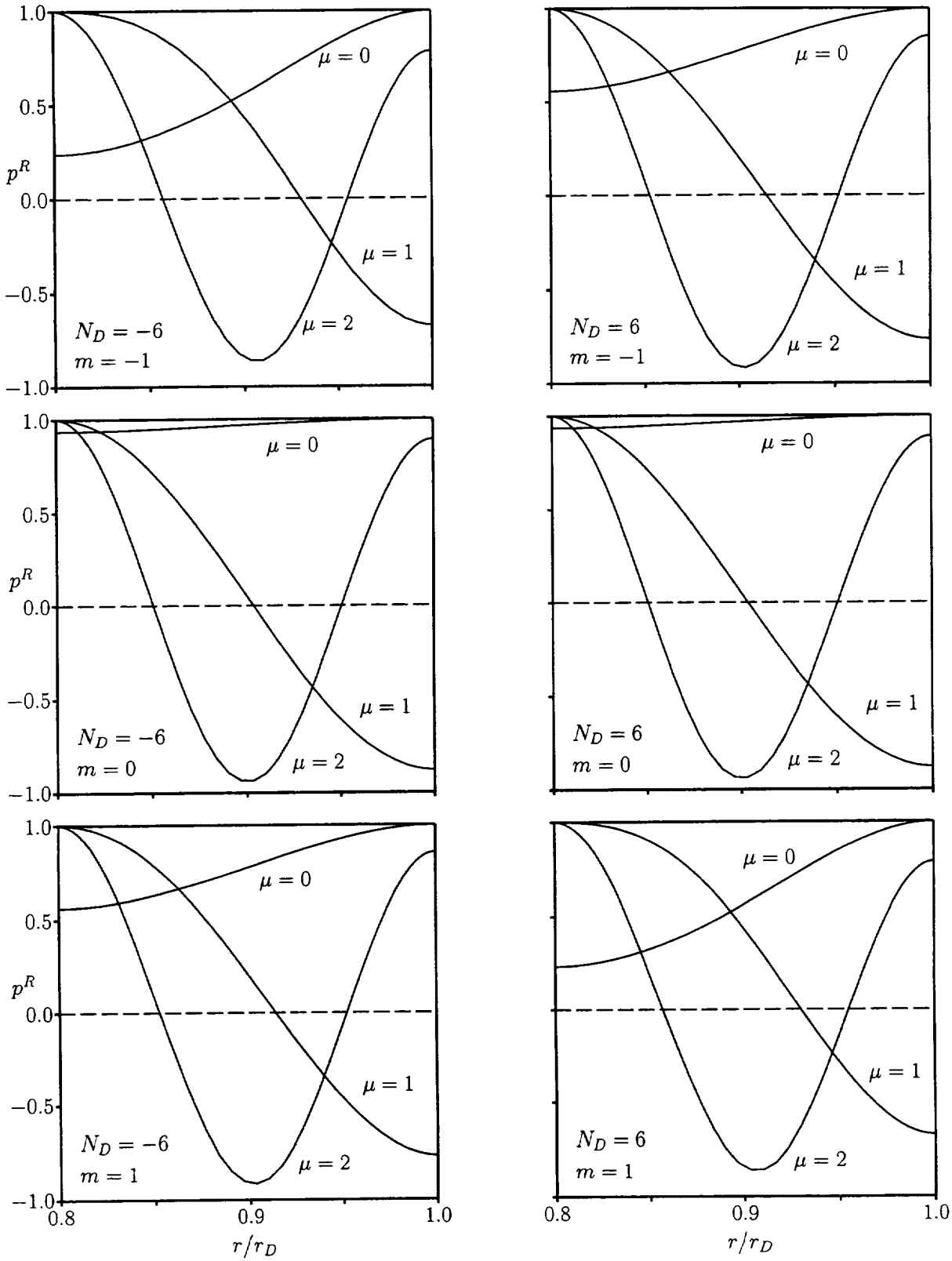

Figure 6: Radial pressure modes, $p^R_{m\mu}(r)$, $m = -1, 0, 1$, $\mu = 0, 1, 2$, for acoustic disturbances at $N_D = \mp 6$ in the far field of the helical fan.

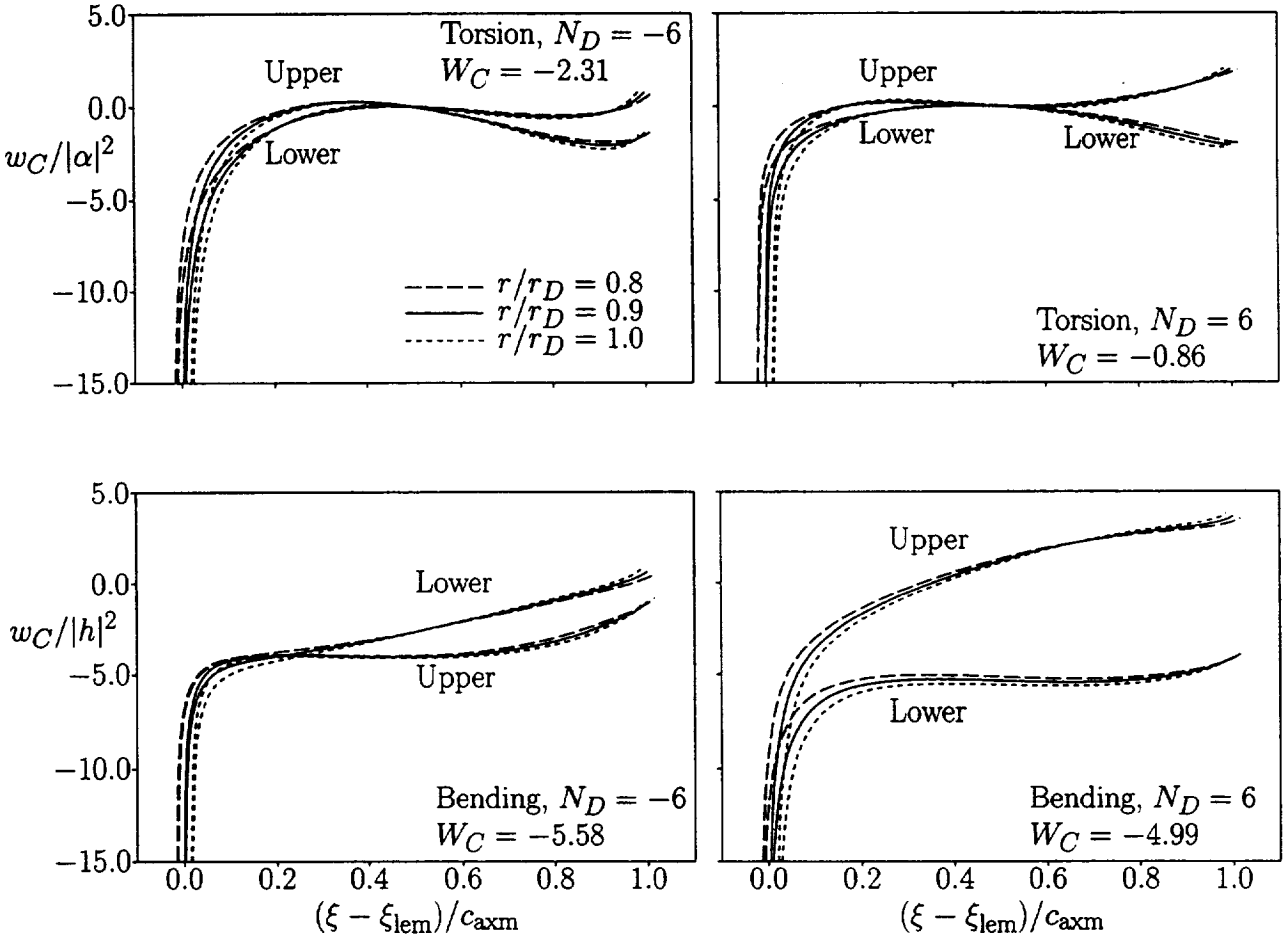

Figure 7: Local work per cycle distributions at $r/r_D = 0.8$ (– – –), $r/r_D = 0.9$ (——) and $r/r_D = 1.0$ (- - - -), and global works per cycle for the helical fan undergoing pure torsional vibrations about midchord and pure bending vibrations at $\omega = 1$ and $\sigma = \mp 90$ deg ($N_D = \mp 6$).

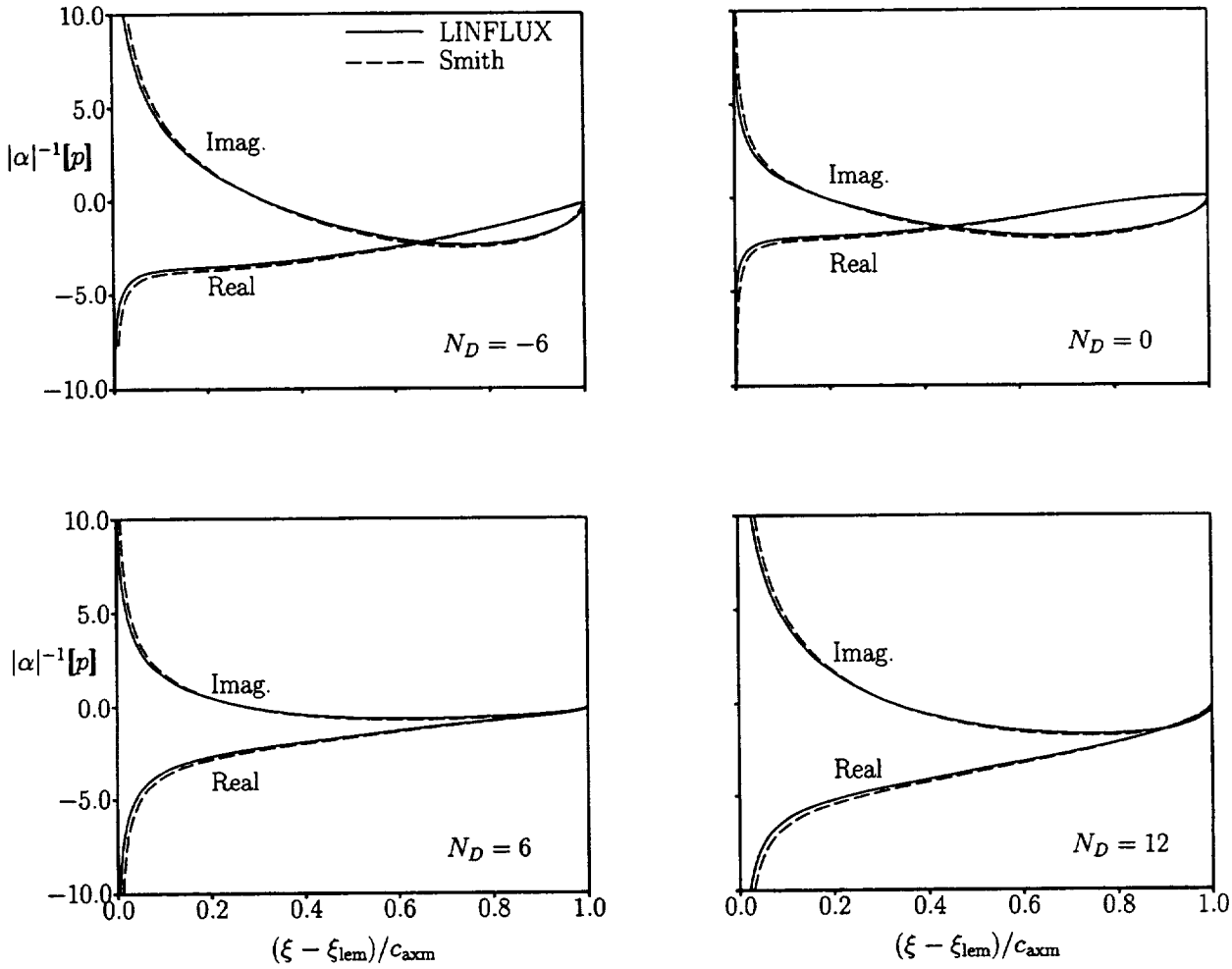

Figure 8: Unsteady pressure difference distributions at midspan ($r/r_D = 0.9$), as predicted using the 3D LINFLUX (——) and the 2D Smith (– – –) analyses, for the helical fan undergoing torsional blade vibrations about midchord at $\omega = 1$.

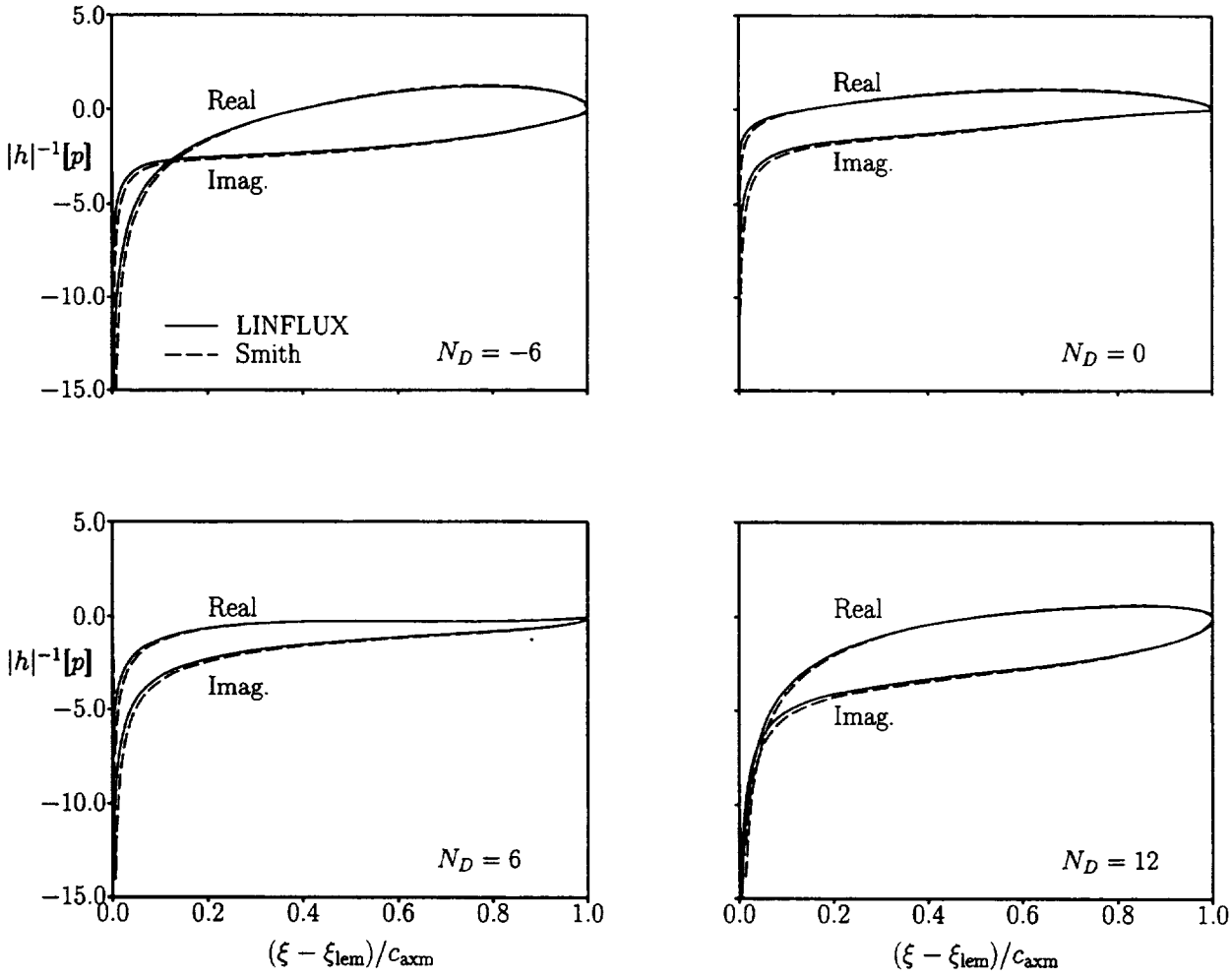

Figure 9: Unsteady pressure difference distributions at midspan ($r/r_D = 0.9$), as predicted using the 3D LINFLUX (——) and the 2D Smith (– – –) analyses, for the helical fan undergoing bending vibrations at $\omega = 1$.

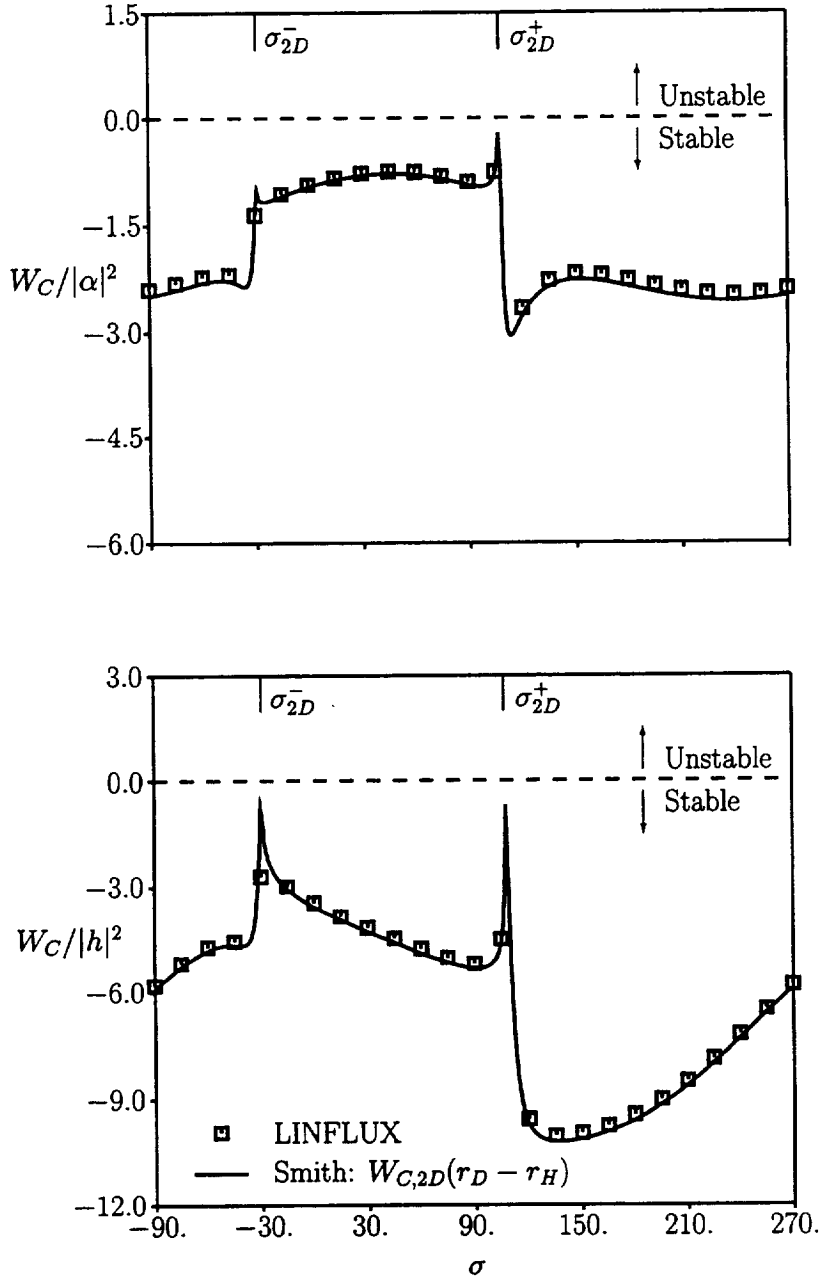

Figure 10: Work per cycle versus interblade phase angle for the helical fan undergoing pure torsional vibrations about midchord (top) and pure bending vibrations (bottom) at $\omega = 1$.

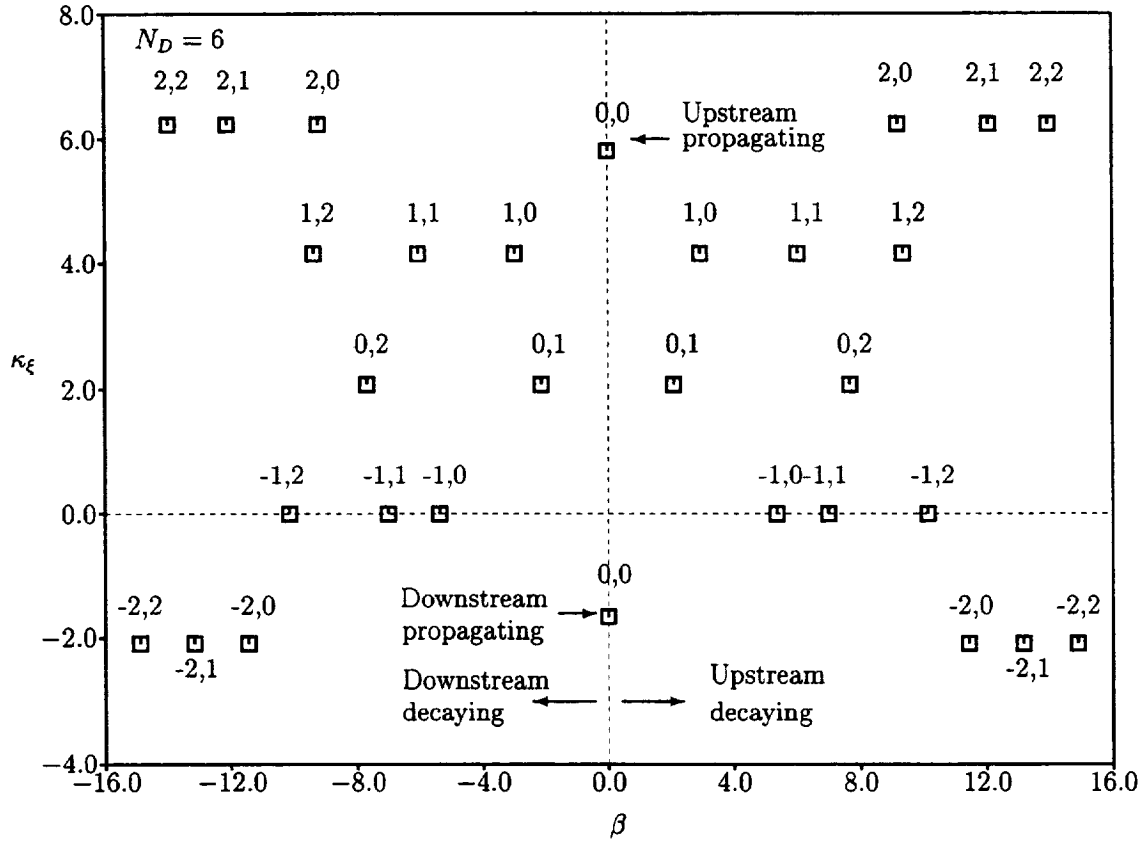

Figure 11: Axial eigenvalues, $\chi = \beta + i\kappa_\xi$, for five circumferential ($m = -2, \ldots, 2$) and three radial ($\mu = 0, 1, 2$) modes of acoustic disturbance, at $\omega = 3.332$ and $N_D = 6$, in the far field of the helical fan.

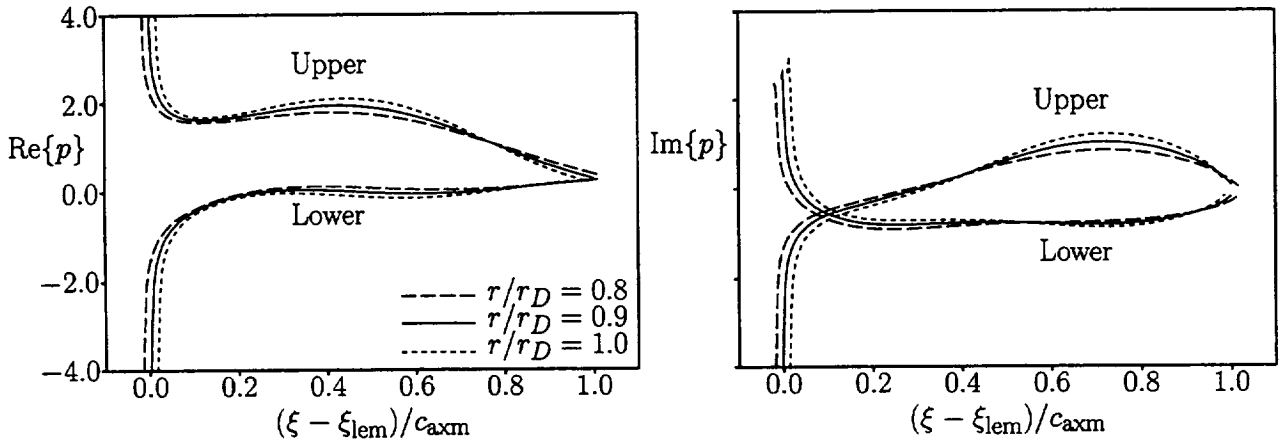

Figure 12: Unsteady surface pressure distributions due to the interaction of an acoustic excitation from upstream $[\bar{p_{A,\text{Ref}}} = (1,0),\ \omega = 3.332$ and $\sigma = 90\,\text{deg}]$ with the helical fan.

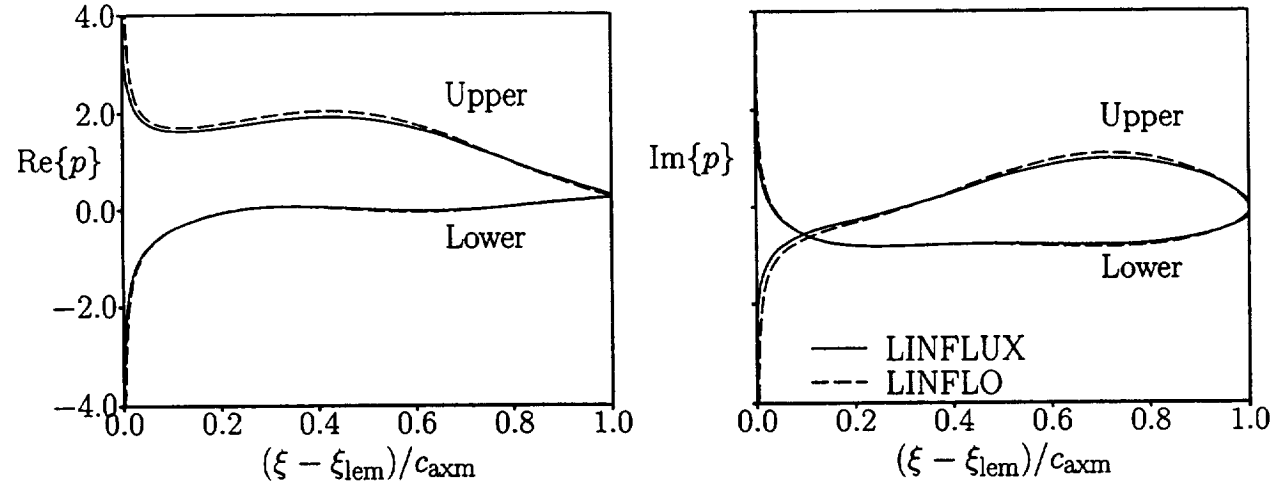

Figure 13: Unsteady surface pressure distributions at midspan ($r/r_\text{D} = 0.9$), as predicted using the 3D LINFLUX (——) , and the 2D LINFLO (– – –) analyses, due to the interaction of an acoustic excitation from upstream $[\bar{p_{A,\text{Ref}}} = (1,0),\ \omega = 3.332,\ \sigma = 90\,\text{deg}]$ with the helical fan.

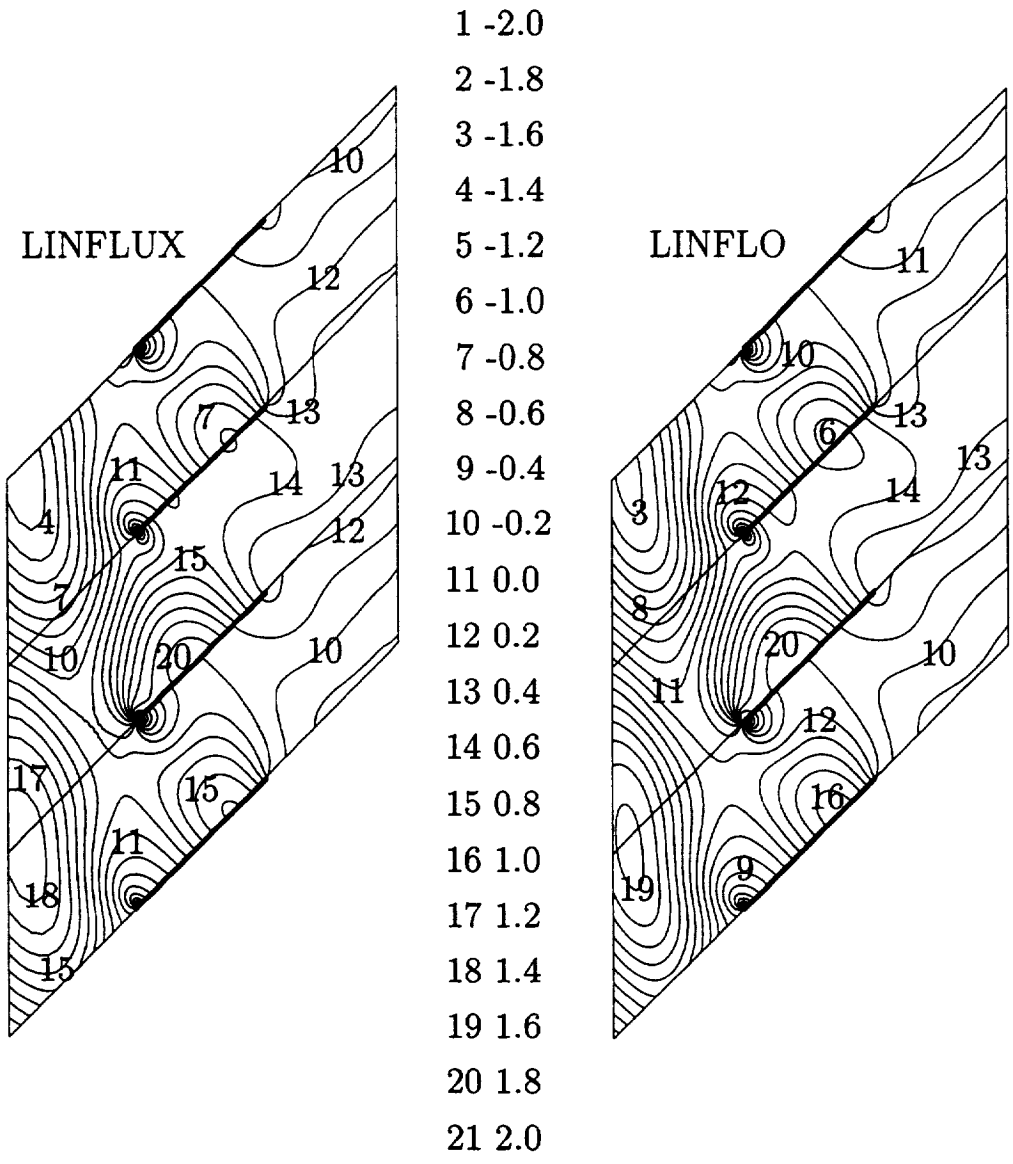

Figure 14: Contours of the in-phase component of the unsteady pressure at midspan due to the interaction of an acoustic excitation from upstream [$p^-_{A,\mathrm{Ref}} = (1, 0)$, $\omega = 3.332$, $\sigma = 90$ deg] with the helical fan.

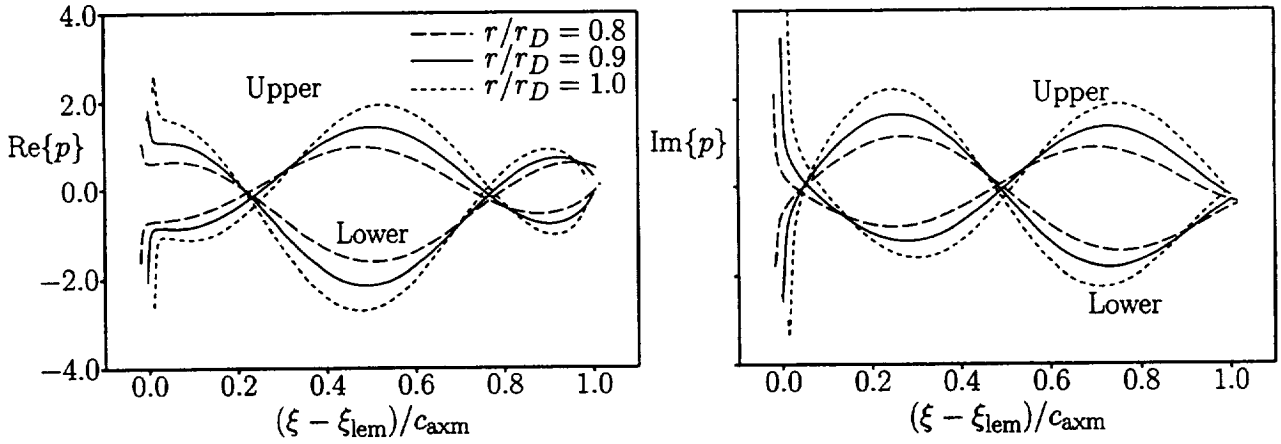

Figure 15: Unsteady surface pressure distributions due to the interaction of an acoustic excitation from downstream [$p^+_{A,\mathrm{Ref}} = (1, 0)$, $\omega = 3.332$ and $\sigma = 90\,\mathrm{deg}$] with the helical fan.

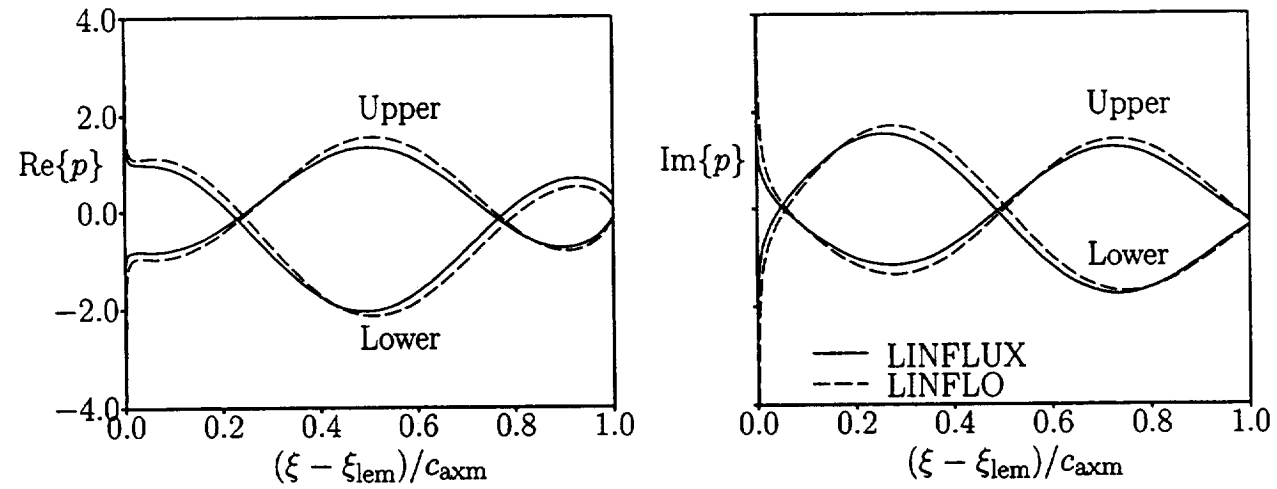

Figure 16: Unsteady surface pressure distributions at midspan ($r/r_D = 0.9$) due to the interaction of an acoustic excitation from downstream [$p^+_{A,\mathrm{Ref}} = (1, 0)$, $\omega = 3.332$, $\sigma = 90\,\mathrm{deg}$] with the helical fan.

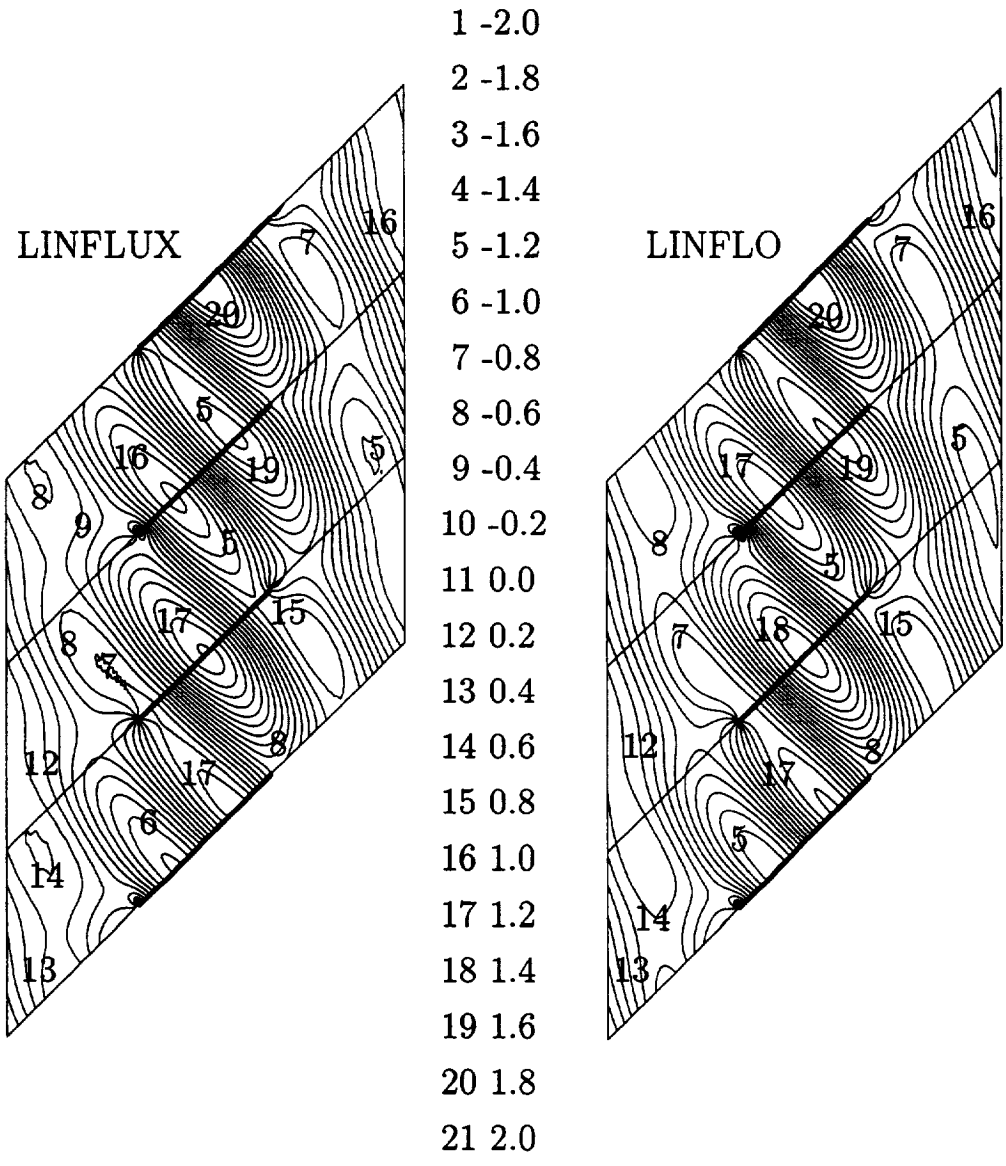

Figure 17: Contours of the in-phase component of the unsteady pressure at midspan due to the interaction of an acoustic excitation from downstream [$p^{+}_{A,\mathrm{Ref}} = (1, 0)$, $\omega = 3.332$, $\sigma = 90\,\mathrm{deg}$] with the helical fan.

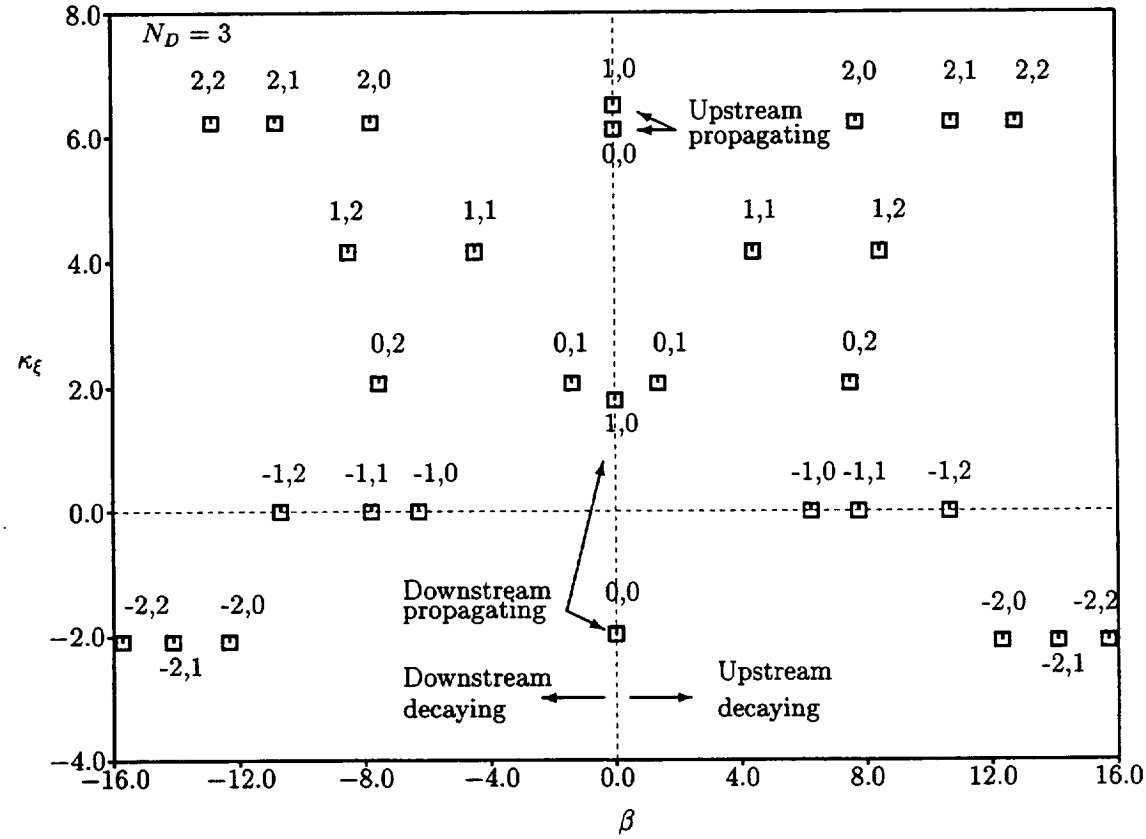

Figure 18: Axial eigenvalues, $\chi = \beta + i\kappa_\xi$, for three circumferential ($m = -1, 0, 1$) and three radial ($\mu = 0, 1, 2$) modes of acoustic disturbance in the far field of the helical fan, for an unsteady flow at $\omega = 3.887$ and $N_D = 3$.

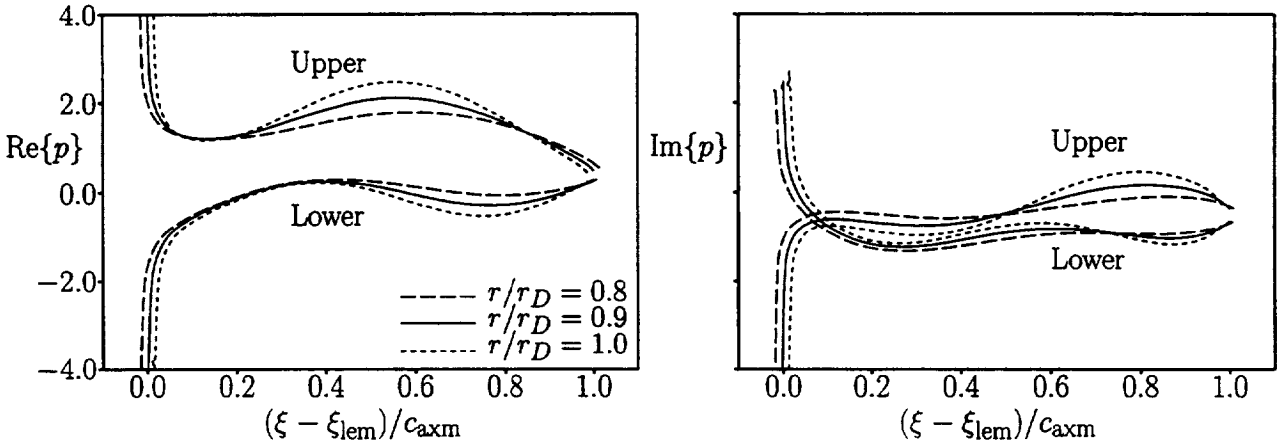

Figure 19: Unsteady surface pressure distributions at $r/r_D = 0.8$ (– – –), $r/r_D = 0.9$ (——) and $r/r_D = 1.0$ (- - - -), due to the interaction of an acoustic excitation from upstream [$\bar{p_{A,\text{Ref}}} = (1, 0)$, $\omega = 3.887$ and $\sigma = 45\,\text{deg}$], with the helical fan.

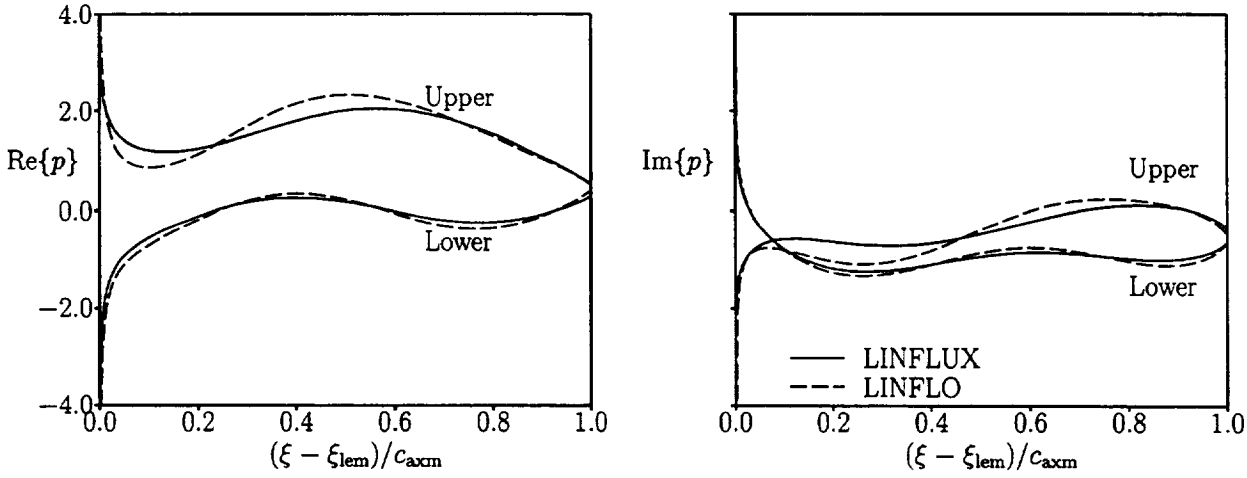

Figure 20: Unsteady surface pressure distributions at midspan ($r/r_D = 0.9$) due to the interaction of an acoustic excitation from upstream [$\bar{p_{A,\text{Ref}}} = (1, 0)$, $\omega = 3.887$ and $\sigma = 45\,\text{deg}$], with the helical fan.

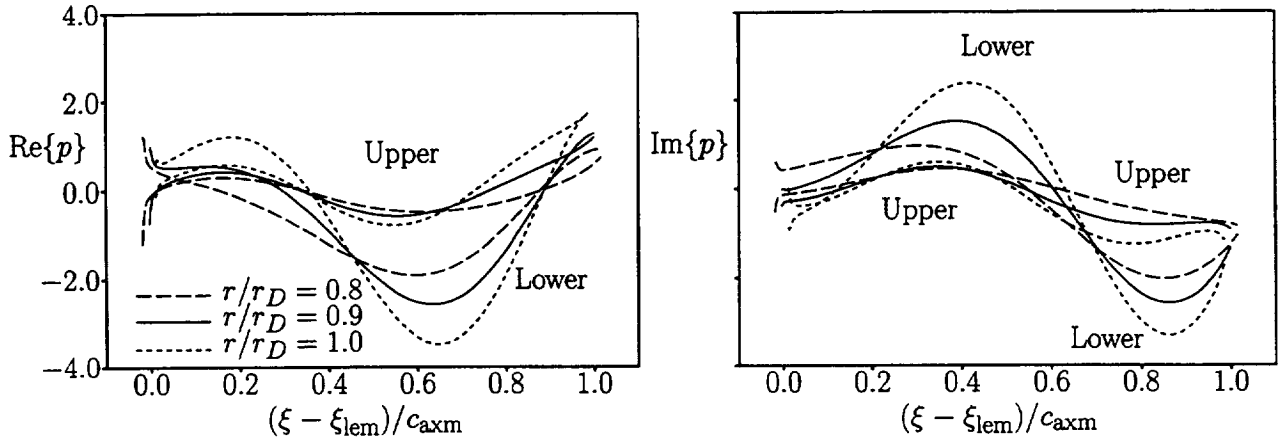

Figure 21: Unsteady surface pressure distributions at $r/r_D = 0.8$ (– – –), $r/r_D = 0.9$ (——) and $r/r_D = 1.0$ (- - - -), due to the interaction of an acoustic excitation from downstream [$p^+_{A,\mathrm{Ref}} = (1, 0)$, $\omega = 3.887$ and $\sigma = 45\,\mathrm{deg}$], with the helical fan.

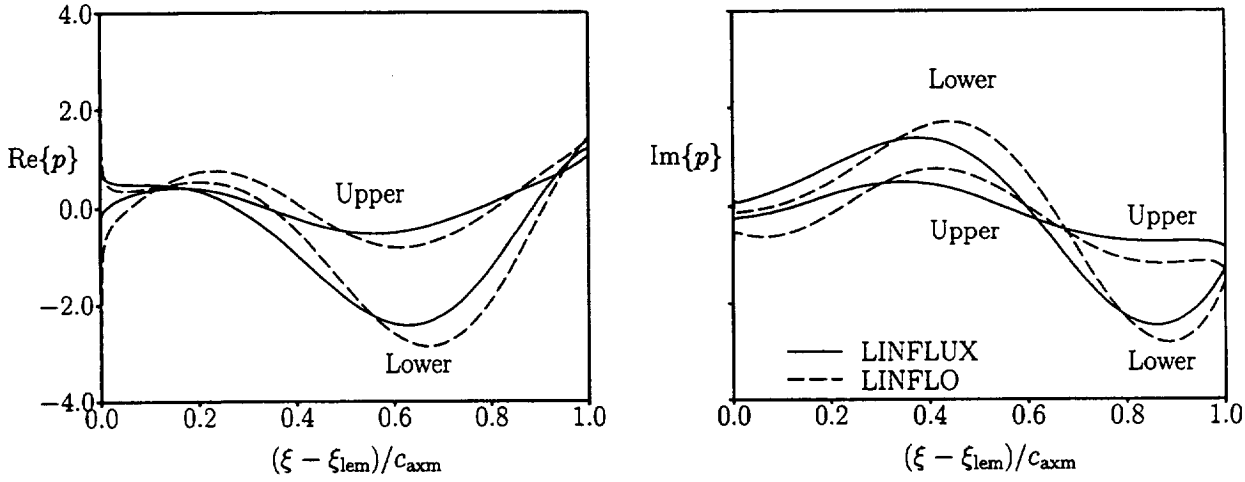

Figure 22: Unsteady surface pressure distributions at midspan ($r/r_D = 0.9$) due to the interaction of an acoustic excitation from downstream [$p^{\mp}_{A,\mathrm{Ref}} = (1, 0)$, $\omega = 3.887$ and $\sigma = 45\,\mathrm{deg}$], with the helical fan.

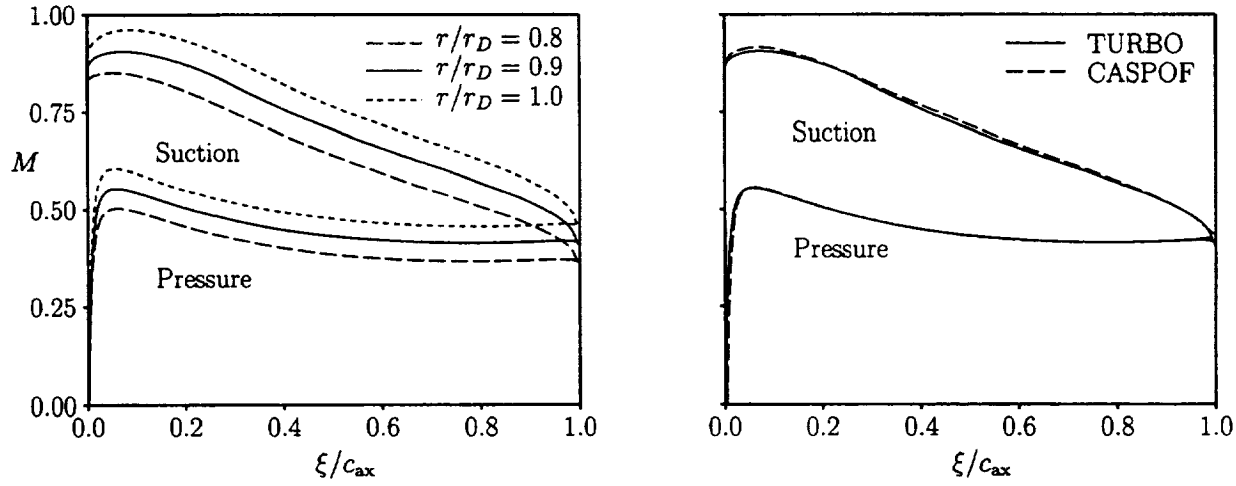

Figure 23: Relative surface Mach number distributions for the 3D 10th Standard Cascade ($M^{abs}_{-\infty} = 0.4015$, $|\Omega| = 0.2145$): (a) TURBO predictions; (b) TURBO and CASPOF predictions at midspan, $r/r_D = 0.9$.

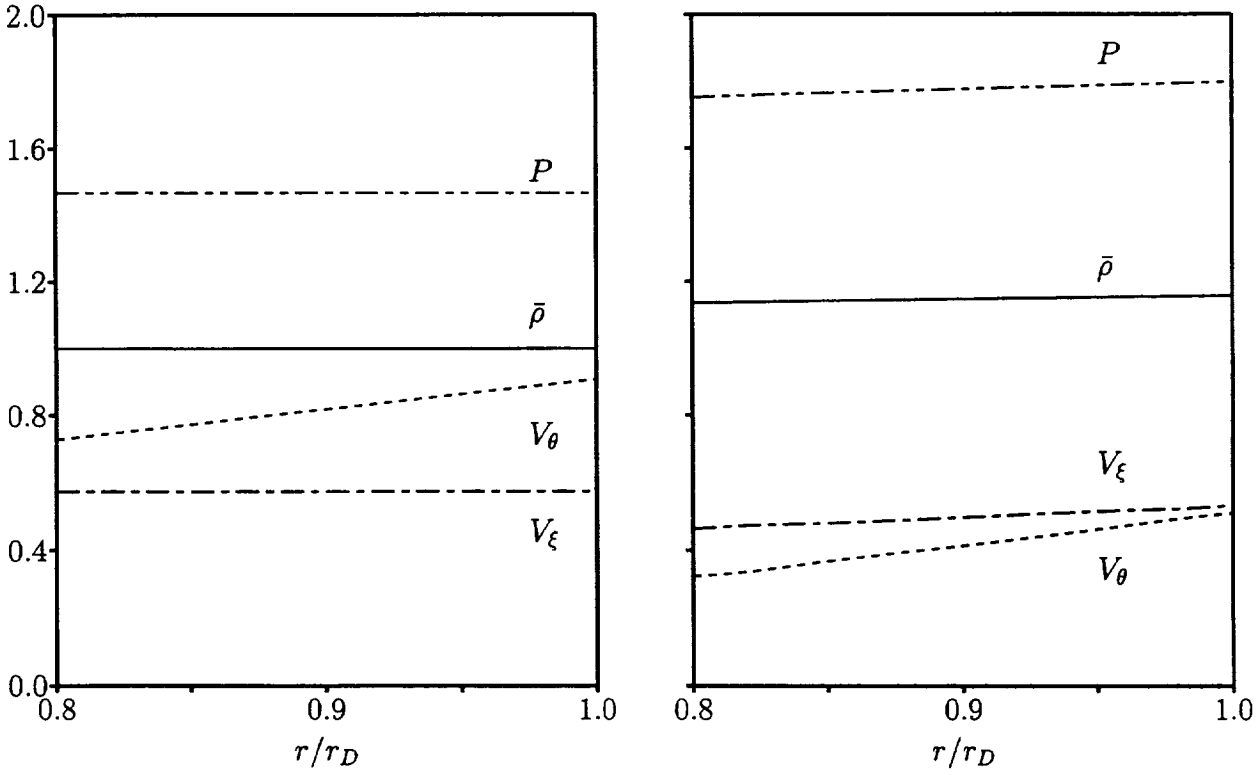

Figure 24: Relative frame steady flow properties far upstream and far downstream of the 3D 10th Standard Cascade ($M^{abs}_{-\infty} = 0.4015$, $|\Omega| = 0.2145$).

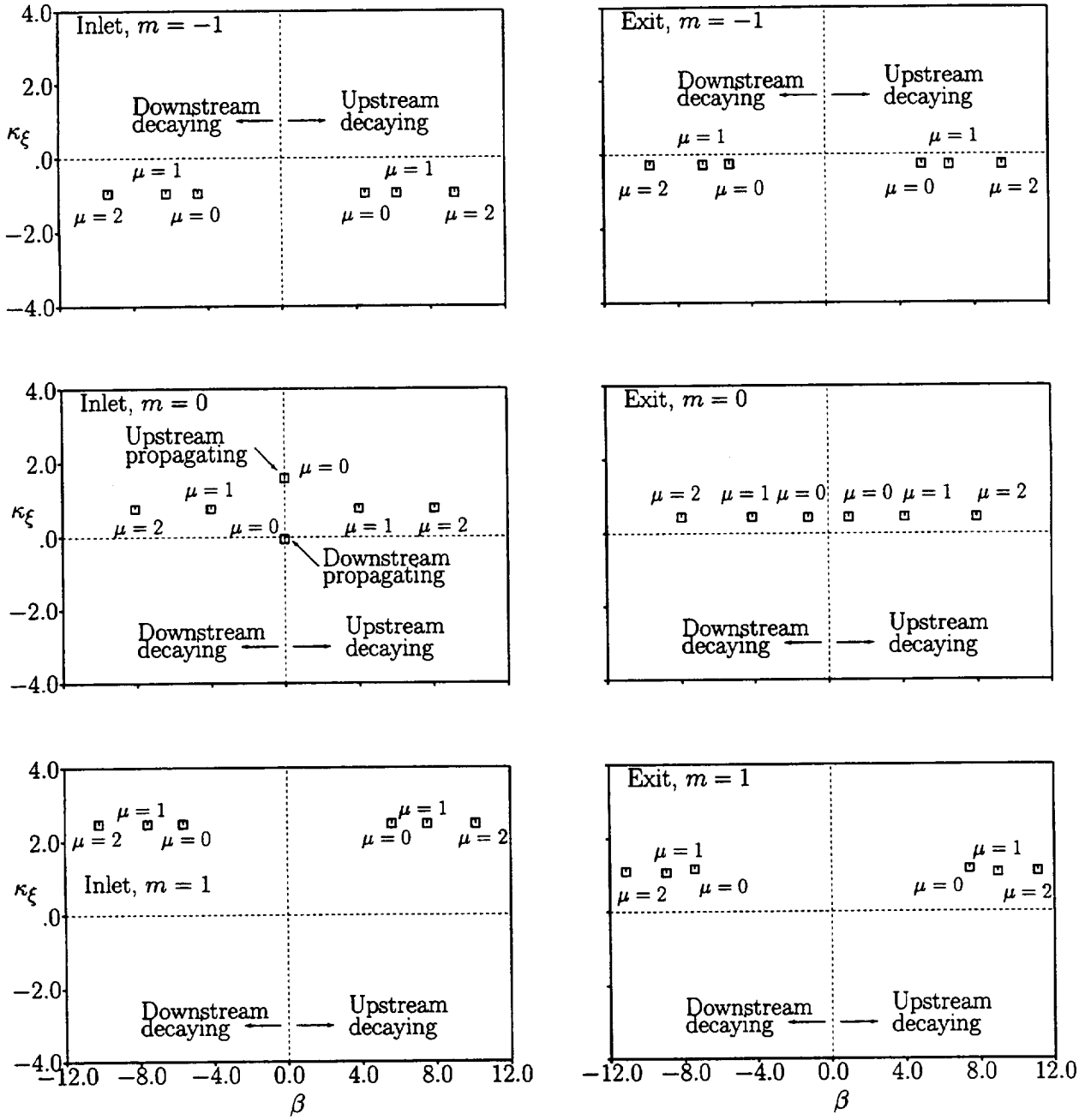

Figure 25: Axial eigenvalues, $\chi = \beta + i\kappa_\xi$, for three circumferential ($m = -1, 0, 1$) and three radial ($\mu = 0, 1, 2$) modes of acoustic disturbance far upstream and far downstream of the 3D 10th Standard Cascade, for an unsteady flow at $\omega = 1.0$ and $N_D = 6$.

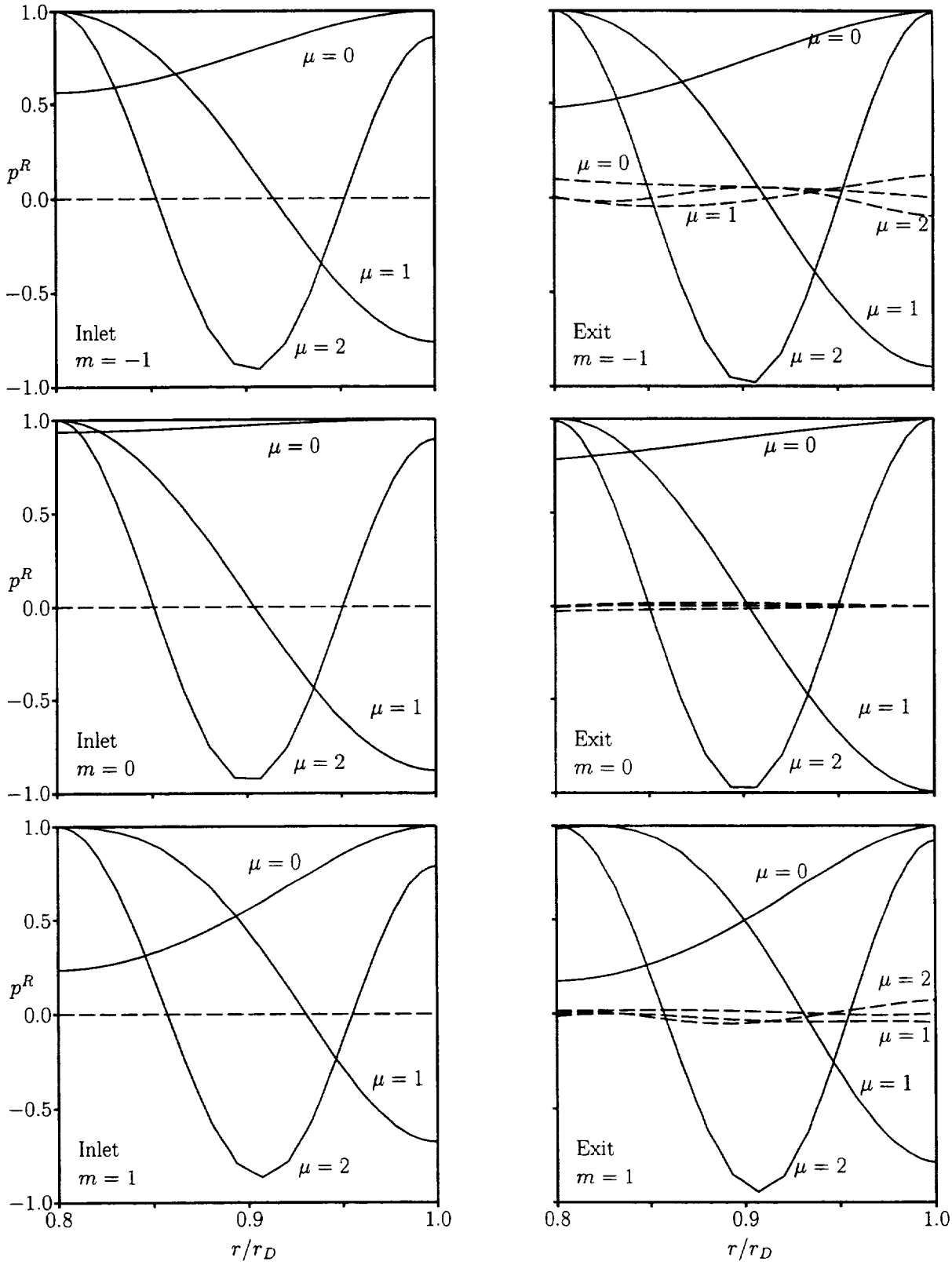

Figure 26: Radial pressure modes, $p^R_{m\mu}(r)$, $m = -1, 0, 1$, $\mu = 0, 1, 2$, for an acoustic excitation or response at $N_D = 6$ far upstream and for an acoustic response at $N_D = 6$ far downstream of the 3D 10th Standard Cascade: (——) in-phase (real) component of $p^R_{m\mu}$; (− − −) out-of-phase (imaginary) component of $p^R_{m\mu}$.

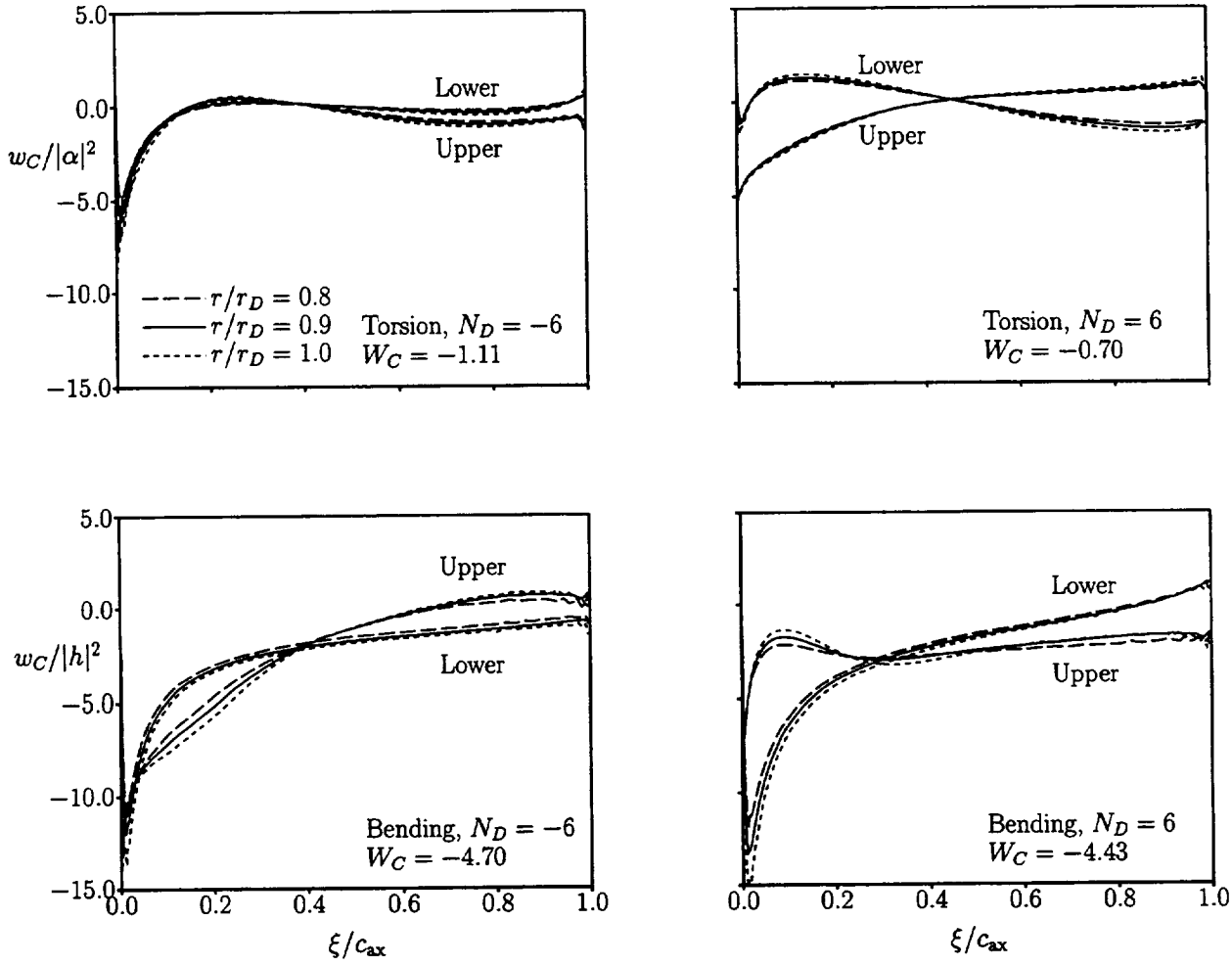

Figure 27: Local work per cycle distributions at $r/r_D = 0.8$ (− − −), $r/r_D = 0.9$ (——) and $r/r_D = 1.0$ (- - - -), and global works per cycle for the 3D 10th Standard Cascade undergoing pure torsional vibrations about midchord and pure bending vibrations, at $\omega = 1$ and $\sigma = \mp 90$ deg ($N_D = \mp 6$).

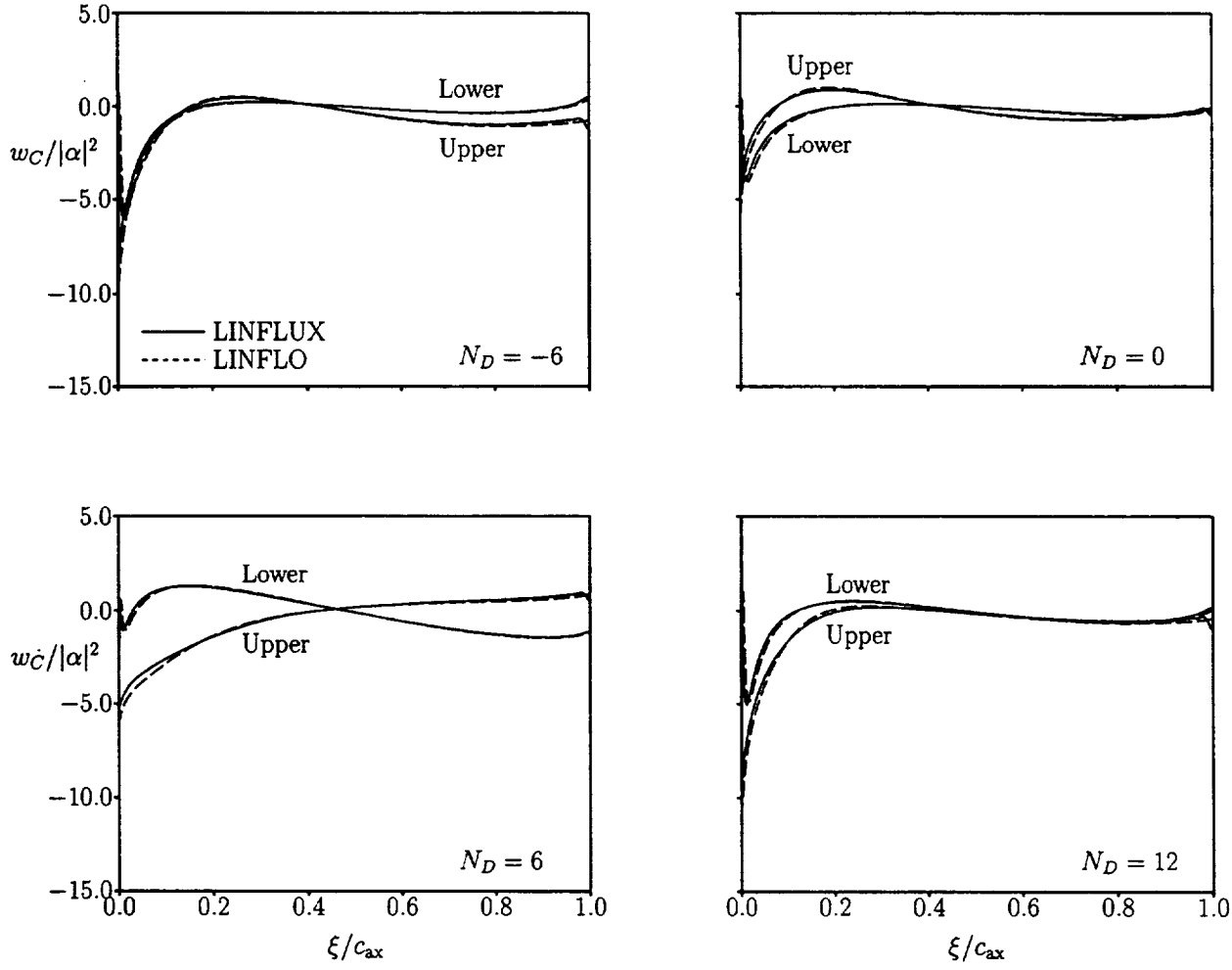

Figure 28: Local work per cycle distributions at midspan, as predicted using the 3D LINFLUX (——) and the 2D LINFLO (– – –) analyses, for the 3D 10th Standard Cascade undergoing torsional blade vibrations about midchord at $\omega = 1$.

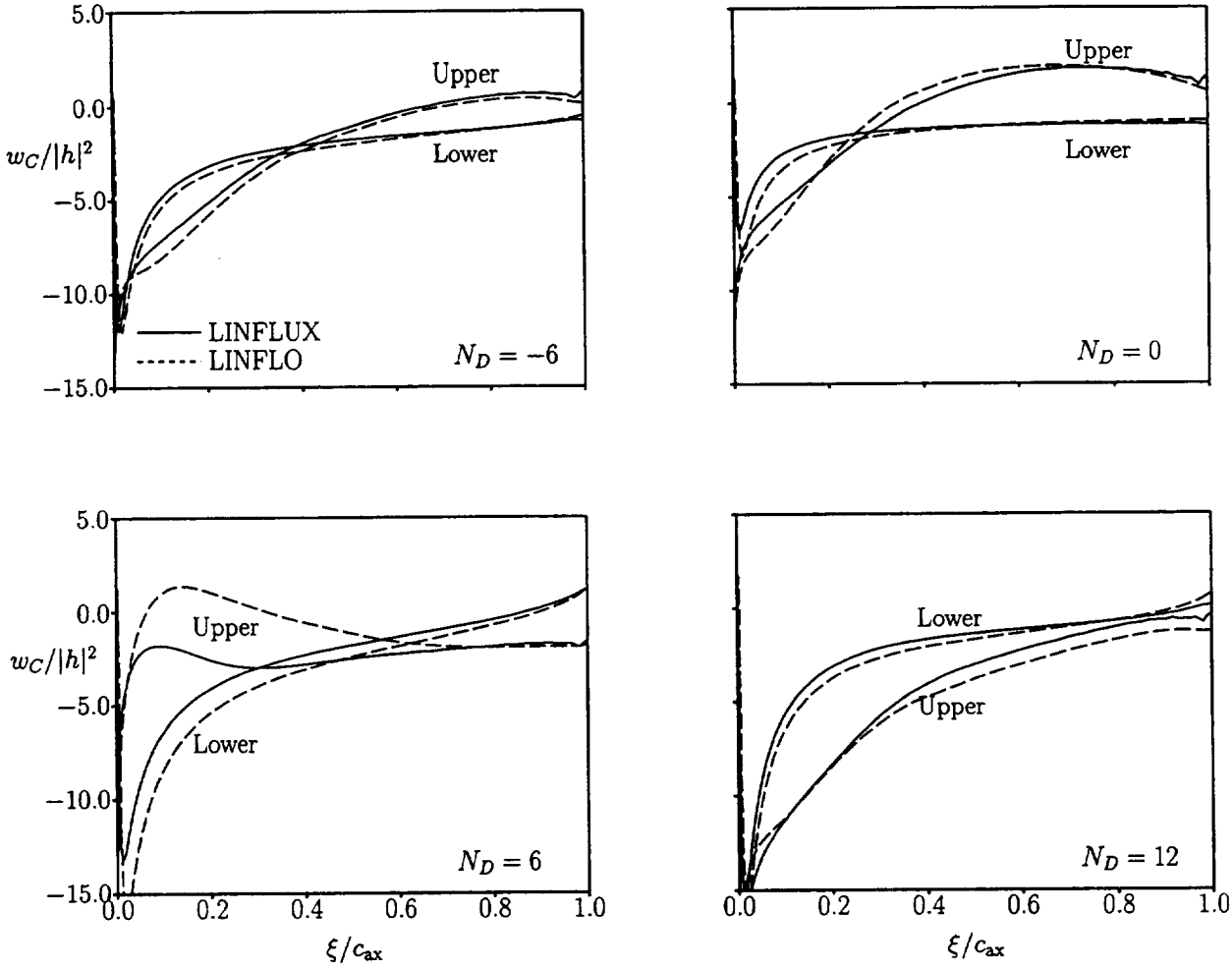

Figure 29: Local work per cycle distributions at midspan, as predicted using the 3D LINFLUX (——) and the 2D LINFLO (– – –) analyses, for the 3D 10th Standard Cascade undergoing bending vibrations at $\omega = 1$.

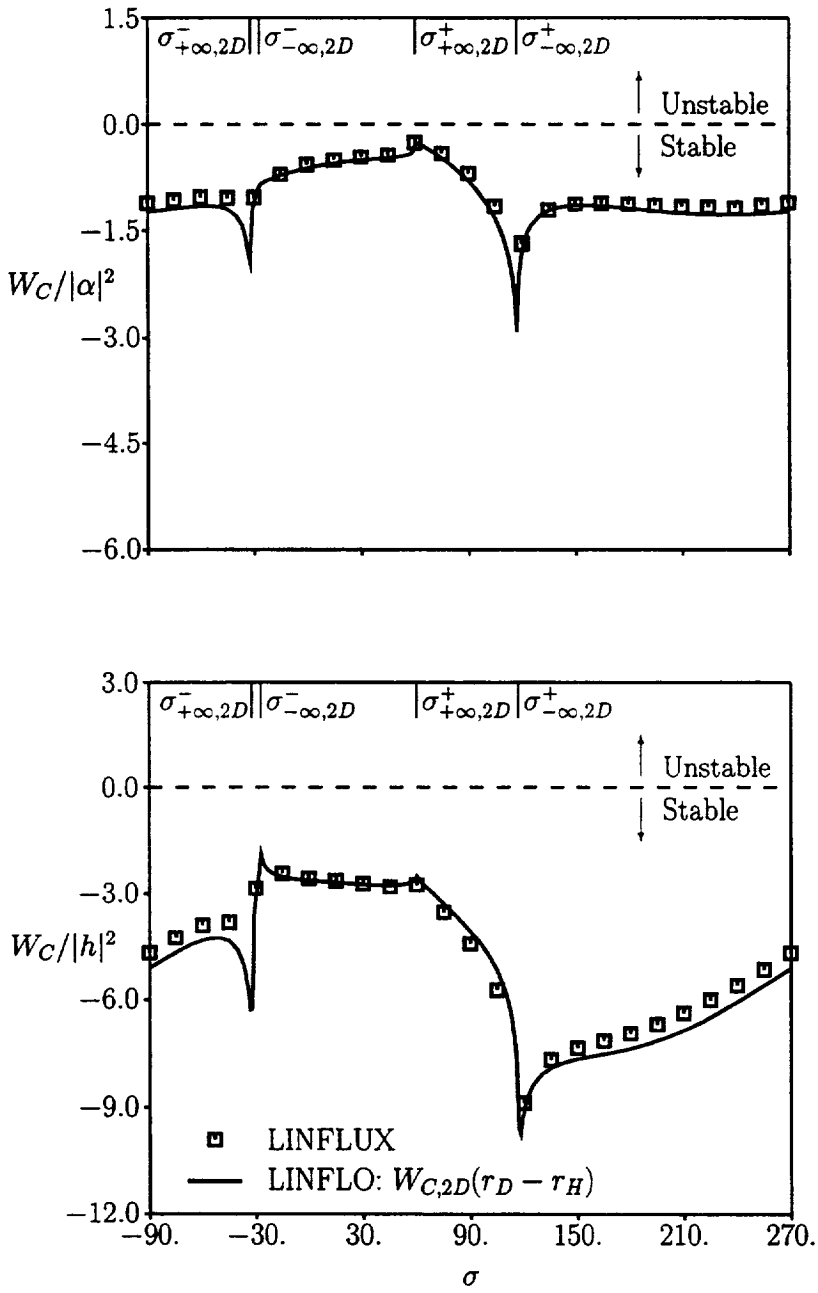

Figure 30: Work per cycle versus interblade phase angle for the 3D 10th Standard Cascade undergoing pure torsional vibrations about midchord (top) and pure bending vibrations (bottom) at $\omega = 1$.

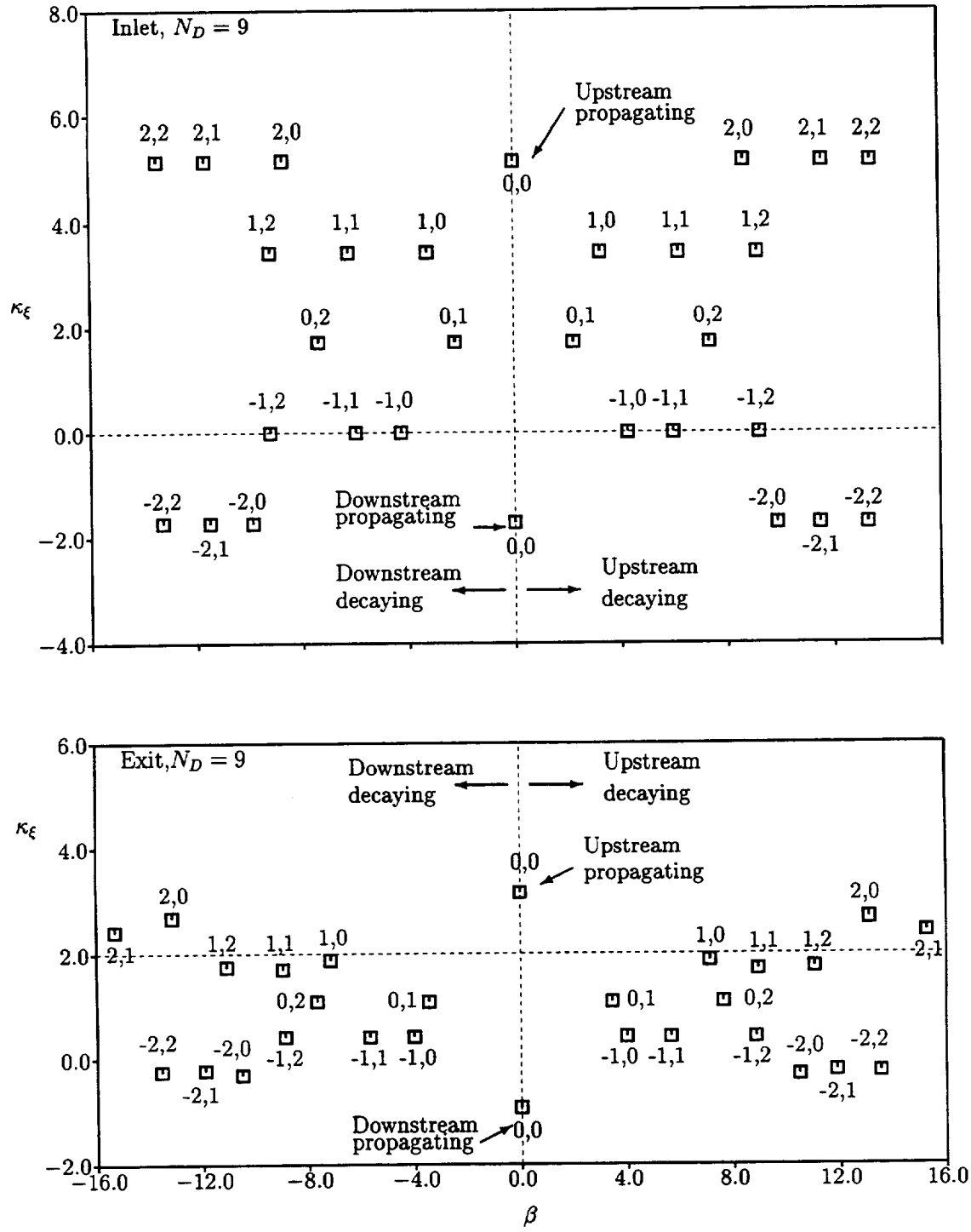

Figure 31: Axial eigenvalues, $\chi = \beta + i\kappa_\xi$, for five circumferential ($m = -2, \ldots, 2$) and three radial ($\mu = 0, 1, 2$) modes of acoustic disturbance far upstream and far downstream of the 3D 10th Standard Cascade, for unsteady flow at $\omega = 3.218$ and $N_D = 9$.

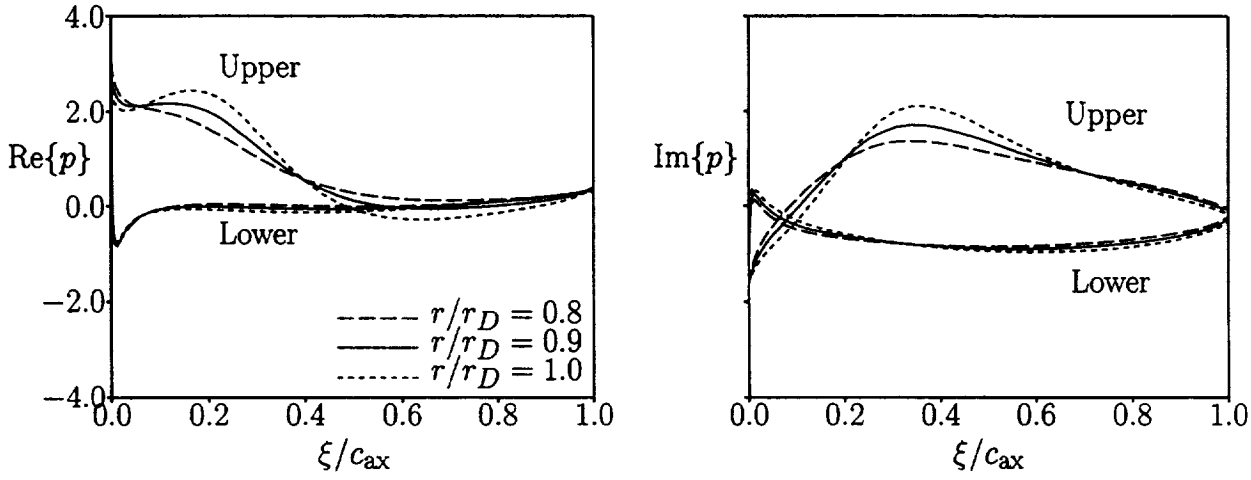

Figure 32: Unsteady surface pressure distributions due to the interaction of an acoustic excitation from upstream [$\bar{p}^{-}_{A,\mathrm{Ref}} = (1, 0)$, $\omega = 3.218$ and $\sigma = 135\,\mathrm{deg}$] with the 3D 10th Standard Cascade.

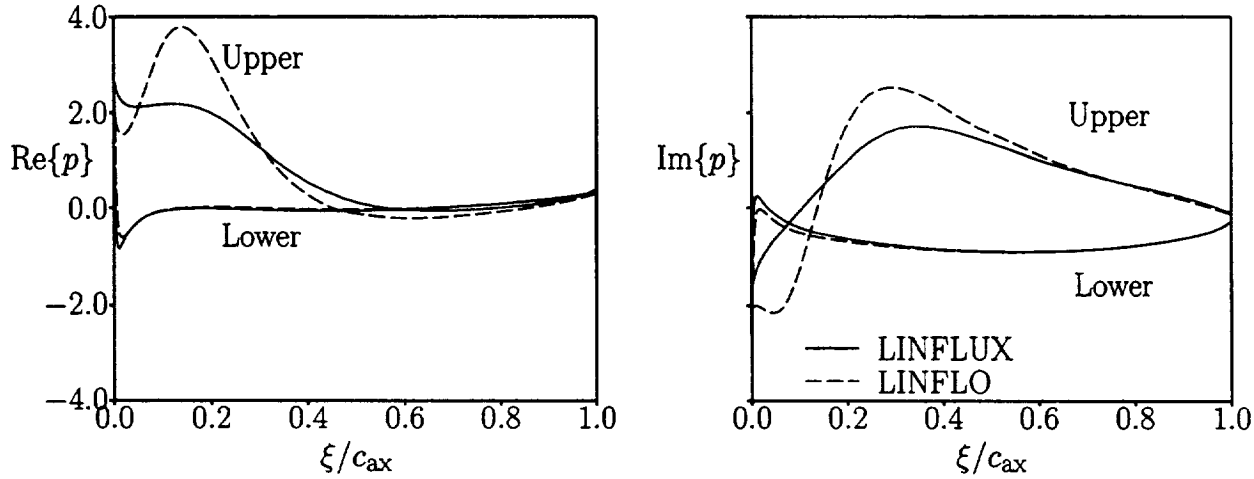

Figure 33: Unsteady surface pressure distributions at midspan ($r/r_D = 0.9$) due to the interaction of an acoustic excitation from upstream [$\bar{p}^{-}_{A,\mathrm{Ref}} = (1, 0)$, $\omega = 3.218$, $\sigma = 135\,\mathrm{deg}$] with the 3D 10th Standard Cascade.

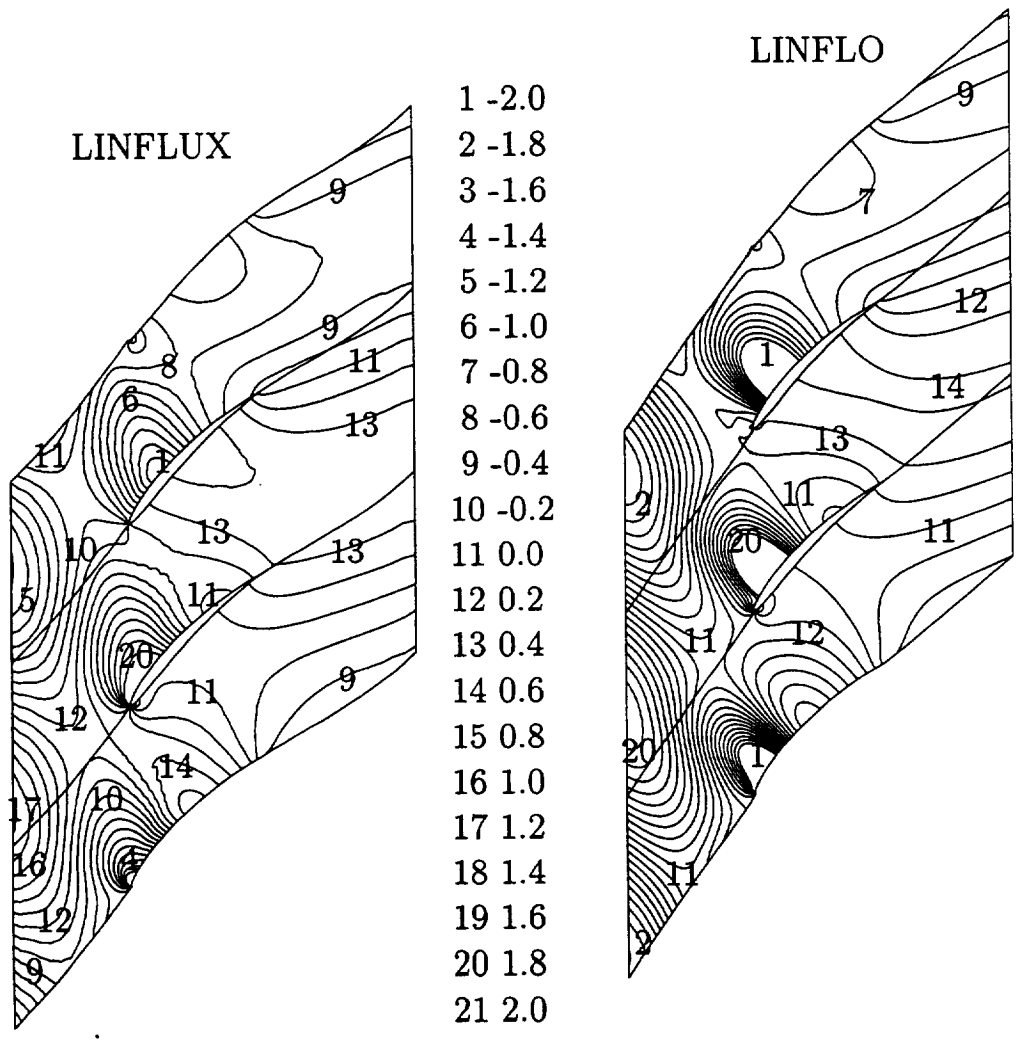

Figure 34: Contours of the in-phase component of the unsteady pressure at midspan due to the interaction of an acoustic excitation from upstream [$\bar{p_{A,\mathrm{Ref}}} = (1,0)$, $\omega = 3.218$, $\sigma =$ 135 deg] with the 3D 10th Standard Cascade.

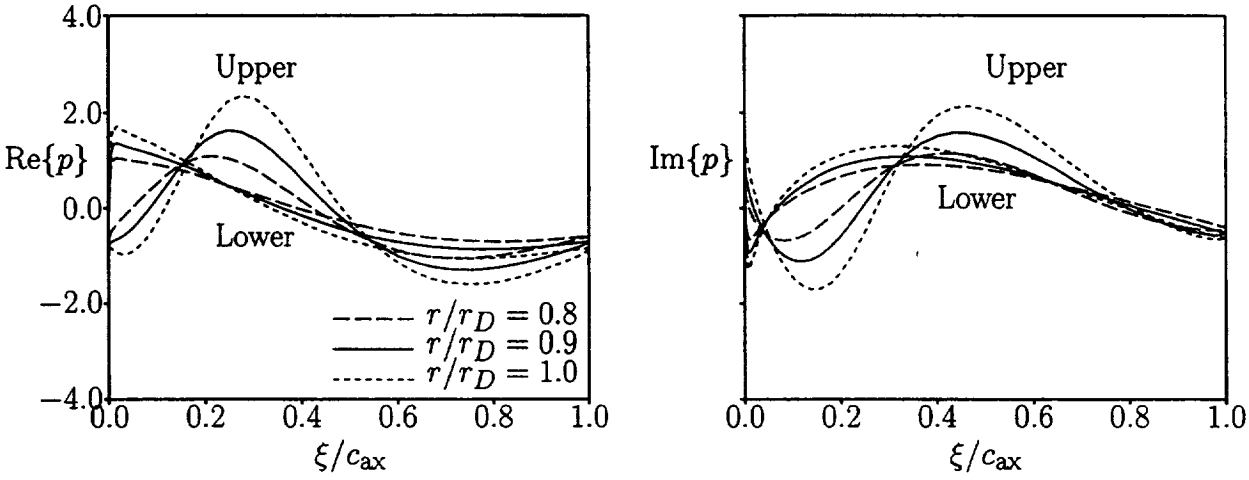

Figure 35: Unsteady surface pressure distributions due to the interaction of an acoustic excitation from downstream [$p^+_{A,\mathrm{Ref}} = (1,0)$, $\omega = 3.218$ and $\sigma = 135\,\mathrm{deg}$] with the 3D 10th Standard Cascade.

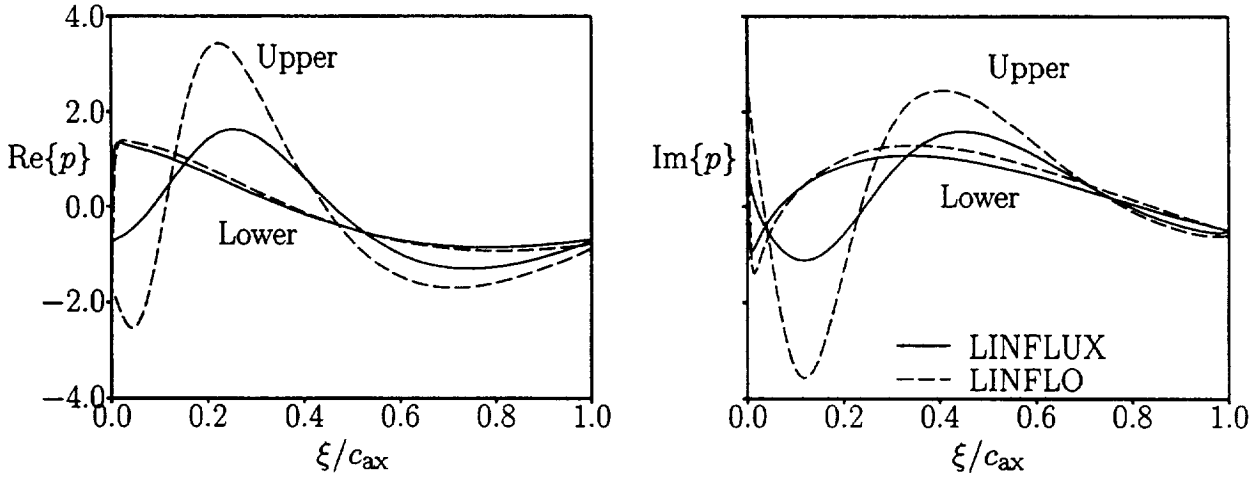

Figure 36: Unsteady surface pressure distributions at midspan due to the interaction of an acoustic excitation from downstream [$p^+_{A,\mathrm{Ref}} = (1,0)$, $\omega = 3.218$, $\sigma = 135\,\mathrm{deg}$] with the 3D 10th Standard Cascade.

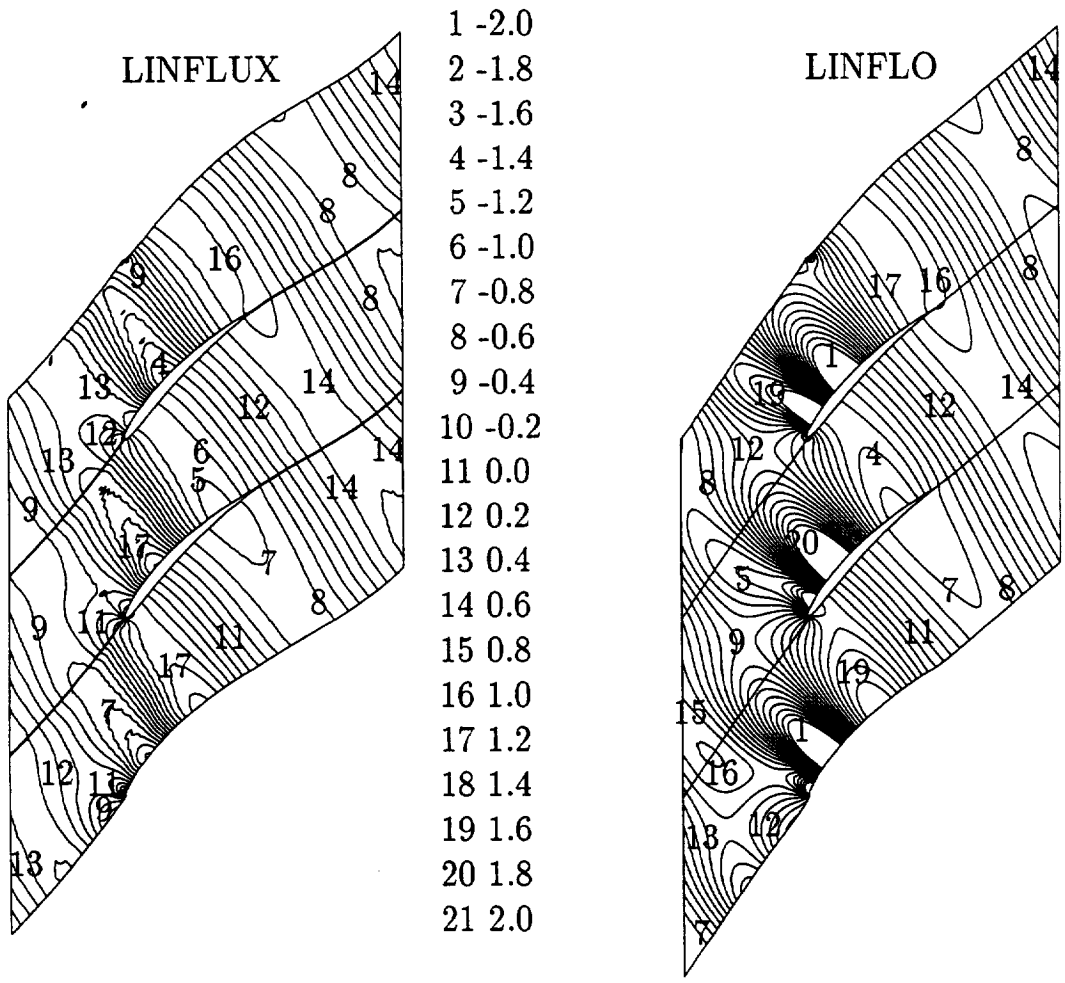

Figure 37: Contours of the in-phase component of the unsteady pressure at midspan due to the interaction of an acoustic excitation from downstream [$p^{+}_{A,\mathrm{Ref}} = (1, 0)$, $\omega = 3.218$, $\sigma = 135\,\mathrm{deg}$] with the 3D 10th Standard Cascade.

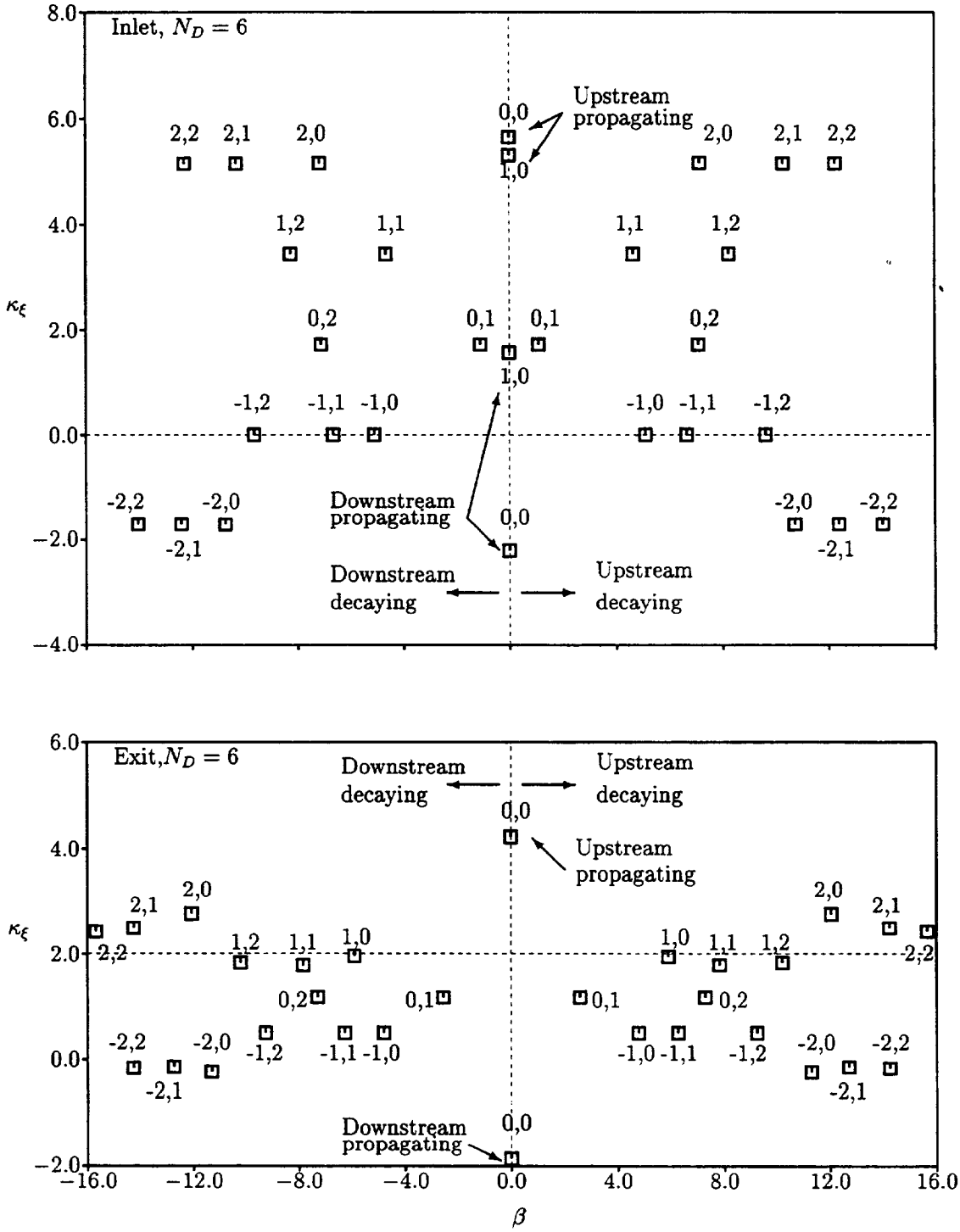

Figure 38: Axial eigenvalues, $\chi = \beta + i\kappa_\xi$, for five circumferential ($m = -2, \ldots, 2$) and three radial ($\mu = 0, 1, 2$) modes of acoustic disturbance far upstream and far downstream of the 3D 10th Standard Cascade, for an unsteady flow at $\omega = 3.861$ and $N_D = 6$.

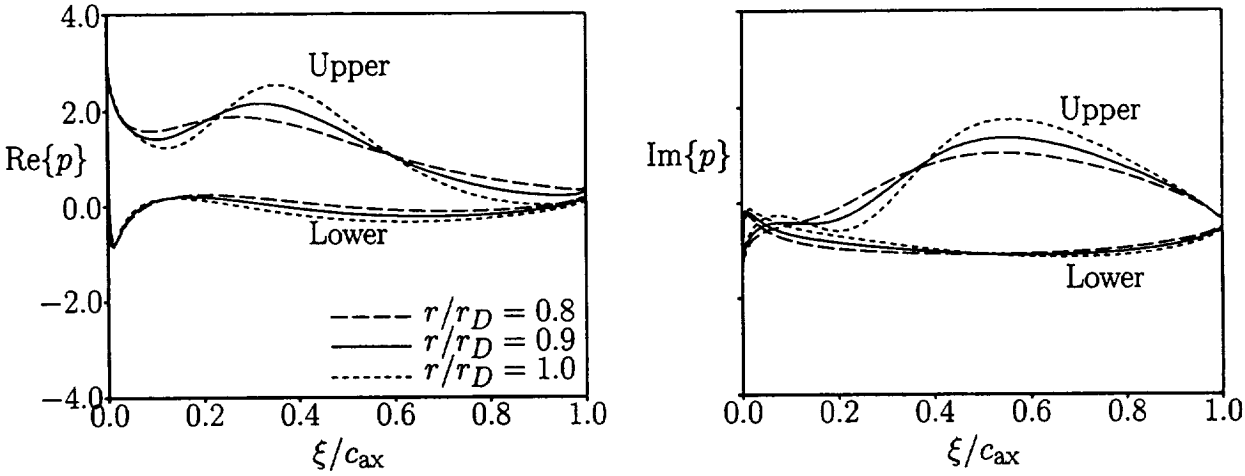

Figure 39: Unsteady surface pressure distributions due to the interaction of an acoustic excitation from upstream [$p^-_{A,\mathrm{Ref}} = (1,0)$, $\omega = 3.861$ and $\sigma = 90\,\mathrm{deg}$] with the 3D 10th Standard Cascade.

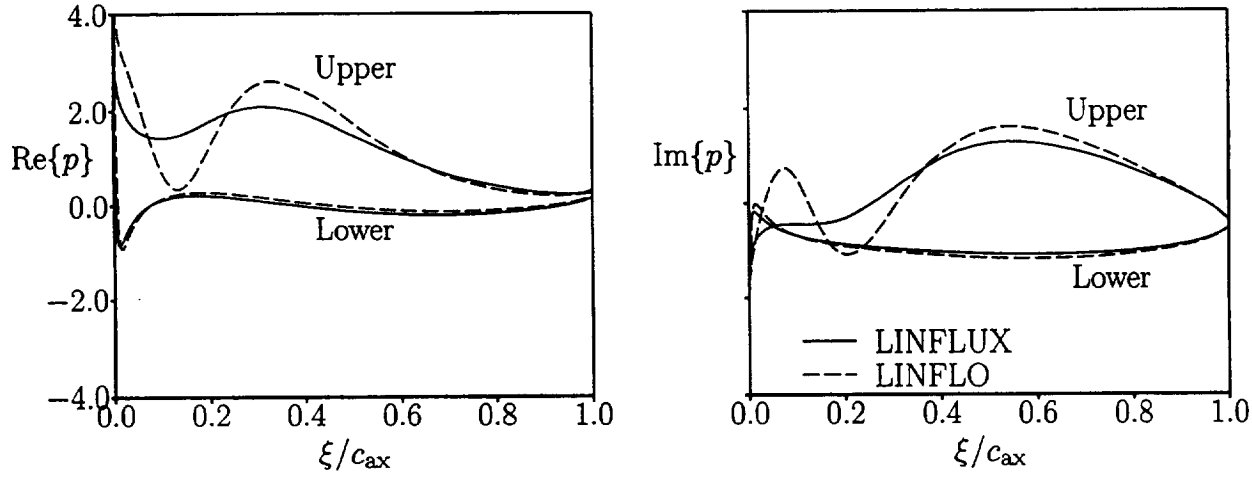

Figure 40: Unsteady surface pressure distributions at midspan ($r/r_D = 0.9$) due to the interaction of an acoustic excitation from upstream [$p^-_{A,\mathrm{Ref}} = (1,0)$, $\omega = 3.861$ and $\sigma = 90\,\mathrm{deg}$] with the 3D 10th Standard Cascade.

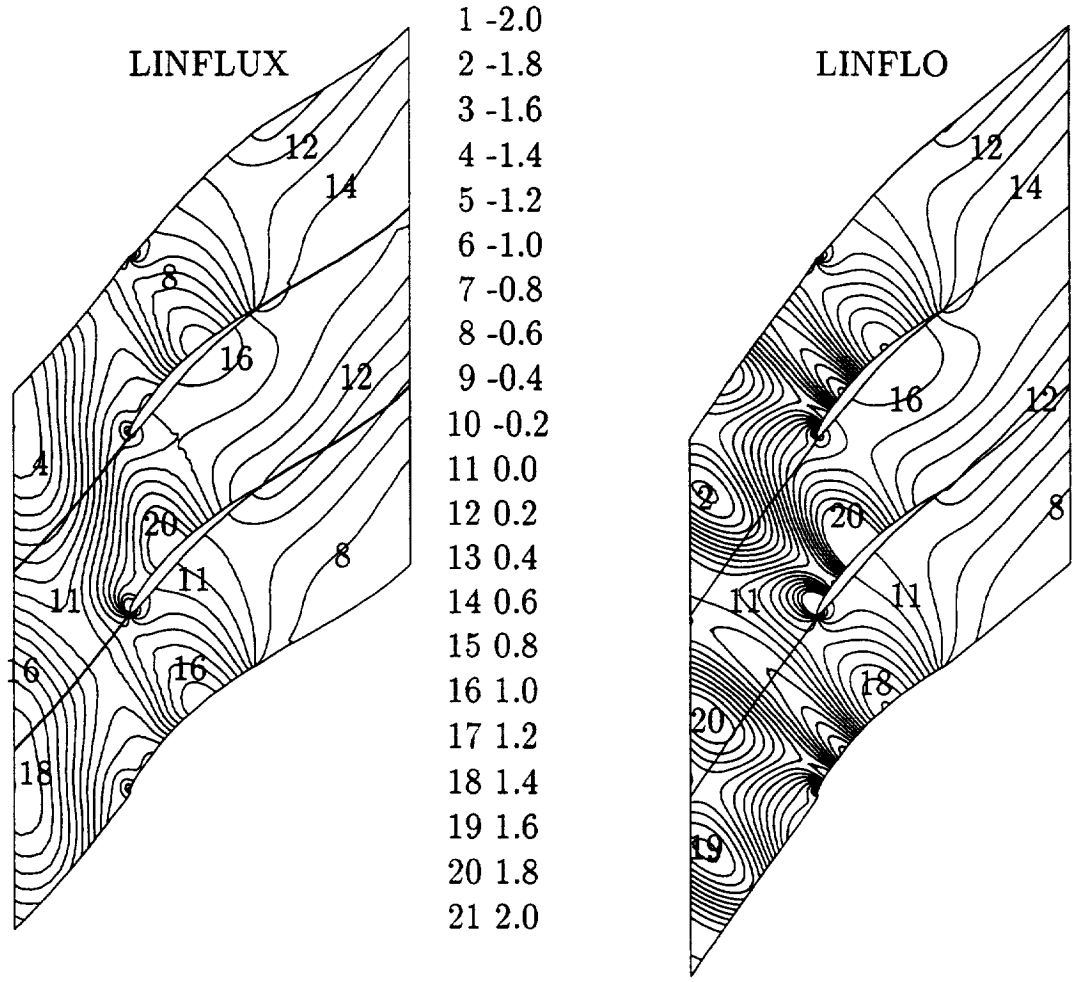

Figure 41: Contours of the in-phase component of the unsteady pressure at midspan due to the interaction of an acoustic excitation from upstream [$p^-_{A,\mathrm{Ref}} = (1,0)$, $\omega = 3.861$, $\sigma = 90\,\mathrm{deg}$] with the 3D 10th Standard Cascade.

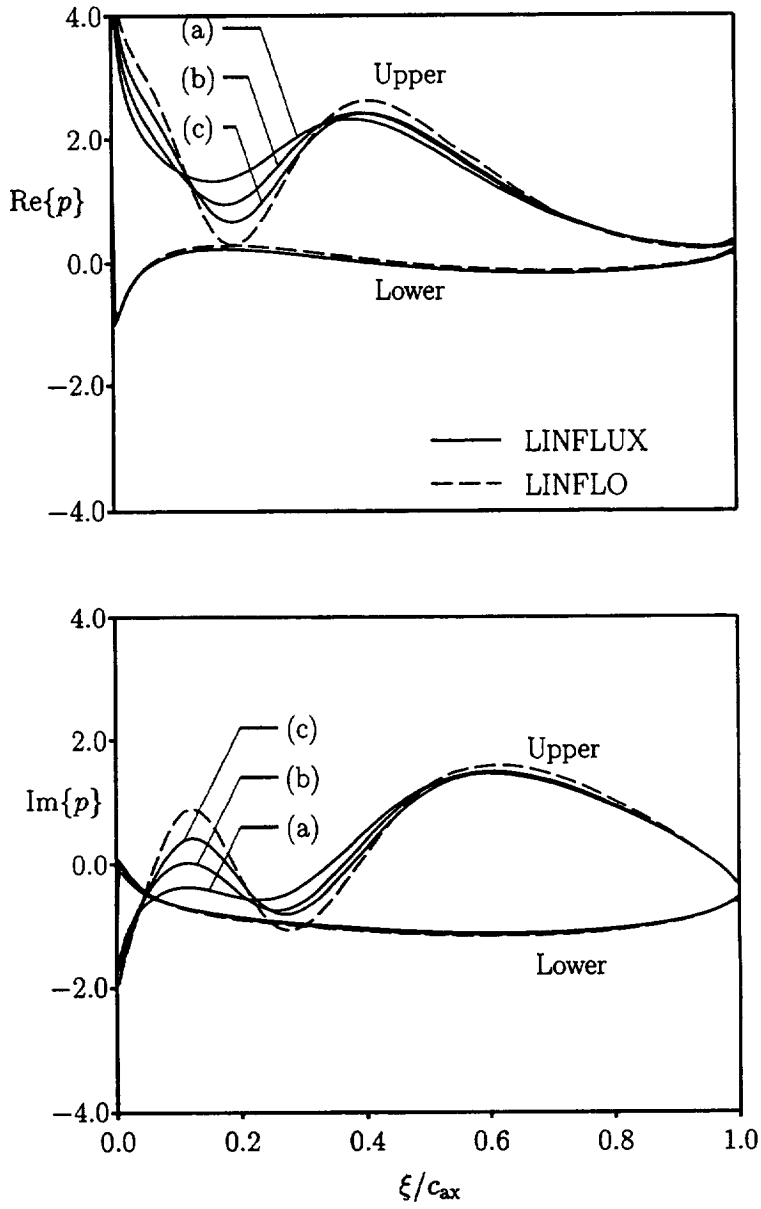

Figure 42: Unsteady surface pressure distributions, as predicted by the 2D LINFLUX and LINFLO analyses, due to the interaction of an acoustic excitation from upstream [$\bar{p_A} = (1, 0)$, $\omega = 3.861$, $\sigma = 90$ deg] with the 2D 10th Standard Cascade. The LINFLUX solutions were determined on 141 × 41 (a), 211 × 61 (b), and 281 × 81 (c) H-meshes.

REPORT DOCUMENTATION PAGE

Form Approved
OMB No. 0704-0188

1. AGENCY USE ONLY (*Leave blank*)	2. REPORT DATE	3. REPORT TYPE AND DATES COVERED
	March 1997	Final Contractor Report

4. TITLE AND SUBTITLE

A Three-Dimensional Linearized Unsteady Euler Analysis for Turbomachinery Blade Rows

5. FUNDING NUMBERS

WU-538-03-11
C-NAS3-26618

6. AUTHOR(S)

Matthew D. Montgomery and Joseph M. Verdon

7. PERFORMING ORGANIZATION NAME(S) AND ADDRESS(ES)

United Technologies Research Center
411 Silver Lane
East Hartford, Connecticut 06108-1049

8. PERFORMING ORGANIZATION REPORT NUMBER

E-10670

9. SPONSORING/MONITORING AGENCY NAME(S) AND ADDRESS(ES)

National Aeronautics and Space Administration
Lewis Research Center
Cleveland, Ohio 44135-3191

10. SPONSORING/MONITORING AGENCY REPORT NUMBER

NASA CR-4770

11. SUPPLEMENTARY NOTES

Project Manager, Dennis L. Huff, Advanced Subsonic Technology Office, NASA Lewis Research Center, organization code 2200, (216) 433-3913.

12a. DISTRIBUTION/AVAILABILITY STATEMENT

Unclassified - Unlimited
Subject Category 07

This publication is available from the NASA Center for AeroSpace Information, (301) 621-0390.

12b. DISTRIBUTION CODE

13. ABSTRACT (*Maximum 200 words*)

A three-dimensional, linearized, Euler analysis is being developed to provide an efficient unsteady aerodynamic analysis that can be used to predict the aeroelastic and aeroacoustic responses of axial-flow turbo-machinery blading. The field equations and boundary conditions needed to describe nonlinear and linearized inviscid unsteady flows through a blade row operating within a cylindrical annular duct are presented. A numerical model for linearized inviscid unsteady flows, which couples a near-field, implicit, wave-split, finite volume analysis to a far-field eigenanalysis, is also described. The linearized aerodynamic and numerical models have been implemented into a three-dimensional linearized unsteady flow code, called LINFLUX. This code has been applied to selected, benchmark, unsteady, subsonic flows to establish its accuracy and to demonstrate its current capabilities. The unsteady flows considered, have been chosen to allow convenient comparisons between the LINFLUX results and those of well-known, two-dimensional, unsteady flow codes. Detailed numerical results for a helical fan and a three-dimensional version of the 10th Standard Cascade indicate that important progress has been made towards the development of a reliable and useful, three-dimensional, prediction capability that can be used in aeroelastic and aeroacoustic design studies.

14. SUBJECT TERMS

Three-dimensional unsteady flow; Axial-flow turbomachinery blading; Euler equations; TURBO; Unsteady perturbations; Linearized equations; Flux-split; Finite-volume analysis

15. NUMBER OF PAGES

92

16. PRICE CODE

A05

17. SECURITY CLASSIFICATION OF REPORT	18. SECURITY CLASSIFICATION OF THIS PAGE	19. SECURITY CLASSIFICATION OF ABSTRACT	20. LIMITATION OF ABSTRACT
Unclassified	Unclassified	Unclassified	